Mixing and Restratification in the Upper Ocean: Competing Mechanisms in the Wave-Averaged Boussinesq Equations

by

Sean Haney

B.S., College of Creative Studies, University of California, Santa Barbara, 2009

M.S., University of Colorado at Boulder, 2013

A thesis submitted to the
Faculty of the Graduate School of the
University of Colorado in partial fulfillment
of the requirements for the degree of
Doctor of Philosophy
Department of Atmospheric and Oceanic Sciences
2015

This thesis entitled:
Mixing and Restratification in the Upper Ocean: Competing Mechanisms in the Wave-Averaged Boussinesq Equations
written by Sean Haney
has been approved for the Department of Atmospheric and Oceanic Sciences

_____

Baylor Fox-Kamper

_____

Jeff Weiss

Date _____

The final copy of this thesis has been examined by the signatories, and we find that both the content and the form meet acceptable presentation standards of scholarly work in the above mentioned discipline.

Haney, Sean (Ph.D., Atmospheric and Oceanic Sciences)

Mixing and Restratification in the Upper Ocean: Competing Mechanisms in the Wave-Averaged Boussinesq Equations

Thesis directed by Prof. Baylor Fox-Kamper

The ocean mixed layer serves as buffer through which the deep ocean and atmosphere communicate. Fluxes of heat, momentum, fresh water, and gases must pass through the mixed layer, and phytoplankton flourish most in the mixed layer where light is abundant. The dynamics of the mixed layer influence these fluxes and productivity of phytoplankton by altering the stratification and mean flow.

Restratifying hurricane wakes provide a unique setting in which a dramatically perturbed mixed layer is observable from satellite sea surface temperature. Strong horizontal temperature fronts which border these wakes suggest that two and three dimensional, adiabatic processes play a role. These observations provide the necessary parameters to estimate wake restratification timescales by surface heat fluxes (SF), Ekman buoyancy fluxes (EBF), and mixed layer eddies (MLEs). In the four wakes observed, the timescales for SF and EBF were comparable, while MLEs were much slower. The restratification time for MLEs is reduced for deeper and narrower wakes compared with other mechanisms. Therefore, stronger mixed layer fronts make MLEs competitive with surface heat and wind forcing.

Fronts are influenced by winds, waves (Langmuir circulations; LC), MLEs, and symmetric instabilities (SI). The wave averaged (Stokes drift) effects on MLEs are subtle, with aligned (anti-aligned) Stokes and geostrophic flows yielding a slight increase (decrease) in wavenumber and growth rate. Frontal effects on LC are very weak, with the primary result confirming that increased vertical stratification suppresses LC.

The effect of Stokes drift on SI is profound. It changes the background flow necessary for SI, and it alters the structure of the SI themselves. Analytic stability criteria show that

SI exist when the Ertel potential vorticity (PV) is negative. When the Stokes drift is aligned (anti-aligned) with the geostrophic shear, the PV is increased (reduced). This PV criterion is confirmed in more realistic settings with numerical linear stability, and with nonlinear large eddy simulations (LES). Therefore, in the presence of waves, the criterion $Ri < 1$ is inappropriate for the onset of SI. LES show that fronts with strongly negative PV are far more energetic than fronts that exhibit only LC.

Acknowledgements

I am extremely grateful for support from the Cooperative Institute for Research in Environmental Sciences (CIRES) through a CIRES graduate student research fellowship, from the National Science Foundation (NSF 0855010 and 0934737) and the National Aeronautics and Space Administration (NASA NNX09AF38G).

My advisor, Baylor Fox-Kemper was unconditionally encouraging. I left every meeting with him energized and excited about the work ahead rather than worried about the code bugs or other woes that I had come to the meeting to talk about. Keith Julien helped me struggle through plenty of difficult math, while also making me feel as though I wasn't struggling at all. Peter Hamlington provided excellent guidance, and very kindly, brought me in as a member of his research group after Baylor's departure from CU. Peter Sullivan constantly reminded me that my idealized science needed to relate to the real world. Furthermore, his superb expertise dramatically enhanced my understanding of large eddy simulations. Thanks to Jeff Weiss, who was always available to discuss research, and who was an excellent teacher when I was just beginning to learn about geophysical flows. Thanks to Kris Karnauskas who agreed to joined the committee with very little notice, but very much enthusiasm about my work.

Last, but certainly not least, thanks to my parents for getting me to grad school in the first place, and to my brother as well, for always being there to help when the work became frustrating and difficult. Thanks to my brother who was always available to explain applied math problems or at least commiserate over the frustrations of working with Matlab and Fortran.

Contents

Chapter

Tables

Table

Figures

Figure

Chapter 1

Introduction

At the surface of the ocean, winds, waves, and heat loss help create a layer in the upper ocean where the temperature, salinity, and other chemical properties become nearly uniform compared to the deep ocean. At the bottom of this mixed layer one finds the strongest vertical stratification of temperature and salinity (an therefore density) in the ocean. This strong stratification, the pycnocline, creates a barrier to vertical motions, and provides a natural setting for considering the dynamics of the mixed layer separate from the dynamics of the ocean as a whole.

1.1 Motivation

The atmosphere and ocean communicate through the mixed layer. Heat, momentum, fresh water, and gases are exchanged between ocean and atmosphere, and the strengths of these fluxes depend on the flow within the mixed layer. For example, imagine a strong surface heat flux from atmosphere to ocean and assume the heat is evenly distributed over the mixed layer. If the mixed layer is thin, then the mixed layer temperature will be much greater than for a deep mixed layer. This will influence the flux of heat back to the atmosphere by changing the sea surface temperature (SST), since the difference between SST and atmospheric temperature controls the flux of latent, sensible, and radiative heat.

Changes in the stratification and dynamics of the mixed layer are also very important for the organisms that live in the mixed layer. Phytoplankton flourish in the upper ocean

where the light availability is sufficient for photosynthesis. Furthermore, phytoplankton are transported around the mixed layer by the same motions which mix and restratify it. This mixing (restratifying) can inhibit (enhance) phytoplankton blooms by separating (joining) them from the light available, or nutrient rich regions. Changes in mixing can be a result of strong forcing external to the mixed layer. For example, the change in surface heat flux during spring reduces the mixing that tends to dilute high concentrations of phytoplankton near the surface by mixing them deeper (Taylor and Ferrari, 2011b; Ferrari et al., 2014). Alternatively, purely adiabatic mixed layer dynamics around strong horizontal density gradients can compete with the destabilizing surface forcing during winter, and enhance phytoplankton blooms (Taylor and Ferrari, 2011a; Mahadevan et al., 2012).

A better understanding of the fluxes between atmosphere and ocean, and the timing and intensity of phytoplankton blooms both require a better understanding of what sets the mixed layer depth (MLD). Although the phytoplankton example shows that the intensity of mixing itself may be of greater interest than effect of mixing on the MLD, we will see that estimating the MLD requires a better understanding of the intensity and character of mixing.

1.2 1-D Approaches to the Mixed Layer

The MLD depends on the relative strengths of the motions that mix and the motions that restratify the layer. These motions are usually thought of as a deviation from a larger scale well described flow, and are often referred to as turbulent motions. There are many ways to define "turbulence", for the moment, we depart from some of the classical properties of turbulence such as homogeneity and isotropy, and instead simply say that the turbulent part of the flow is that which is left over after some well defined mean flow has been removed.

A common approach to estimating the MLD is to assume that the MLD can be directly computed by assuming a balance of turbulent heat fluxes ($\overline{w'T'}$; a measure of the importance of stratification) and vertical fluxes of horizontal momentum ($\overline{u'w'}$ a measure of the vertical

mixing induced by shear). One of the most common approaches of this kind comes from Monin-Obukhov similarity theory for atmospheric boundary layers Monin and Obukhov (1954). The concept is to use these quantities that describe the turbulence in conjunction with other known dimensional quantities to form the Obukhov length scale (L_O),

$$L_O = \frac{(\overline{u'w'})^{3/2}}{k_0 \frac{g}{T_0} \overline{w'T'}} \tag{1.1}$$

where u' and w' are turbulent horizontal and vertical velocities respectively, $k_0 \approx 0.41$ is the Von Kármán constant, $g \approx 9.81\ ms^{-2}$ is the gravitational acceleration, and T_0 is the mean temperature about which the temperature deviations (T') fluctuate. L_O can then be used to form a non-dimensional vertical distance from the boundary ($\hat{z} = \frac{z}{L_O}$) over which the vertical shear and temperature may vary. Then these profiles of temperature and velocity related such that the ratio of the temperature gradient to the velocity gradient scales only with the large scale parameters.

L_O is a perfect example of the how the competition of mixing and restratifying processes combine to determine the MLD, but how do we know what the turbulent fluxes are? It is common to relate the wind stress at the surface of the ocean to the turbulent momentum flux, and similarly for the surface heat flux, however, there are dynamics intrinsic to the ocean that contribute to these turbulent fluxes. Conceptualizing the mixed layer as a layer where the wind stress and surface heat flux conspire with (or compete against) each other to erode (or enhance) otherwise stable stratification is a reasonable first estimate. Several 1-D models have been developed on this principle with surface fluxes that vary on different time scales from diurnal (Price et al., 1986, e.g.) to seasonal Kraus and Turner (1967). These approaches provide a one-dimensional perspective of mixing and restratification, but coherent two and three-dimensional (2D, and 3D) structures are ubiquitous in the mixed layer. How do these 2D and 3D structures influence the rates of mixing and restratification?

1.3 Coherent Structures and Instabilities

As mentioned above, the surface shear stress, and heating or cooling induce turbulent fluxes in the mixed layer, but there are many 2D and 3D coherent structures observed in the mixed layer which themselves are often treated as turbulent fluxes. Here I will take coherent structures to mean any feature of the flow with motion strongly confined to a single length scale that persists for more than a few eddy turnover times. A good estimate of the eddy turnover time would then be the characteristic length scale divided by the characteristic velocity of the coherent structure. This paints a picture of a flow with many features all at one, or a few length scales, when in fact a defining characteristic of turbulence is that the flow contains energy at all scales. The ability for the different scales to interact and pass energy between is what allows for turbulence. Lastly, the remaining several sections and chapters will refer to instabilities. By this I mean a perturbation to some well defined mean flow that reinforces itself rather than being forced back toward a quiescent or oscillating state. The instabilities discussed here will be thought of as the drivers that define the energy injecting scales, which ultimately in a turbulent flow, would interact with other scales of motion and transfer energy and enstrophy. In this dissertation, I choose to focus on a select few of these coherent structures which are thought to dominate adiabatic mixed layer dynamics.

1.3.1 Langmuir Cells

Undoubtedly, the most easily observable (visually at least) dynamical mechanism that affects the mixed layer are surface gravity waves (waves hereafter; any discussion of other types of waves will include specification). Anyone who looks out on the ocean can see them, and on occasion, watch them break even in deep water. Almost as widely observed as waves (based on personal communications with friends and family), is the combined effect of winds and waves that gives rise to windrows. Windrows are parallel lines of surface convergence which are easily visualized when floating debris collects along these lines (figure 1.1). The

spacing of windrows is often regular, but notably, they exhibit many different length scales of spacing at one time. Some of the basic dynamics of windrows were first well documented by Dr. Irving Langmuir Langmuir (1938), and they are now referred to as Langmuir cells (LC).

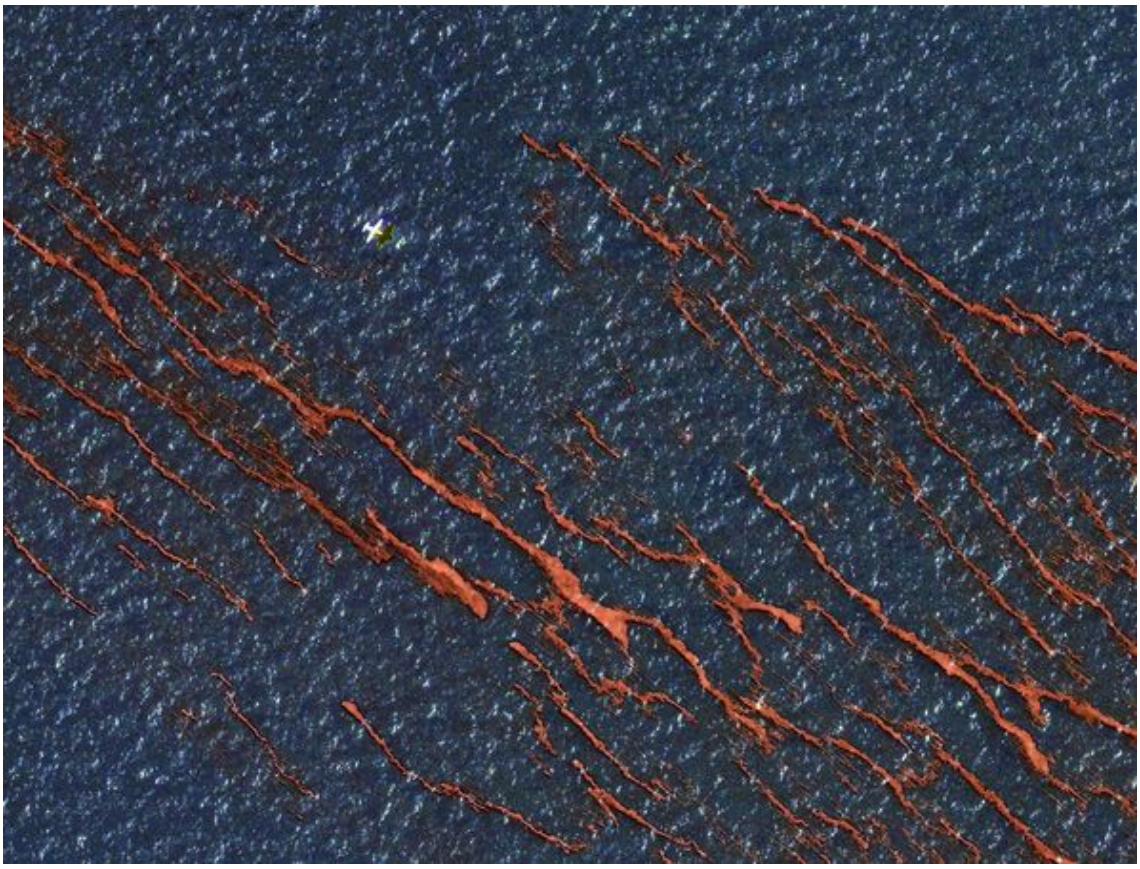

Figure 1.1: Image from: http://www.oilspillsolutions.org/evaluation.htm. Oil collects in the surface convergence zones of windrows (LC) after the Deep Water Horizon oil spill. Note that the LC direction is roughly parallel to the wave propagation direction (perpendicular to wave crests). Also note the airplane conveniently present provides a sense of scale.

Smith (1992) observed a sudden increase in windrows following an increase in the winds. He noted that the spacing of the LC was roughly two thirds the dominant wavelength of the waves. Furthermore, his measurements of density showed that the depth of mixing increased as the LC developed. D'Asaro and Dairiki (1997) showed that during a period of rapid

mixed layer deepening due to a storm, vertical velocity measurements were much greater than what would be expected for the measured wind stress imparted on the surface of the ocean. They hypothesized that these high vertical velocities were due to LC. Weller and Price (1988) observed characteristic LC structures including strong downwind and vertical velocities ($> 20\ cm\ s^{-1}$) at surface convergence zones. The LC were able to mix weakly stratified near surface water that had formed from daytime surface heating, but they could not penetrate to the base of the mixed layer.

The mathematical underpinnings of LC were developed by Craik and Leibovich (1976). To achieve this, they use a wave-filtered version of the Navier-Stokes equations. To retain the leading order effect of the waves on currents, averaging over the period of the waves is performed, and the result is a drift current, $\mathbf{U}^S$ in the direction of wave propagation.

$$\mathbf{U}^S = \left\langle \int^t \mathbf{u}^w dt \cdot \nabla \mathbf{u}^w \right\rangle \tag{1.2}$$

where $\mathbf{u}^w$ is the Eulerian velocity in the waves, and the angle brackets indicate an average over a time longer than the wave period but shorter than the timescale on which the current changes. This results in the addition of a Stokes vortex force ($\mathbf{U^S} \times (\nabla \times \mathbf{u})$), and a Stokes induced velocity head in the pressure. Lane et al. (2007) showed that the Stokes vortex force is the dominant wave-averaged effect on currents. Huang (1979) showed that the there is also a Stokes Coriolis force. McWilliams et al. (2004) showed that Combining these results gives the rotating, wave-averaged, Boussinesq equations (WAB).

$$\begin{aligned}
\partial_t \mathbf{u} + (\mathbf{u} \cdot \nabla)\mathbf{u} + f\hat{k} \times \mathbf{u}^L + \nabla\pi &= \mathbf{U^S} \times (\nabla \times \mathbf{u}) + b\hat{k} + \nu\nabla^2\mathbf{u}, && (1.3)\\
\partial_t b + (\mathbf{u}^L \cdot \nabla)b &= \kappa\nabla^2 b, && (1.4)\\
\nabla \cdot \mathbf{u} &= 0, && (1.5)\\
\textit{where,} \qquad \pi &= \left(\frac{p}{\rho_0} + \frac{1}{2}|\mathbf{u} + \mathbf{U^S}|^2 - \frac{1}{2}|\mathbf{u}|^2\right)
\end{aligned}$$

Where f is the Coriolis frequency, b is the buoyancy, ν is the kinematic viscosity, κ is the thermal diffusivity, p is the pressure, and ρ_0 is a reference density.

Alternatively, wisely applied vector identities reveal an equivalent form of the momentum equation where the advecting velocity is always Lagrangian, the pressure is unchanged, and the Stokes vortex force is replaced by the Stokes shear force ($u^{L,j}\nabla u^{S,j}$) (Suzuki and Fox-Kemper, 2015).

$$\partial_t \mathbf{u} + (\mathbf{u}^L \cdot \nabla)\mathbf{u} + f\hat{k} \times \mathbf{u}^L + \nabla p + u^{L,j}\nabla U^{S,j} = b\hat{k} + \nu\nabla^2\mathbf{u}. \tag{1.6}$$

Note that the waves, and therefore Stokes drift have been assumed stead in this cases, and therefore, no Stokes drift tendency term appears. Only this form of the momentum equation will be used in subsequent chapters as it conveniently highlights unusual ways in which the Stokes drift interacts with the flow while still providing a similar level of physical intuition as the vortex force formulation. For example, note that the Stokes drift advects momentum, but it is not itself advected. Gnanadesikan and Weller (1995) explain that this is because "the Stokes drift is a wave quantity and is so trapped to the surface gravity waves by the pressure field." Furthermore, this formulation of the momentum equation nicely separates the two primary effects of wave forcing: the Stokes Coriolis term ($f\hat{\mathbf{k}} \times \mathbf{U}^S$), which we will see is relevant when the Coriolis force is comparatively strong (i.e. large scale flows), and the Stokes shear term ($u^{L,j}\nabla U^{S,j}$), which is only dynamically interesting when there are horizontal variations in either the Eulerian or Stokes flow. Note that with horizontally invariant Stokes drift, this term only appears in the vertical momentum equation ($\mathbf{u}^L \cdot \mathbf{U}_z^S$). If one considers only horizontally uniform mean flows, this separates these two effects of Stokes drift nicely. The Stokes Coriolis changes the mean flow balance, and the Stokes shear imposes an alternating and unbalanced vertical force on the perturbations which may go unstable.

The instabilities (LC) that Stokes drift produce hinges upon the action of the Stokes shear force. If we consider horizontally invariant Stokes drift and a horizontally invariant Eulerian mean flow, the Stokes shear force only acts vertically, and uniformly in the horizontal directions, and can therefore be balanced by a vertical pressure gradient. However, if either

the Stokes drift or the Eulerian flow vary horizontally, an unbalanced Stokes shear force is created. These two possibilities describe the two commonly discussed instability mechanisms for LC, however, here I choose to focus only on the case of horizontally invariant Stokes drift.

Craik (1977) suggested an instability mechanism, later named CL2. In this case, the Stokes drift is assumed horizontally invariant, the Eulerian flow is assumed downwind invariant ($\partial_x(\cdot) = 0$), and the Eulerian flow near the surface will be given some small perturbation (figure 1.2). Then the resulting Stokes shear force is downward and it peaks in amplitude at the maximum velocity perturbation. This creates a vertical pressure gradient drawing water downward. Continuity then implies converging water at the surface. In the inviscid case, along this low pressure line, the dominant contribution to the x momentum is the vertical advection term, since $v = 0$ and the flow is downwind invariant.

$$u'_t = -w'\overline{U}_z, \tag{1.7}$$

$$w'_t = -u'U^S_z \tag{1.8}$$

where $(\cdot)'$ indicates a perturbation from a horizontally averaged mean, $\overline{(\cdot)}$. Therefore, the initial perturbation causes a further acceleration of the flow (since $w' < 0$ and $\overline{U}_z > 0$ above). This also highlights the reason that positive Eulerian shear (i.e. aligned with the Stokes shear) results in stronger LC (Van Roekel et al., 2012). Additionally, since the Stokes shear force acts in the direction of the circulation, it does positive work, reinforcing the circulation.

Leibovich (1977a) showed that in the presence of stratification and the absence of viscosity, a nessessary and sufficient condition for instability is given by

$$\overline{U}_z(z)U^S_z(z) - N^2(z) > 0, \tag{1.9}$$

for any depth, z, within the flow. Here $N^2 \equiv \frac{\partial b}{\partial_z}$ is the vertical buoyancy frequency squared. This suggests that the Stokes and Eulerian shears must be, at least partially, aligned for the instability to occur. Viscid, but constant density analysis showed that the stability of LC

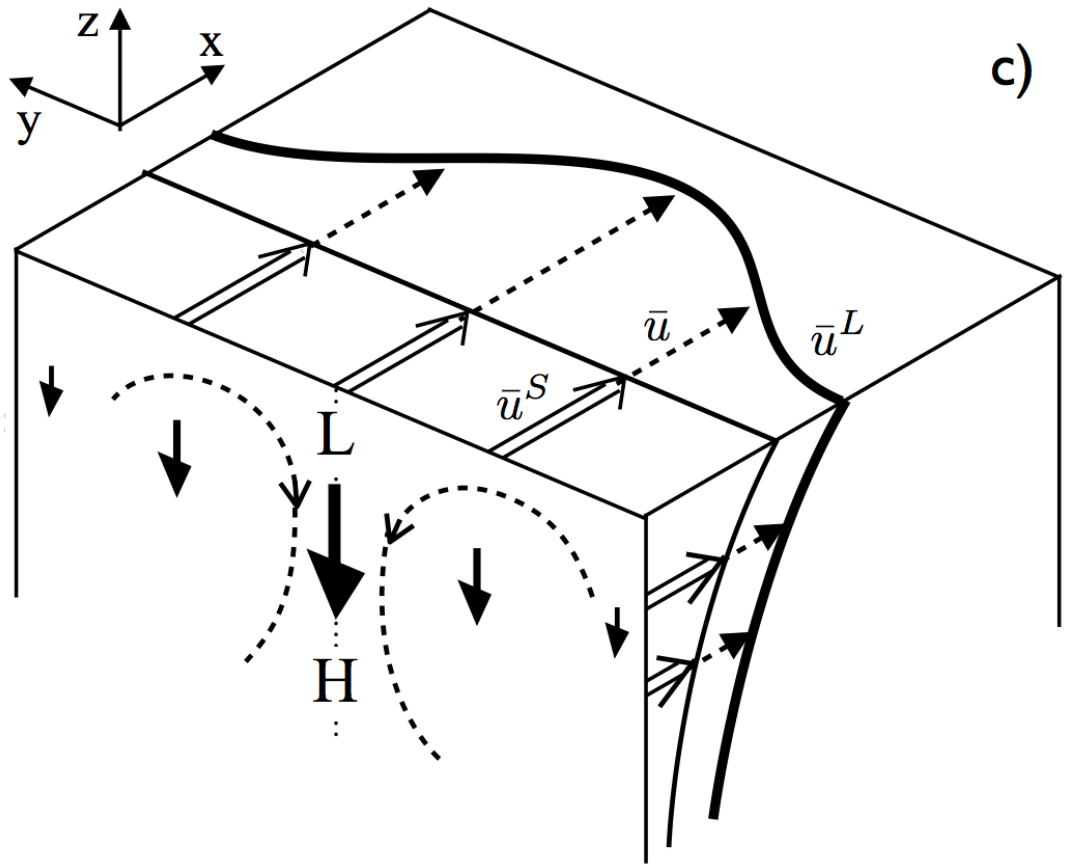

Figure 1.2: Figure 1c. from Suzuki and Fox-Kemper (2015). The dashed arrows indicate Eulerian flow, the double line arrows indicate Stokes drift, and the bold arrows indicate the strength and direction of the Stokes shear force. H and L indicate regions of high and low pressure respectively. The Stokes shear force induces and maintains the pressure gradient shown, which then induces LC (the dashed counter-rotating flow). In this figure only, over bars indicate wave averaged quantities. This notation applies only to this figure as it is inconsistent with the notation used throughout the rest of this work.

depends on the Langmuir number (La) (Leibovich, 1977b).

$$La = \left(\frac{(\nu k^w)^3}{U^S u^{*,2}} \right)^{1/2} \tag{1.10}$$

where k^w is the wavenumber of the waves, and $u^* = \sqrt{\frac{\tau}{\rho_0}}$ is the friction velocity, and τ is the wind stress. La can be interpreted as the competition between the rate of viscous damping of down wind/wave vorticity and the rate of production of vorticity by Stokes drift. Leibovich and Paolucci (1981) show that the stability limit for LC in a weakly stratified layer

($Ri \sim 0.1$) occurs at $La \sim O(1)$. In the ocean mixed layer, typically, $La << 1$, implying that the mixed layer is always in the supercritical regime for LC.

An alternative, turbulent, Langmuir number was proposed by McWilliams et al. (1997).

$$La_t = \sqrt{\frac{u^*}{U^S}}. \tag{1.11}$$

Here, the Stokes velocity and friction velocity are compared. Small La_t implies that the wave effects are much stronger than the wind effects. For fully developed waves, where further energy input by the wind only causes wave breaking rather than further growth, $La_t \approx 0.3$. This can be derived by first assuming a Stokes drift for unidirectional, fully developed waves (Webb and Fox-Kemper, 2011).

$$U_s = (0.0162)u_{10}, \tag{1.12}$$

where u_{10} is the 10 m wind speed. Then the conversion from wind speed to wind stress (Large and Pond, 1981) is given by

$$\rho_a u_a^{*,2} = \rho_a u_{10}^2 C_d. \tag{1.13}$$

where ρ_a and ρ_o are the air and ocean density respectively, and C_d is the drag coefficient. This gives the stress on the atmosphere, but we are interested in the stress on the ocean which is given by

$$u_o^* = u_{10}\sqrt{C_d \frac{\rho_a}{\rho_o}}. \tag{1.14}$$

Then using the derived Stokes drift (equation 1.12) and friction velocity (equation 1.14) in La_t (equation 1.11) yields

$$La_t = \left(\frac{\sqrt{C_d \frac{\rho_a}{\rho_o}}}{(0.85)(0.0162)} \right)^{1/2} \tag{1.15}$$

which is approximately 0.3 for realistic values of ρ_a, ρ_o, and C_d.

Gnanadesikan and Weller (1995) explored the linear instability of LC in an Ekman layer. As alluded to, the Stokes Coriolis force alters the mean flow requiring an anti-Stokes Eulerian flow, in effect making the Ekman spiral wider. LC do still occur, and are strongest

when the influence of the Coriolis force on the perturbations is weak, and when the waves are strong compared to the viscosity (small La). Furthermore they find that the fastest growing LC are aligned in the direction of the Lagrangian shear, however, the Eulerian shear and Stokes shear are not always partially aligned.

In addition to the many analytic and linear analyses of LC, several fully nonlinear Large Eddy Simulations (LES) of the WAB have been performed. McWilliams et al. (1997) adapt the LES model developed by Moeng (1984) to include Stokes drift, and they are able to simulate the characteristic features of surface convergence and divergence zones with associated downwelling and upwelling velocities respectively. Sullivan et al. (2007) simulated a mixed layer with Stokes drift and stochastic momentum input to emulate breaking waves. They showed that LC readily form, and sometimes are seeded by the vorticity injection from breaking waves. Furthermore, the breakers can produce a deeply penetrating downwelling jet that enhances entrainment at the mixed layer base. Harcourt and D'Asaro (2008) performed simulations that showed the maximum vertical kinetic energy peaks deeper in the layer as the Stokes e-folding depth is increased until roughly 20% of the way down into the mixed layer. The amplitude of this peak decreases as it moves down with the increasing Stokes depth. These findings are compared with observations from Lagrangian floats, and help explain some of the discrepancy between the observed and expected vertical kinetic energy based on wind stress alone. LES of misaligned winds and waves show that LC align with the Lagrangian shear in mostly ($< 90°$) aligned wind-wave scenarios (Van Roekel et al., 2012).

1.3.2 Mixed Layer Eddies

Before proceeding with a discussion of mixed layer eddies (MLEs), it is relevant to provide an overview of the dynamics of baroclinic instability. Baroclinic flows are ones in which the constant pressure surfaces cross the constant density surfaces. When the effect of rotation is much stronger than the effects of non-linear advection (i.e. $Ro \equiv \frac{U^2}{L}/fU = \frac{U}{fL} << 1$), then the Coriolis force may balance the horizontal pressure gradient force (geostrophic

balance). Furthermore, if the vertical momentum balance remains hydrostatic ($P_z = -\rho g$), these balances combine to form thermal wind balance,

$$fU_z = -B_y \tag{1.16}$$

The result is a balanced flow with both available kinetic energy (in the geostrophic shear), and potential energy (in the horizontal buoyancy gradient). The analysis of baroclinic instability follows with the assumption of quasi-geostrophic (QG) motions and, perhaps more importantly, perturbations to that motion which are also quasi-geostrophic. Furthermore, the buoyancy is scaled as the hydrostatic pressure, which, recall is balanced by (and thus can be scaled by) the Coriolis force. It is also important to note that QG motions are characterized by the motions similarly sized, or smaller than the Rossby radius of deformation $L_d \equiv \frac{NH}{f}$. This assumption combined with the buoyancy scaling, and small Ro form the key features of QG scaling. As a result of geostrophy and continuity (the flow is assumed to be Boussinesq, and therefore $\nabla \cdot \mathbf{u} = 0$), the leading order vertical velocity is zero. As a result of the buoyancy scaling with the Coriolis force, the leading order buoyancy equation is:

$$b_{0,t} + (\mathbf{u}_0 \cdot \nabla) b_0 = -w_1 \left(\frac{Ld}{L} \right)^2, \tag{1.17}$$

where $(\cdot)_0$ indicates the leading order quantity, and $(\cdot)_1$ indicates a quantity that is Ro smaller than leading order, and L is the scale of the perturbation. As a result the vertical velocity is replaced by buoyancy conservation throughout. It is this strict relation between buoyancy and vertical velocity that wedges QG dynamics between 2D and fully 3D flow. While simpler than 3D flow (since there is no vertical velocity), QG dynamics retains the property of vortex stretching which is absent from 2D flow. The vortex stretching term is just enough to retain the dynamics that are relevant for baroclinic instability.

Consider the scales of QG motions $L \lesssim L_d$. Then $\left(\frac{L}{L_d} \right)^2 = \frac{L^2 f^2}{N^2 H^2} \equiv (RiRo^2)^{-1}$. This implies QG motions near the deformation radius, which have small Ro, must have very large Ri. The simplest of the QG baroclinic instability problems comes from Eady (1949), where

constant Coriolis frequency and buoyancy gradients are assumed. Eady (1949) found that baroclinic instability exists only for a limited range of long wavelengths (no smaller than $2.6L_d \approx 70\ km$) with the fastest growth at $\sim 3.9L_d$ ($\approx 100\ km$). Furthermore, the e-folding time for the fastest growing mode is $\sim 0.3\frac{\sqrt{Ri}}{f}\ s$ (≈ 10 days). The Charney (1947) problem examines a more general baroclinic instability problem in which the Coriolis frequency and buoyancy gradient may vary horizontally. Both do reasonable jobs of describing baroclinic eddies at the mesoscale $O(100\ km)$.

As previously mentioned, QG (mesoscale) baroclinic instability exists when $RiRo^2 \sim 1$ and $Ro << 1$ (and therefore, $Ri >> 1$), but we know that the stratification is very weak in the mixed layer (thus small Ri). In addition, the MLD is shallow, and therefore the mixed layer deformation radius is far smaller ($\sim 1\ km$) than the mesoscale deformation radius. Therefore, if we are interested in baroclinic motions in the mixed layer near the deformation radius, we must consider flows with $Ro \sim O(1)$. In the QG scaling, both the mean and perturbed flow were assumed to be QG. For the mixed layer, it is sufficient, if not illustrative, to consider non-hydrostatic 3D perturbations around a QG mean flow. These disparate scalings result in inner and outer length scales, the outer which follows from QG and results in a small Ro for the mean flow, and the inner, turbulent length scale which results in $Ro \sim O(1)$.

Baroclinically unstable flow in the $Ri, Ro \sim O(1)$ regime,has been studied extensively. Stone (1966, 1970) showed that ageostrophic ($Ro \sim O(1)$) baroclinic instabilities are dominant for $Ri > 0.95$. These instabilities have maximum growth rates of $\sigma = \left(\frac{5}{54(1+Ri)}\right)^{\frac{1}{2}}$ ($(\sigma f)^{-1} \sim 16$ hours for $Ri = 1$) for wavenumbers $k = \left(\frac{5}{2(1+Ri)}\right)^{\frac{1}{2}}$ ($\frac{2\pi L_d}{k} \sim 7\ km$ for $Ri = 1$, $L_d = 1\ km$). A natural next step beyond ageostrophic motions, which may occur on smaller length scales, is to consider non-hydrostatic effects. Stone (1971) showed that strong non-hydrostatic effects slightly reduce the growth rate and wavenumber of the fastest growing baroclinic instabilities (some of these results will be shown in chapter 3).

Boccaletti et al. (2007) increase the complexity of the problem by allowing a moving

bottom boundary making it much more similar to the pycnocline. Although the growth rates of baroclinic instability are reduced since some of their energy is used to create waves along the bottom boundary, the primary effect of the sloping bottom boundary is to prohibit very low wavenumber modes. This, in addition to having larger growth rates at mixed layer deformation radius scales, is what restricts mixed layer eddies to be $O(1\ km)$ and not much larger (unlike mesoscale eddies). Furthermore, Boccaletti et al. (2007) highlight the fact that ageostrophic baroclinic instabilities in the mixed layer grow sufficiently fast $O(1\ day)$ that: 1) they may become the primary driver of restratification in the mixed layer (as opposed to geostrophic adjustment Tandon and Garrett (1995)), and 2) the rate of restratification can be high enough to compete with mixing events, and help set the MLD.

Recall that part of the goal in describing dynamical mechanisms for mixing and re-stratitfication in the mixed layer is to compare the net effects of these precesses to the the surface fluxes. Since the net effect of mixed layer eddies is to restratify, the relevant turbulent flux is the buoyancy production ($\overline{w'b'}$). Fox-Kemper et al. (2008) parametrize the vertical and horizontal ($\overline{v'b'}$) buoyancy fluxes in terms of the mean stratification, MLD, and Coriolis frequency. This parametrization is included into a 2D (across front and vertical directions) model which cannot become baroclinically unstable because along front perturbations (the only ones for which baroclinic instability grows) are not present. This 2D model (with the parametrization) approximates well the restratifying effect of mixed layer eddies when compared to 3D (i.e. explicitly resolving baroclinic instability) simulations (figure 1.3; Fox-Kemper and Ferrari, 2008). This success underscores the fact that mixed layer eddies induce a strongly restratifying effect. This success, then motivated the use of this parametrization in a mesoscale resolving general circulation model Fox-Kemper et al. (2011)

Although the primary effect of mixed layer eddies is to extract potential energy from the mean flow by slumping the front (restratifying), as mentioned above, these instabilities extract little to no energy from the geostrophic shear. Since the geostrophic shear offers another source of energy, we might expect there are fronts that become unstable to modes

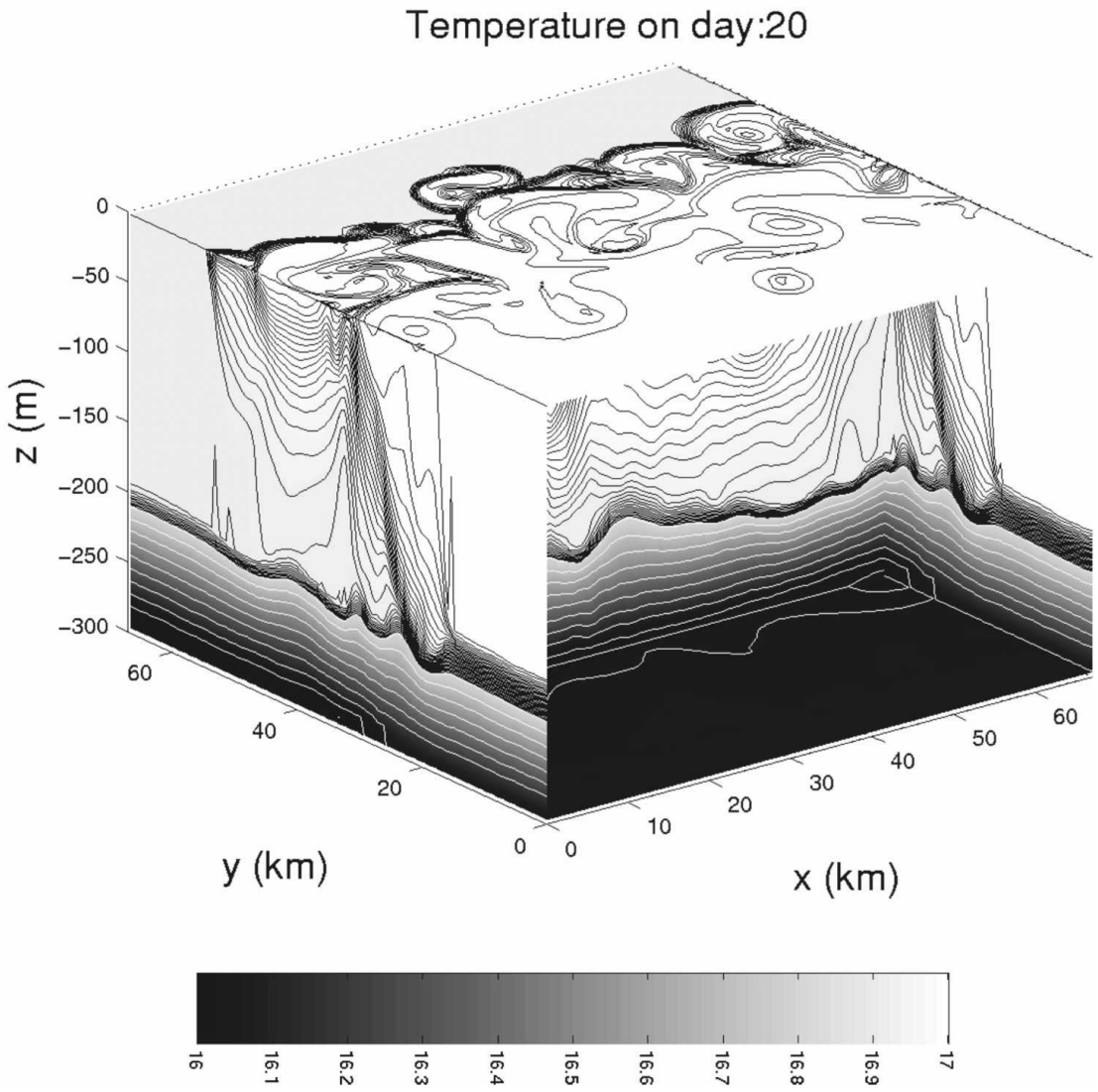

Figure 1.3: Figure 2b. from Fox-Kemper et al. (2008). A simulation of a baroclinically unstable front. After 20 days, the flow has become nonlinear, and the instabilities interact forming MLEs. The net effect of slumping the front (which was initially nearly vertical) can be seen on the left face. Temperature is contoured (contour interval = $0.01°C$ in the mixed layer).

that extract more kinetic than potential energy. These fronts are dominated by symmetric instabilities.

1.3.3 Symmetric Instabilities

Symmetric Instabilities (SI) are characterized by alternating positive and negative velocity along isopycnals (figure 1.4). The stereotypical fastest growing mode has high cross

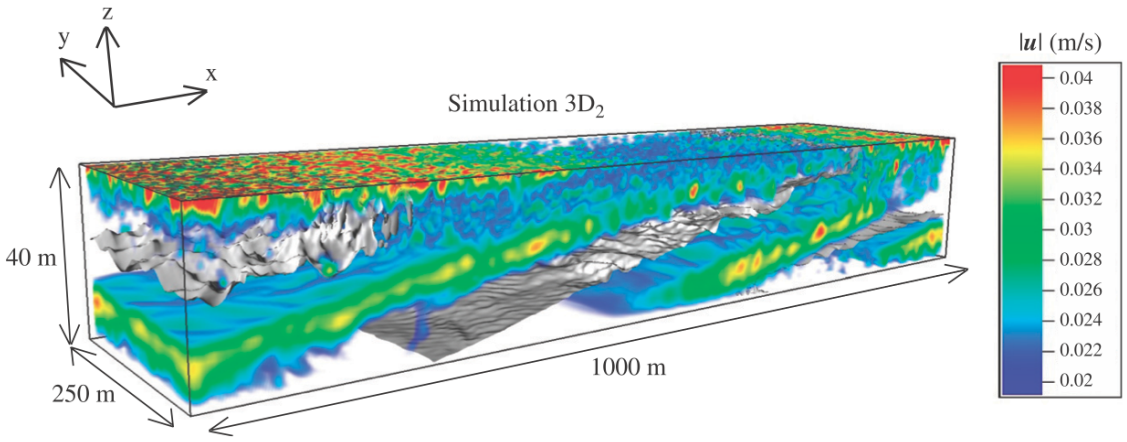

Figure 1.4: Figure 12 from Taylor and Ferrari (2010). Cross front (the 1000m directino) velocity magnitude, $|u|$, is shown in color. The gray surfaces are isopycnals.

front wavenumber, and zero along front wavenumber Stone (1970). Stone (1971) showed that SI may only exist when $Ri^g \equiv \frac{N^2 f^2}{M^4} < 1$ (where $M^2 \equiv b_y$). Hoskins (1974) showed that SI may only exist when the Ertel potential vorticity (PV) is negative.

$$SI \quad \Longrightarrow \quad PV = (\nabla \times \mathbf{u} + f\hat{\mathbf{k}}) \cdot \nabla b < 0. \tag{1.18}$$

Furthermore, Hoskins showed that when the relative vorticity is strictly due to the geostrophic flow, negative PV gives an equivalent criteria on Ri^g, and when there is no relative vertical vorticity, this collapses to Stone's $Ri^g < 1$ criteria.

$$PV^g = \zeta N^2 - \frac{M^4}{f} < 0, \ \textit{or equivalently,} \tag{1.19}$$

$$Ri^g < \frac{\zeta}{f}. \tag{1.20}$$

where $\zeta \equiv f - (\nabla \times \mathbf{u}) \cdot \hat{\mathbf{k}}$.

Ertel showed that PV is materially conserved ($\frac{D(PV)}{Dt} = 0$) (e.g. Vallis, 2006), therefore, the mixing done by SI results in an exchange of negative PV fluid with positive PV fluid until the PV has mixed and become zero, and SI can no longer form. If the fluid has negative PV everywhere, SI can not restore the PV to zero, however, in the real ocean mixed layer, both a frictional surface boundary, and the highly stratified pycnocline may serve as significant sources of positive PV.

The frictional surface boundary layer acts as a source or sink for PV due to the interaction between the surface wind stress, and fronts (Thomas, 2005; Thomas and Ferrari, 2008). Downfront (upfront) wind stress (i.e. in the direction of the geostrophic shear associated with the front) extracts (injects) PV from the surface ocean by advecting dense (light) water over light (dense) water. The vertical, frictional PV flux is given by

$$J_z^F = f\nabla_h b \times \mathbf{F}, \tag{1.21}$$

where $\mathbf{F}$ is the frictional force of the wind. Furthermore, even in the absence of wind stress, if there is any Eulerian shear in the flow that extends to the surface, it must be canceled by an opposing Ekman shear, and this Ekman shear will still induce a surface PV flux (Thomas and Ferrari, 2008). In the context of no surface stress above geostrophic shear, this is referred to as frictional spindown (Thomas and Rhines, 2002). In this case, the induced stress directly opposed the geostrophic shear, and therefore always induces a negative PV flux (i.e. into the ocean; restratifying). The frictional PV flux may also be interpreted as a horizontal, Ekman buoyancy flux (EBF) (Thomas and Taylor, 2010) and is given by

$$EBF = \frac{M^2\tau}{\rho_0 f}. \tag{1.22}$$

In the case of downfront winds, the reduction of surface PV results in forced symmetric instability (FSI). The rate of kinetic energy extraction by FSI scales with the EBF.

The frictional PV flux may rival the diabatic PV flux due to surface cooling or heating Taylor and Ferrari (2010).

DAsaro et al. (2011) showed in multiple cross sections of the Kurashio extension that conditions more favorable for SI were coincident with higher energy dissipation rates (figure 1.5). In the traditional view that the flow, and turbulence in the mixed layer is driven by

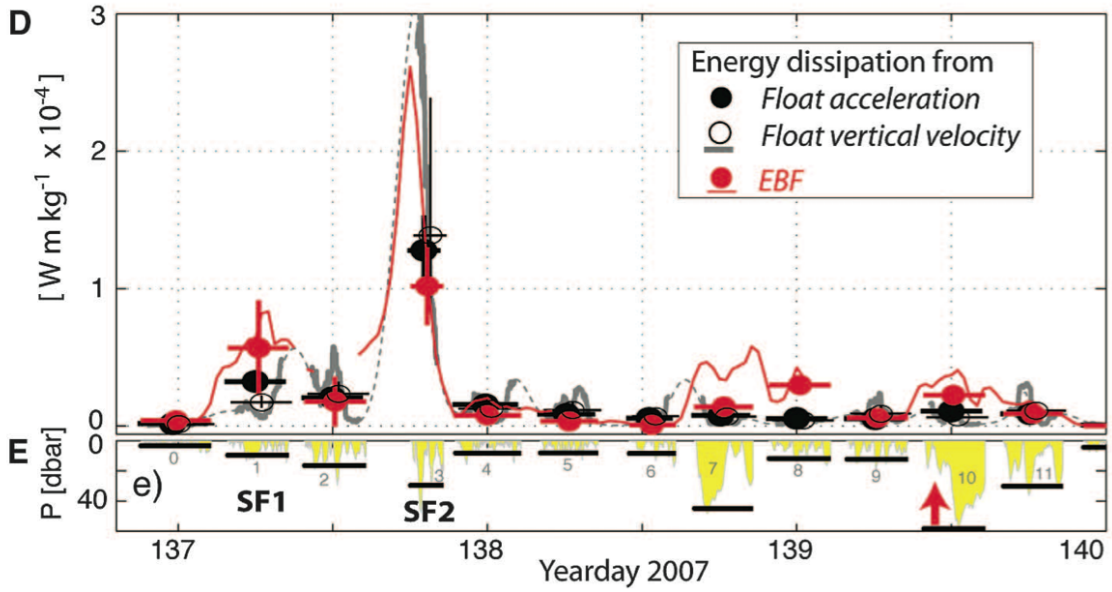

Figure 1.5: Figure 3d and e from DAsaro et al. (2011). Energy dissipation rate from a Lagrangian profiling float and from estimates of EBF in a strong submesoscale front (SF2) in the Kuroshio extension.

atmospheric forcing, one would expect turbulent dissipation to be strongly correlated with wind stress or surface cooling. However, despite only moderate wind stress near a surface front (SF2) compared to the other locations sampled (where the front was not as strong), the energy dissipation is very high, and is coincident with a large EBF. Furthermore, this region was stably stratified ($N^2 > 0$), so there was no convective heat flux. Therefore, the enhanced energy dissipation is likely due to FSI because of a reduction of the PV by EBF.

Once SI become strong enough, a secondary Kelvin-Helmholtz instability (KHI) forms Taylor and Ferrari (2009). This KHI produces small scale turbulence to aid the entrainment of high PV water from the pycnocline and frictional surface layer. This expedites the restoration of mixed layer PV to zero.

Haine and Marshall (1998) showed that in conditions with only geostrophic shear, SI travel along isopyncals, and therefore get their energy from the kinetic energy (the geostrophic shear) without changing the available potential energy in the front. In other words, SI mix the surface ocean without substantially affecting the stratification.

1.3.4 Kelvin-Helmholtz Instabilities

In flows with stable stratification, but sufficiently strong vertical shear, the shear may overcome stable stratification and produce Kelvin-Helmholtz instabilities (KHI). These instabilities have been observed in the ocean (figure 1.6), and contribute to vertical mixing of buoyancy. Miles (1961) proved the standing conjecture of G.I. Taylor that in a stratified

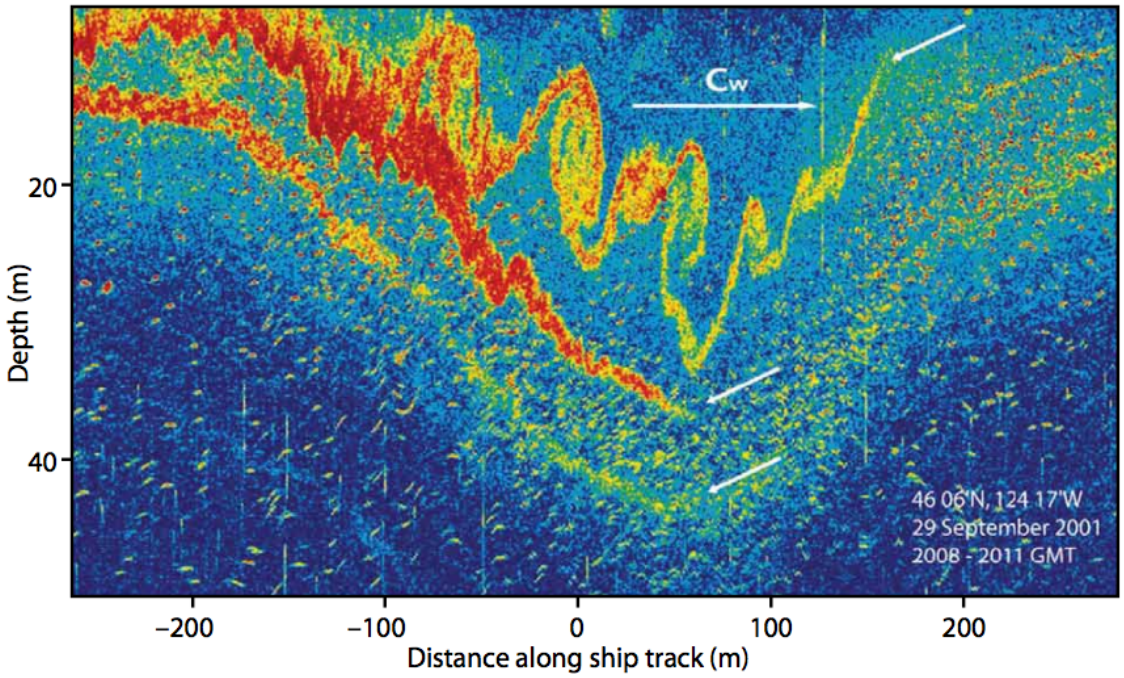

Figure 1.6: Figure 14 from Moum et al. (2003). Acoustic backscatter shows KHI forming from the shear produced by a solitary wave.

parallel shear flow, when $Ri^E \equiv \frac{N^2}{U_z^{E,2}} < \frac{1}{4}$, the flow is unstable to KHI. Howard (1961) proved this to be true for a more general class of shear profiles, and showed that the complex wave

velocity of unstable modes is bounded by $\frac{1}{4}(U_{max} - U_{min})^2$, where U_{max} and U_{min} are the maximum and minimum velocity of the mean shear flow respectively.

Since all the above criteria were derived in the absence of Stokes drift, one might ask how if at all the Stokes shear contributes to the instability of KHI. Holm (1996) showed that in the presence of Stokes drift, an inflection point in the Eulerian velocity is necessary, and that $Ri \equiv \frac{N^2}{U_z^{L,2}} < \frac{1}{4}$, where recall Ri is the *Lagrangian* Richardson number (which will be used throughout this work), is sufficient for KHI. As discussed in section 3.4, the presence of Stokes drift changes the Eulerian flow through the Stokes Coriolis force by producing an anti-Stokes Eulerian flow. However, analytic solutions for the Ekman layer with Stokes drift show that the Lagrangian flow is unchanged (Gnanadesikan and Weller, 1995; McWilliams et al., 2014, Appendix C).

Lastly, parametrizations of ocean mixing are often built under the assumption that this mixing is driven by wind which produces shear instabilities near the surface (Price et al., 1986; Large et al., 1994, e.g.). The stability criteria ($Ri^E < \frac{1}{4}$) for KHI is often used in these parametrizations, however, as is evident in the previous two sections, higher Ri flows can be unstable to motions that mix buoyancy and momentum in the mixed layer. These turbulent fluxes are unaccounted for in such parametrizations.

1.4 Wave-Front Interactions

Although the instabilities and turbulence due to waves and submesoscale features of the ocean have been extensively studied on their own, knowledge of their interactions is sparse. As will be shown, the dynamics of LC are strongly non-geostrophic ($Ro >> 1$; rather than ageostrophic, $Ro \sim O(1)$), and non-hydrostatic, whereas the dynamics of geostrophic instability (GI; rather than baroclinic instability to distinguish from SI which is also baroclinic), SI, and fronts in general require planetary vorticity, and stratification which constrain them to be nearly hydrostatic. Despite the discrepancies in the dynamical regimes, and the scale separation, waves forcing may have a a strong influence on submesoscale motions, and fronts

can influence wave forced turbulence.

Wave forcing may not only affect the instabilities, but also the structure of the front itself. McWilliams and Fox-Kemper (2013) showed that a front adjusts conservatively to the arrival of waves, and the result is a horizontally uniform anti-Stokes Eulerian flow which maintains the balance between Coriolis forces (Stokes and Eulerian) and the pressure gradient. Furthermore, for finite width fronts and filaments, the buoyancy and flow fields take the opposite symmetry (e.g. initially odd buoyancy structure of a filament gains an even buoyancy perturbation due to the adjustment). The Rossby number is a measure of the strength of the front or filament, while their parameter $\epsilon \equiv \frac{U^S H}{fLH^S}$ is a measure of the strength of the Stokes shear force in the vertical momentum equation. Oceanographers have been concerned about ageostrophic ($Ro \sim O(1)$) effects on the flow for more than a decade, but figure 1.7 shows that if we think strong fronts and filaments are important for the dynamics, we also ought to be concerned with wave effects. The strength of the Stokes shear perturbation to hydrostatic balance can be an order of magnitude or larger than the ageostrophic perturbation to the geostrophic balance.

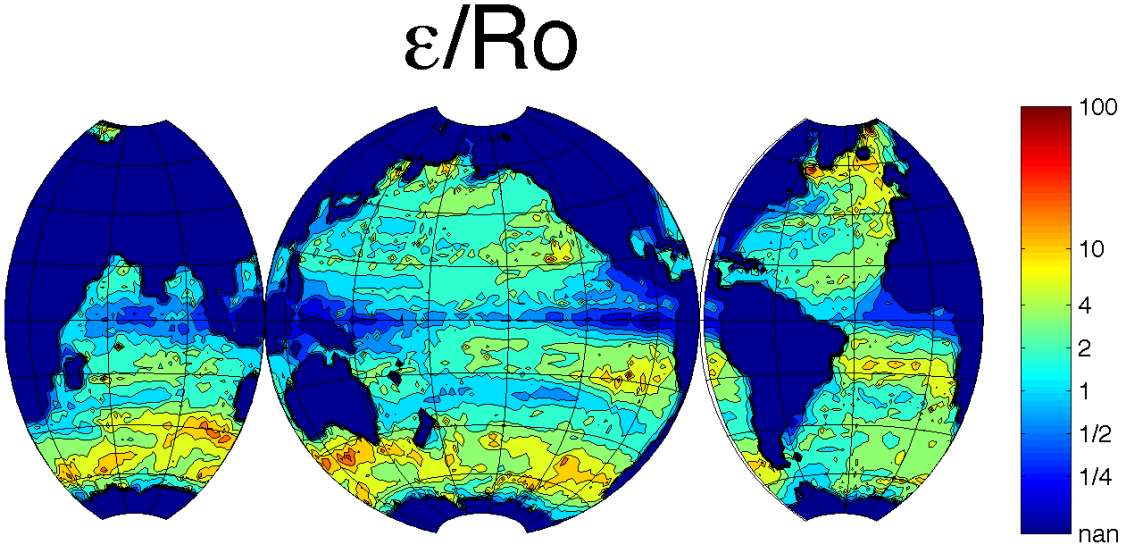

Figure 1.7: Figure 1 from McWilliams and Fox-Kemper (2013). $\epsilon \equiv \frac{U^S H}{fLH^S}$ shows the strength of the Stokes shear force perturbation from hydrostatic balance.

Malecha et al. (2014) show in a multi-scale simulation that LC interact with internal waves. The interaction is strongly non-linear and results in strong cross cell (i.e. across the LC cells) and vertical velocities and vertical vorticity. The inertial wave modulates the strength and depth of the LC.

Li et al. (2012) show the existence of a hybrid LC/SI mode in a strong submesoscale front with Stokes drift in Lagrangian thermal wind balance. This hybrid mode grows significantly faster than SI in the absence of Stokes drift. They perform nonlinear simulation that show the hybrid mode restratifies the front at an even faster rate than is typical of MLEs. This is contrary to the view that wave forcing induces mixing, and rather suggests that Stokes drift may play a stabilizing role in mixed layer dynamics.

Hamlington et al. (2014) performed Large Eddy Simulations (LES) of a submesoscale front with and without Stokes drift. Their results indicate that Stokes drift enhances vertical mixing, and likely increases the MLD. Furthermore, they find that the prevalence of SI is reduced by a third when Stokes drift forcing is present. In both of their runs, the wind direction was dominantly down-front, and the wind and waves were aligned. This configuration is favorable for FSI in both cases, but Stokes drift apparently makes for less favorable conditions (see chapter 4). Furthermore, destruction of the mean shear by LC may reduce the shear available for SI.

1.5 Length and Time Scales of Mixed Layer Dynamics

The previous sections all discuss coherent structures and instabilities in the mixed layer which occur on different length and time scales. The MLEs have been shown to scale with Ri and the mixed layer deformation radius

$$L = 2\pi L_d \left(\frac{2(1+Ri)}{5} \right)^{\frac{1}{2}} \tag{1.23}$$

L is $O(1-10\ km)$ for the mixed layer. The timescale (τ) for MLEs is given by

$$\tau = \frac{1}{f} \left(\frac{54(1+Ri)}{5} \right)^{\frac{1}{2}} \tag{1.24}$$

τ is $O(1\ day)$ for the mixed layer.

The length scale for LC is observed to be highly variable. There are suggestions that it may relate to the depth scale of the Stokes drift (H^S) which directly relates to the wavelength of the waves (k_w) for a monochromatic wave.

$$L \sim H^S = \frac{1}{2k_w} \tag{1.25}$$

For a wave with a 5 s period, using the deep water dispersion relation to find k_w, $L \sim 3\ m$. However, since LC also extract energy from the Eulerian shear, the Ekman depth (H^E) is also an important length scale.

$$H^E = \sqrt{\frac{2\nu}{f}} \tag{1.26}$$

The Ekman depth ranges from a few to a few tens of meters. This and the observed length scales of LC ($1 - 200\ m$) give a range for the length scale of LC. If we consider a typical Stokes drift magnitude ($\sim 0.05m\ s^{-1}$), or observed vertical velocities in LC ($\sim 20\ cm\ s^{-1}$; Smith (1992)), a range of timescales for LC can be formed from the length and velocity scales which ranges from $5\ s - 1\ h$.

Lastly, the length and time scales for SI fall in between. A typical length scale for SI is $O(100\ m)$. Haine and Marshall (1998) give the timescale for SI as

$$\tau \sim \frac{2\pi\sqrt{-\hat{q}}}{f}, \tag{1.27}$$

where $\hat{q} \equiv \frac{fq}{M^4}$, and q is the Ertel PV. In the case of only geostrophic shear, $\hat{q} = Ri - \frac{f}{\zeta}$, where $\zeta = u_y - f$. This gives a timescale of $3 - 10\ h$.

These disparate length and timescales make it exceedingly difficult to both measure and simulate these phenomena. This strongly motivates the development of scaling laws that are broadly applicable. The scales for growth rate wavenumber of MLE's as a function of Ri are a good example of this because they illustrate how the large scale mean flow properties (such as Ri) influence the turbulent motions. But beyond that we would like to develop how the net effect of the turbulent motions changes the mean flow. For example Fox-Kemper

et al. (2008) have given a scaling for the buoyancy production done by MLEs as a function of mean mixed layer depth and stratification, however, we do not yet know how this varies in the presence of Stokes drift. Similarly, there have been several quantifications of the mixing due to LC, but it is not yet clear how those change in the presence of MLEs or SI.

This scaling law approach is extremely useful for both observations and large scale (climate scale) models. If one wants to observe any of these phenomena in the ocean, the length and time scales that depend on easily observed quantities of the mean flow (e.g. Ri or wavelength of surface gravity waves) are very useful. Furthermore, such scalings provide a good way to interpret observed data in which the contributing mechanisms, for example, vertical kinetic energy are not always clear. In climate scale models, none of these processes are resolved due to computational limits, yet they have been shown to have an effect on the mean stratification and flow. Eventually, computational resources will be able to simulate climate down to these small length and time scales, but that is decades if not centuries away. Therefore, in the interim, we use simple, but widely applicable scaling laws to parametrize these sub-grid scale physical phenomena.

It is the goal of this work to show how these phenomena change in the presence of each other. Growth rates, and energy production terms will be scaled in terms of the dimensionless parameters that describe the mean flow. In this way we can see how the MLEs, SI, and LC all contribute to mixing of momentum and buoyancy in the mixed layer under different scenarios of waves, winds, and fronts.

Chapter 2

Restratification of Hurricane Wakes: A Special Case

When a hurricane passes over the ocean, it leaves behind a wake of relatively cold sea surface temperature (SST). This cold wake is sometimes even visible in satellite SST images (see figure 2.1). This temperature anomaly extends through the mixed layer, which has been deepened by the strong momentum flux into the ocean. The result is a cold wake with a deep mixed layer bounded on either side by a comparatively warm and shallow mixed layer. This scenario provides a unique an interesting context in which to study how the effects of surface heat fluxes compare to adiabatic processes that also affect the mixed layer stratification. Furthermore, remote sensing data (satellite SST) allows us to diagnose most of the wake parameters required to estimate timescales for restratification. Certainly in situ measurements of the wake parameters would be superior, but even without them, the derived scalings give good estimates of wake restratification time. The majority of this chapter has been published in (Haney et al., 2012, Appendix A).

2.1 Background

The motivations to better understand the structure, and restratification of hurricane wakes range from possible climatic consequences through altered ocean heat transport (Emanuel, 2001; Pasquero and Emanuel, 2008), to changes for fisheries due to changes in the stratification, and therefore the concentration of phytoplankton. Regardless of the broader motivation, hurricane wakes provide a special case in which the surface heat fluxes are out

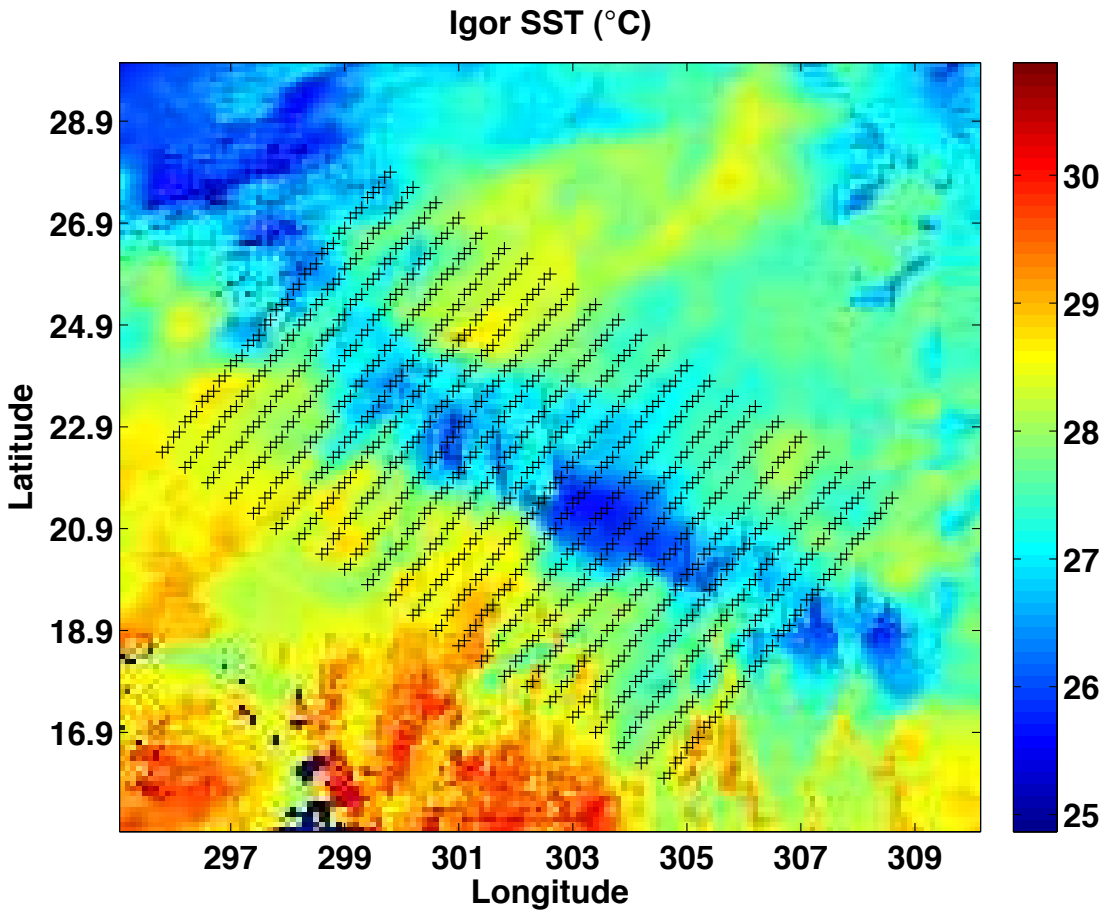

Figure 2.1: Figure 6 from (Haney et al., 2012, Appendix A). SST on September 19, 2010, ≈ 2 days after Hurricane Igor passed over the region. The 'x' marks show where the temperature is sampled to estimate the cross track temperature difference.

of equilibrium, and potential energy in the fronts on either side of the wake is available.

The formation of hurricane wakes has been well studied, and one robust result of these studies is that the hurricane wake forms primarily as a result of mixing rather than heat loss to the atmosphere (D'Asaro et al., 2007; Huang et al., 2009; Zedler et al., 2009). This observation will be a critical assumption in computing the depth of the wake. Studies of hurricane wake recovery are less prevalent. Price et al. (2008) uses a $1D$ model (Price et al., 1986) to study the recovery of the wakes of Hurricanes Fabian and Frances. Although the $1D$ approach does a good job of predicting the observed SST, other processes may play a more dominant role in influencing the temperature anomaly in deeper parts of the wake. Mrvaljevic et al. (2013) showed that during Typhoon Fanapi, the the recovery of a sub-surface bolus of well mixed water took nearly twice as long as the recovery of the SST. Numerical modeling of a hurricane wake also confirms the presence of the sub-surface bolus, particularly in the absence of MLEs (Haney et al., 2012).

Several $2D$ and $3D$ dynamical processes have been shown to influence the stratification near fronts (Thomas and Ferrari, 2008; Fox-Kemper et al., 2008). Depending on the orientation of the wind and the front, the resulting Ekman transport may restratify or de-stratify the mixed layer. This effect is referred to as the Ekman buoyancy flux (EBF) Thomas (2005). As mentioned previously, MLEs may extract available potential energy from the fronts on either side of the wake, thereby restratifying it. Timescales for restratification for each of these two mechanisms are developed based on the parameters of the wake. These timescales are compared to the time for thermal restratification by the surface fluxes (SF) to estimate the importance of adiabatic vs diabatic processes. Lastly, due to the observational and model evidence that the near surface layer restratifies faster than the sub-surface bolus, separate restratification times are derived for each process in each of these layers.

2.2 Restratification Timescales

The goal here is to estimate the time required for three mechanisms to restratify a hurricane wake independent of other forcing. Furthermore, it is desirable to estimate these timescales from a combination of remotely observed and estimated parameters of the hurricane wake. The minimum necessary parameters to obtain timescales for restratification by SF, EBF, and MLE are depicted in the wake schematic (figure 2.2).

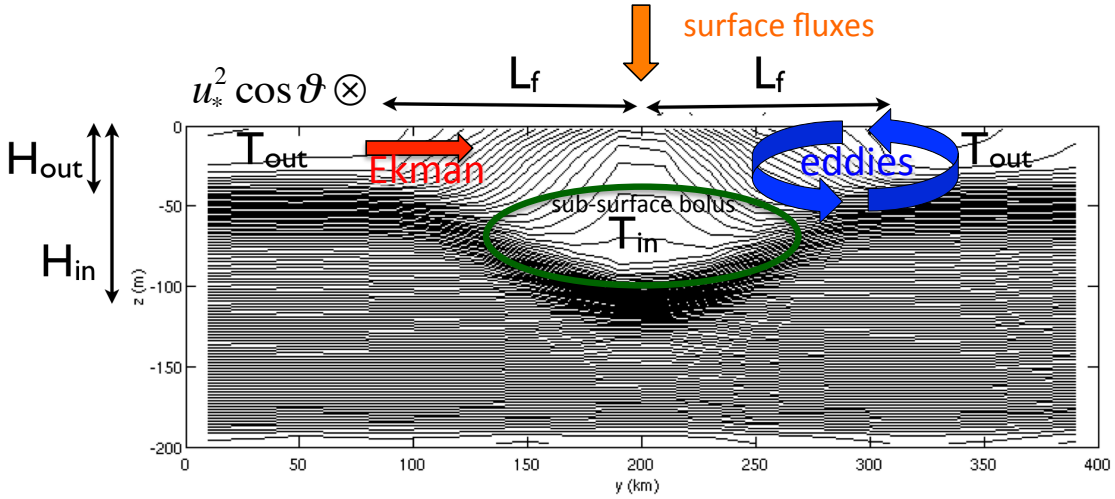

Figure 2.2: Figure 2 from (Haney et al., 2012, Appendix A). Schematic diagram of cold wake during restratification. The thin black lines are isotherms. Temperatures T_{out}, T_{in}, mixed layer thicknesses H_{out}, H_{in}, front width L_f, and friction velocity squared in the along track direction of the hurricane $u_* \cos\theta$ are indicated. Each restratification mechanism discussed is also depicted, and the region referred to as the sub-surface bolus is shown.

2.2.1 Surface Heat Fluxes

Previous work on wake restratification considered the primary mechanism to be a balance of surface heat and momentum fluxes Price et al. (2008). Put more simply, the wake is restored by solar heating, some of which is mitigated by vertical mixing of that heat. The vertical mixing can be interpreted as influencing the depth over which the heat is distributed, so for a fixed depth, the problem is reduced to computing the net heat flux anomaly at the

surface. The primary assumption is that outside the wake, the net heat flux is zero, and the temperature is steady.

$$\rho C_p H_{out} \frac{\partial T_{out}}{\partial t} = -Q_{out} + S^0_{H_{out}} = 0, \tag{2.1}$$

where Q_{out} is the sensible, infrared, and latent heat flux from ocean to atmosphere, and $S^0_{H_{out}}$ is solar heating from the surface down to H_{out}. In reality, the temperature is not steady, but rather fluctuates with the diurnal cycle of solar heating during the day, and latent and sensible heat loss at night. The diurnal cycle is well addressed in the $1D$ model in Price et al. (2008), and the goal here is not to improve upon that, but rather to compare a rough estimate of the $1D$ diabatic fluxes with $2D$ amd $3D$ adiabatic fluxes. As such, we neglect the diurnal cycle, assuming that outside the wake, the net heat content change is zero over one period of the diurnal cycle.

Now, assuming that the heat flux from ocean to atmosphere in the wake can be linearly related to the SST difference, the heat flux within the wake is given by

$$\rho C_p H' \frac{\partial T_{in}}{\partial t} = -Q_{out} + C_{sst}(T_{out} - T_{in}) + S^0_{H'}, \tag{2.2}$$

where $C_{SST} \approx 50 \pm 10 W m^{-1} K^{-1}$ (Large and Yeager, 2012) relates the SST difference to the heat flux difference, and $S^0_{H'}$ is the solar heating down to a depth H'. The choice of restratification depth H' is left open because the SF are not expected to be effective over the full depth of the wake H_{in} (nor are EBF). Furthermore, as stated previously, the depth over which the surface heat flux is distributed changes, however, in order to provide a simple scaling for the restratification time, we bound the restratification depth $H_{out} < H' < H_{in}$. Since SF are distributed by turbulent momentum fluxes that determine the MLD, L_O is a natural choice for H'. Inserting the relevant wake parameters into 1.1 yields

$$L_O = \frac{\rho C_p T_{in} u_*^3}{kg(-Q_{out} + C_{sst}(T_{out} - T_{in}) + S_0 I_2)}, \tag{2.3}$$

where $S_0 I_2$ approximates the solar heating term $S^0_{H'}$. Unfortunately, L_O is extremely sensitive to the surface wind stress, which varies rapidly in strength and direction over the recovery

period of a hurricane wake. As such, H_O is not chosen as a bound for H'. Lastly, the particular choice of H' does not affect the functional form of any of the restratification timescales (so long as H' is constant), but it does change the temperature to which the wake returns. The final temperature (T_f) of the recovered wake is determined by considering no net heat flux at the surface (i.e. the steady state case of 2.2)

$$T_f = T_{out} - \frac{1}{C_{sst}} S_{H'}^{H_{out}} \tag{2.4}$$

For $H' = H_{out}$, T_f is simply T_{out}. Integrating 2.2 from T_{in} to T_f gives the timescale for SF restratification

$$\tau_{SF} = \frac{\rho C_p}{C_{sst}} H', \tag{2.5}$$

and through a remarkably convenient coincidence of the proportionality constants,

$$\tau_{SF}(in\ days) \approx H'(in\ meters).$$

2.2.2 Restratification by EBF

Undoubtedly, the wake will be subjected to surface wind forcing throughout the recovery period. If the wind stress is directed up (down) front, i.e. opposing (coinciding with) the geostrophic shear, the resulting Ekman transport will be restratifying (de-stratifying) (Thomas, 2005; Thomas and Ferrari, 2008). Furthermore, up (down) front wind stress results in an injection (extraction) of PV, reducing (increasing) the likelihood of FSI (Thomas et al., 2013). The Ekman transport is given by $\frac{u_*^2}{f\delta}$, where δ, the Ekman layer depth, is assumed to be H'. Then a timescale for EBF restratification is given by

$$\tau_{EBF} = \frac{wake\ width}{Ekman\ Flow} = 2\frac{L_f f H'}{u_*^2 cos\theta}. \tag{2.6}$$

It should be noted that the EBF do not heat the wake, as with SF, but EBF advect warm water outside the wake onto the wake. If this effect was uniform over H_{in}, then EBF would merely translate the wake in space, however, as with SF, EBF are unlikely to penetrate

to H_{in}. Therefore EBF act to seal the deeper portion of the wake (between H_{in} and H'), isolating it from surface heat and momentum fluxes.

2.2.3 Restratification by MLEs

The success of the MLE parametrization in general (Fox-Kemper et al., 2008) and in a simulated hurricane wake (Haney et al., 2012), suggests that its use would be ideal in estimating a restratification timescale by MLEs when only the minimal number of parameters is known. The parametrization is formulated as an eddy induced stream function from which may be written in terms of the wake parameters as follows

$$\begin{aligned} |\mathbf{\Psi}| &= C_e \frac{H_{eddy}^2 (b_{out} - b_{in})}{L_f |f|} \mu(z), \\ \mu(z) &= \max\left\{0, \left[1 - \left(\frac{2z}{H} + 1\right)^2\right]\left[1 + \frac{5}{21}\left(\frac{2z}{H} + 1\right)^2\right]\right\}, \end{aligned} \tag{2.7}$$

where $H_{eddy} \approx \frac{1}{2}(H_{in} + H_{out})$, and $C_e \approx 0.06$ is an efficiency factor (Fox-Kemper et al., 2008; Bachman and Fox-Kemper, 2013).

First, the fastest possible MLE restratification timescale is estimated as the time for the eddy induced surface velocity $\left|\frac{\partial \mathbf{\Psi}}{\partial z}\right|_{z=0}$ to seal the surface of the wake by advecting warm water across it.

$$\frac{L_f}{\left|\frac{\partial \mathbf{\Psi}}{\partial z}\right|_{z=0}} \approx \frac{0.2}{C_e g \alpha} \frac{L_f^2 \, |f|}{H_{eddy}(T_{out} - T_{in})} = \tau_{eddy}. \tag{2.8}$$

Although τ_{eddy} is unlike τ_{SF} and τ_{EBF} in that it reflects only the surface sealing rather than the restratification of the buoyancy anomaly over H', it is found to be a more robust estimate of the timescale because it is less sensitive to variation in the horizontal buoyancy gradient.

A wake sealing time is inappropriate for use in the sub-surface bolus, and therefore the along isopycnal buoyancy fluxes are computed from the stream function and buoyancy anomaly. The timescale for restratification by the vertical buoyancy flux is given by

$$\begin{aligned} \tau_{ev} &= \frac{\int_{-H_{in}}^{-H'} \int_0^{L_f} b' \, dy \, dz}{\int_0^{L_f} |\overline{w'b'}|_{z=-H_{eddy}} \, dy} \\ &\approx \frac{1}{C_e g \alpha} \frac{(H_{in} - H') L_f^2 |f|}{H_{eddy}^2 (T_{out} - T_{in})} \end{aligned} \tag{2.9}$$

The timescale for restratification by the horizontal buoyancy flux is given by

$$\begin{aligned}\tau_{eh} &= \frac{\int_{-H_{in}}^{-H'}\int_0^{L_f} b'\,dx\,dz}{\int_{-H_{eddy}}^{-H'}|\overline{v'b'}|\,dz} \\ &\approx \frac{1}{m(\gamma)C_e g\alpha}\frac{(H_{in}-H')L_f^2|f|}{H_{eddy}^2(T_{out}-T_{in})}\end{aligned} \tag{2.10}$$

where $\gamma = \frac{H'}{H_{eddy}}$, and $m(\gamma) = \frac{4}{63}(-1+\gamma)^2(11+22\gamma-6\gamma^2+12\gamma^3)$ is a dimensionless constant representing the strength ($\mu(z)$) of the stream function between H' and H_{eddy}. For the cyclones studied here: $0.34 \leq m(\gamma) \leq 0.56$.

2.3 Applying the Scalings

The timescales for each restratification process in section 2.2 are applied to four cyclones. The relevant parameters, as in figure 2.2, for each of Hurricanes Frances, Igor, and Katrina, and Typhoon Fanapi are given in table 2.1

Cyclone	Fanapi	Frances	Igor	Katrina
Date	9/19/2010	9/02/2004	9/19/2010	9/04/2005
Location	$22.5N\ 127.5E$	$20.4N\ 61W$	$22.4N\ 57.5W$	$26.4N\ 86W$
$T_{in}(\,^\circ\mathrm{C})$	$26.3+0.6$	$26.72+0.08$	$25.63+0.06$	$28.1+0.2$
$T_{out}(\,^\circ\mathrm{C})$	29.37 ± 0.05	28.35 ± 0.04	28.36 ± 0.08	29.44 ± 0.06
$L_f(km)$	260^{+50}_{-40}	280 ± 60	20^{+20}_{-40}	160_{-30}
$u_*^2 cos\theta(10^{-5}m^2/s^2)$	8 ± 6	8 ± 3	8 ± 4	7 ± 7
$H_{out}(m)$	55	30	26	15
$H_{in}(m)$	163	120	160	89

Table 2.1: Table 1 adapted from (Haney et al., 2012, Appendix A). Table of values for cold wakes used in this study as estimated from data, showing temperatures T_{out}, T_{in}, mixed layer thicknesses H_{out}, H_{in}, front width L_f, and friction velocity in the along track direction of the hurricane $u_* \cos\theta$. Note, the dates reflect when the wake is first visible in satellite SST images, rather than the date that the hurricane was at that physical location.

As stated previously, H' is bounded by H_{out} and H_{in}, so the bounding restratification times for each wake are given in figure 2.3. Actual restratification times for each wake are determined from satellite SST images (details in Haney et al. (2012)), and are included for comparison to the scalings. In all cases, the actual restratification time is considerably

shorter than the timescale for any individual process. This is unsurprising since recovery of the SST does not reflect a recovery over the full depth of the wake, H_{in}, but rather a thin surface layer. Furthermore, since none of the isolated restratification mechanisms ever acts alone (at least not near the surface), the restratification time for all the processes acting in concert would be shorter. For example, in the case of Typhoon Fanapi, considering the effects of SF and EBF yields an e-folding time of 29 days which is comparable to the observed e-folding time of 23 days given by Mrvaljevic et al. (2013)

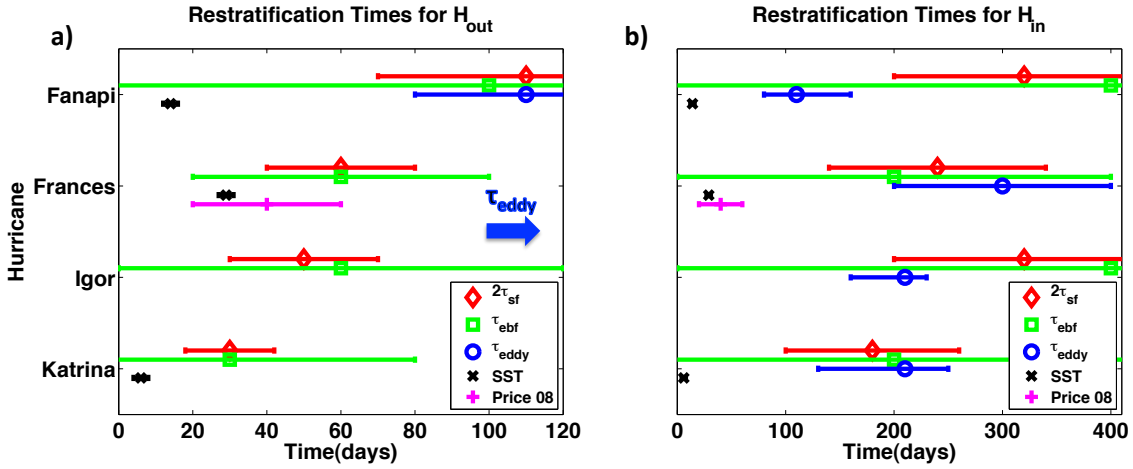

Figure 2.3: Figure 5 from (Haney et al., 2012, Appendix A). Restratification times for each cyclone. Error bars represent the 90% confidence interval. The Price et al. (2008) e-folding time has been doubled to compare more directly to the other times that represent full restratification.

In general, the SF and EBF timescales are comparable when the restratifying depth is shallow (H_{in}), although The error in τ_{EBF} is quite large due to the significant variability in wind strength and direction over the recovery period. If the restratifying depth is very deep (H_{in}), then the eddies compete with or are even faster than (e.g. in Typhoon Fanapi) SF and EBF. Although a restratifying depth of H_{in} is unlikely, this case provides an upper bound on the timescales. More importantly, the H_{in} case highlights the sensitivity of the restratification time to the wake depth, where τ_{eddy} is literally off the chart in the $H' = H_{out}$

case, and dominant in the $H' = H_{in}$ case. This is clear from the scalings since $\tau_{SF}, \tau_{EBF} \sim H'$, whereas $\tau_{eddy} \sim \frac{1}{H'}$.

The only mechanisms which can possibly restratify the deep bolus are SF and MLEs. The SF timescale is strictly given by the solar heating rate since the concept of the bolus implies that it does not exchange water with the near surface, and presumably already restratified, portion of the mixed layer. This timescale is also derived from equation 2.2, but the surface flux term is neglected, and the solar heating term is integrated only over the depth of the bolus. Since solar heating decays exponentially from the surface, this term is expected to be small, and this is confirmed by the timescales in table 2.2.

Cyclone	$\tau_{ev}(days)$	$\tau_{eh}(days)$	$\tau_{sb}(10^5 days)$	$\tau_{eh+ev}(days)$
Fanapi	500^{+200}_{-100}	$1,600^{+700}_{-400}$	$100,000 \pm 30,000$	400^{+200}_{-100}
Frances	$1,900 \pm 800$	$4,000 \pm 2,000$	8 ± 0.2	$1,300 \pm 500$
Igor	$1,500^{+200}_{-400}$	$2,700^{+300}_{-700}$	5 ± 0.2	$1,000^{+100}_{-200}$
Katrina	$1,400^{+200}_{-600}$	$3,000^{+500}_{-1,000}$	0.05 ± 0.03	$1,000^{+200}_{-400}$

Table 2.2: Table 4 adapted from (Haney et al., 2012, Appendix A). Restratification timescales for the subsurface bolus. $H^{'} = H_{out}$. Note that the different columns have different units.

Although it is the most effective restratification mechanism in the bolus, the eddy buoyancy fluxes are still quite slow due to the wide fronts on either side of these wakes. The vertical buoyancy fluxes are generally twice as effective as the horizontal buoyancy fluxes, but even their combined effect results in restratification times longer than a year in all cases. This suggest hurricane wakes may have a long lasting signal if the sub-surface bolus is not eroded by MLEs sufficiently quickly.

To address the potential of a long lasting sub-surface bolus, I considered the climatological wintertime MLD (MLD_w) near each wake and compared it to H_{in}. If the wintertime mixed layer is as deep or deeper than the wake depth, the bolus would be consumed by and become part of the winter mixed layer. In each case $H_{in} > MLD_w$, however since MLD_w is a monthly climatology, it is an underestimate of the absolute maximum MLD. Furthermore,

once $MLD_w > H_{out}$, i.e. once the wintertime mixed layer has entrained some bolus water, the comparatively warm bolus water could further the wintertime mixed layer deepening. The source of heat in the bolus would increase the mixed layer temperature, and therefore the surface heat flux (to the atmosphere) that results in the convection that deepens the mixed layer.

The strong dependence of wake restratification time on the wake parameters highlights that hurricane wakes are not far from a parameter regime in which $2D$ and $3D$ dynamical processes can become more important than the diabatic surface fluxes. This is made especially clear by considering the $H' = H_{in}$ case, but τ_{eddy} would also be rapidly reduced in the case of a narrower front since $\tau_{eddy} \sim L_f^2$ (while $\tau_{EBF} \sim L_f$, and τ_{SF} is independent of L_f). Furthermore, the while the dynamical effects of MLEs on the thermal stratification were considered, their effect on the MLD itself was not sufficiently addressed here. In fact the dynamical effect on MLD was only briefly touched upon through the influence of the wind on L_O (equation 2.3).

As alluded to in chapter 1, there are relevant turbulent fluxes that are intrinsic to the ocean (rather than fluxes through the surface) that influence the MLD, and MLEs are one of them. This chapter has shown that the special case of hurricane wakes represents a parameter regime not far from where the conservative mixed layer dynamics are competitive with diabatic forcing from the atmosphere. The fronts on the edges of these wakes were all $O(100\ km)$ an with weaker buoyancy gradients than fronts in the ocean on the submesoscale ($O(10\ km)$). As is evident in the eddy sealing time (equation 2.8), a stronger, narrower front dramatically increases the effect of the eddies. Furthermore very strong fronts may open up the possibility of a new class of instabilities such as SI. Lastly, this chapter neglected any wave effects because the instability they induce, LC, is thought to mix rather than restratify the upper ocean. This provides a competing mechanism for the restratification mechanisms due to diabatic fluxes from the atmosphere, and induced by strong fronts. In the subsequent chapters, the focus will be restricted to adiabatic dynamics which are primarily intrinsic to

the ocean (though the influence of the wind will still be relevant). These dynamics will first be investigated in chapters 3-4 through linear instabilities of mean flows that are characteristic of all, or parts, of the mixed layer. Then the fully non-linear dynamics will be explored with large eddy simulations (LES).

Chapter 3

Numerical Linear Stability: Model Validation

Several linear stability problems have been formulated in the past in order to characterize the instability processes that lead to coherent structures and turbulence in the mixed layer. Unfortunately, none of these past formulations has encompassed all of the disparate instability types that exist in the mixed layer which range from strongly sheared boundary layer turbulence to strongly stratified and rotating turbulence. In this chapter, I develop a linear stability model beginning from the WAB equations (3.1-3.3), and scale them appropriately to allow a smooth transition between these disparate stability regimes.

$$\partial_t \mathbf{u} + (\mathbf{u}^L \cdot \nabla)\mathbf{u} + f\hat{k} \times \mathbf{u}^L + \nabla p + u^{L,j}\nabla U^{S,j} = b\hat{k} + \nu\nabla^2\mathbf{u}. \tag{3.1}$$

$$\partial_t b + (\mathbf{u}^L \cdot \nabla)b = \kappa\nabla^2 b, \tag{3.2}$$

$$\nabla \cdot \mathbf{u} = 0, \tag{3.3}$$

3.1 Model Setup

First, the flow is decomposed into mean and perturbation parts (i.e. $u = \overline{U} + u'$, and similarly for other flow variables) by assuming multiple scales of horizontal variation, which allows for fast and slow timescales.

$$\hat{\partial}_x \rightarrow \frac{1}{l}\partial_x + \frac{1}{L}\partial_X, \tag{3.4}$$

$$\hat{\partial}_t \rightarrow \frac{U}{l}\partial_t + \frac{U}{L}\partial_T \tag{3.5}$$

The mean flow is obtained by averaging over the fast timescale and small horizontal space scales.

$$\overline{(\cdot)} = \frac{U}{l^3} \int^t \int^x \int^y dxdydt \tag{3.6}$$

A set of dimensional scales is then chosen based on realistic scales for the mixed layer (table 3.1). Length, time, and horizontal velocity scales are fixed, and vertical velocity, pressure, and buoyancy scales are derived therefrom. The pressure scaling ($M_r = max(1, Ro^{-1})$) is chosen to switch between scaling with the velocity head, and the Coriolis force as in McWilliams (1985) to allow for a full range of non-rotating to rapidly rotating flows. The Lagrangian velocity is chosen so that Stokes drift has an effect on the size of the velocity scale, and so that it will not vanish without Stokes drift. A separate vertical scale is given as the e-folding depth of the Stokes drift (H^S). The perturbation velocities scale a factor of $\delta \equiv \frac{l}{L}$ smaller than their mean velocity counterparts.

$$u' \sim \delta|\overline{U}| \tag{3.7}$$

The perturbation pressure and buoyancy terms have a similar scale switch ($M_r' = max(1, \delta Ro^{-1})$) to go between rapidly ($\delta Ro^{-1} >> 1$) and slowly ($\delta Ro^{-1} << 1$) rotating perturbed motions. Lastly, the Ekman number Ek is used here since it will prove useful in defining the Ekman depth. In case of any confusion, the reader is reminded that the Reynolds number relates to the Ekman number through the Rossby number $Re = \frac{Ro}{Ek}$. Since I will only be exploring the limits of Ro, there are no concerns about inadvertently making the problem inviscid when it becomes strongly rotating. The non-dimensional numbers that may be formed from these dimensional scales can be found in table 3.2

Dimensional Variable	Scaling	Typical Value
f	f	$8.34 \times 10^{-5}\ s^{-1}$
b_z	N^2	$6.96 \times 10^{-7}\ s^{-2}$
b_Y	M^2	$6.96 \times 10^{-8}\ s^{-2}$
∂_z^{-1}	H	$50\ m$
∂_X^{-1}	L	$5\ km$
∂_x^{-1}	l	$50\ m$
u, v	$U^L \equiv \lvert\mathbf{U} + \mathbf{U}^S\rvert_{z=0}$	$0.06\ ms^{-1}$
U^S, V^S	$\lvert\mathbf{U}^S\rvert_{z=0}$	$0.05\ ms^{-1}$
H^S	H^S	$1 - 10\ m$
w	$\frac{U^L H}{l}$	$0.06\ ms^{-1}$
π	$U^{L,2} M_r$	$0.036\ m^2 s^{-2}$
b	$\frac{U^{L,2}}{H} M_r$	$0.007\ ms^{-2}$
ν	ν	$10^{-6} m^2 s^{-1}$
κ	κ	$1.4 \times 10^{-7} m^2 s^{-1}$

Table 3.1: The scalings for the dimensional variables, and their typical values in the ocean mixed layer. The buoyancy frequency, N^2 and geostrophic shear $\frac{M^2}{f}$ are consistent with those reported in Boccaletti et al. (2007). The surface Stokes drift magnitude, $|\mathbf{U}_s(0)|$, is consistent with that reported in Webb and Fox-Kemper (2011).

Non-dimensional number	Definition	Possible Range	Typical Range
Ro	$\frac{U^L}{fL}$	$(0, \infty)$	$[10^{-}2, 10^3]$
Ri	$\frac{N^2 H^2}{U^{L,2}}$	$[0, \infty)$	$[10^{-10}, 10]$
α	$\frac{H}{L}$	$<< 1$	$[10^{-}5, 10^{-2}]$
μ	$\frac{U^S}{U^L}$	$[0, \infty)$	$[0, 10^3]$
λ	$\frac{H}{H^S}$	$(0, \infty)$	$[5, 50]$
γ	$\frac{U_z^g}{U_z^L} \equiv \frac{M^2 H}{f U^L}$	$[0, 1]$	$[0, 1]$
δ	$\frac{l}{L}$	$<< 1$	$[10^{-4}, 1]$
M_r	$max(1, Ro^{-1})$	$[1, \infty)$	$[1, 100]$
M_r'	$max(1, \delta Ro^{-1})$	$[1, \infty)$	$[1, 100]$
Ek	$\frac{\nu}{fL^2}$	$[0, 1)$	$[10^{-}15, 10^{-}5]$
Pr	$\frac{\nu}{\kappa}$	~ 7	~ 7

Table 3.2: Non-dimensional numbers and their range of values that may be explored by this equation set. Note that all non-dimenstional parameters involving a velocity contain the *Lagrangian* rather than Eulerian velocity.

Applying these scalings to the WAB equations (1.4-1.6) gives a complete set of mean and perturbation equations which may be used to explore the vast parameter space that is alluded to by the size of table 3.2.

$$\begin{aligned} Ro\left[\overline{\mathbf{U}}_T + (\overline{\mathbf{U}}^L\cdot\nabla_H)\overline{\mathbf{U}} + M_r\nabla_H\overline{P}\right] + \frac{Ro}{\delta}\overline{W}\ \overline{\mathbf{U}}_z + \hat{\mathbf{k}}\times\overline{\mathbf{U}}^L + \\ -Ek\nabla_H^2\overline{\mathbf{U}} - \frac{Ek}{\alpha^2}\overline{\mathbf{U}}_{zz} + \\ Ro\left[\mathbf{u}'_t + (\overline{\mathbf{U}}^L\cdot\nabla_h)\mathbf{u}' + \overline{W}\mathbf{u}'_z + w'\ \overline{\mathbf{U}}_z + M'_r\nabla_h p'\right] + \delta\hat{\mathbf{k}}\times\mathbf{u}' + \\ -\frac{Ek}{\delta}\nabla_h^2\mathbf{u}' - \delta Ek\nabla_H^2\mathbf{u}' - \frac{\delta Ek}{\alpha^2}\mathbf{u}'_{zz} + \\ Ro\delta\left[\mathbf{u}'_T + (\overline{\mathbf{U}}^L\cdot\nabla_H)\mathbf{u}' + (\mathbf{u}'\cdot\nabla_H)\overline{\mathbf{U}} + M'_r\nabla_H p'\right] + \\ \delta^2 Ro\left[(\mathbf{u}'\cdot\nabla_H)\mathbf{u}'\right] + Ro\delta\left[w'u'_z + (\mathbf{u}'\cdot\nabla_h)\mathbf{u}'\right] = 0 \end{aligned} \tag{3.8}$$

$$\begin{aligned} \frac{Ro\alpha^2}{\delta}\left[\overline{W}_T + (\overline{\mathbf{U}}^L\cdot\nabla_H)\overline{W}\right] + Ro\left(\frac{\alpha}{\delta}\right)^2\overline{W}\ \overline{W}_z + \mu\lambda Ro\overline{\mathbf{U}}^L\cdot\mathbf{U}_z^S + \\ RoM_r\left[\overline{P}_z - \overline{B}\right] - \frac{Ek\alpha^2}{\delta}\nabla_H^2\overline{W} - \frac{Ek}{\delta}\overline{W}_{zz} + \\ \frac{Ro\alpha^2}{\delta}\left[w'_t + (\overline{\mathbf{U}}^L\cdot\nabla_h)w' + \overline{W}w'_z + w'\overline{W}_z\right] + \mu\lambda Ro\delta\mathbf{u}'\cdot\mathbf{U}_z^S + Ro\delta M'_r\left[p'_z - b'\right] + \\ -\frac{Ek\alpha^2}{\delta^2}\nabla_h^2 w' - Ek\alpha^2\nabla_H^2 w' - Ekw'_{zz} + \\ Ro\alpha^2\left[w'_T + (\overline{\mathbf{U}}^L\cdot\nabla_H)w' + (\mathbf{u}'\cdot\nabla_H)\overline{W} + (\mathbf{u}'\cdot\nabla_h)w' + w'w'_z\right] + \\ Ro\alpha^2\delta(\mathbf{u}'\cdot\nabla_H)w' = 0 \end{aligned} \tag{3.9}$$

$$\begin{aligned} \overline{B}_T + \frac{\gamma}{RoM_r}(\overline{\mathbf{U}}^L\cdot\nabla_H)\overline{B} + \frac{Ri}{\delta M_r}\overline{W}\ \overline{B}_z - \frac{Ek}{RoPr}\nabla_H^2\overline{B} - \frac{Ek}{RoPr\alpha^2}\overline{B}_{zz} + \\ \frac{M'_r}{M_r}\left[b'_t + (\overline{\mathbf{U}}^L\cdot\nabla_h)b' + \overline{W}b'_z\right] + \frac{\delta\gamma}{RoM_r}(\mathbf{u}'\cdot\nabla_H)\overline{B} + \frac{Ri}{M_r}w'\overline{B}_z + \\ -\frac{EkM'_r}{M_rRoPr\delta}\nabla_h^2 b' - \frac{Ek\delta M'_r}{M_rRoPr}\nabla_H^2 b' - \frac{Ek\delta M'_r}{M_rRoPr\alpha^2}b'_{zz} + \\ \frac{\delta M'_r}{M_r}\left[b'_T + (\overline{\mathbf{U}}^L\cdot\nabla_H)b'\right] + \frac{\delta^2 M'_r}{M_r}(\mathbf{u}'\cdot\nabla_H)b' + \frac{\delta}{M_r}\left[(\mathbf{u}'\cdot\nabla_h)b' + w'b'_z\right] = 0 \end{aligned} \tag{3.10}$$

$$\nabla_H\cdot\overline{\mathbf{U}} + \frac{1}{\delta}\overline{W}_z + \delta\nabla_H\cdot\mathbf{u}' + \nabla_h\cdot\mathbf{u}' + w'_z \tag{3.11}$$

In this chapter, it will be demonstrated that five regimes of interest can be explored with 3.8-3.11: QG motions; submesoscale flows; the vertically stratified Stokes drift layer that admits LC instabilities; the Stokes-Ekman layer; and the Stokes-Front layer.

3.1.1 Numerical Implementation

While some special cases with strict assumptions can be solved analytically (see section 4.1), in general, equations 3.8-3.11 will be solved with a linear numerical code by assuming enough to neglect the nonlinear terms. I also assume a normal mode form for the perturbations

$$u' = \tilde{u}(z)e^{ikx+ily-i\sigma t}, \tag{3.12}$$

and similarly for v', w', b', and p'. Then, with the assumption of a suitable mean flow, the linearized perturbation equations can be solved as a generalized eigenvalue problem.

$$\begin{bmatrix} & & \\ & A & \\ & & \end{bmatrix} \begin{bmatrix} \tilde{u}(z) \\ \tilde{v}(z) \\ \tilde{w}(z) \\ \tilde{b}(z) \\ \tilde{p}(z) \end{bmatrix} - i\sigma \begin{bmatrix} & & \\ & B & \\ & & \end{bmatrix} \begin{bmatrix} \tilde{u}(z) \\ \tilde{v}(z) \\ \tilde{w}(z) \\ \tilde{b}(z) \\ \tilde{p}(z) \end{bmatrix} = \begin{bmatrix} 0 \\ 0 \\ 0 \\ 0 \\ 0 \end{bmatrix}$$

where A is the matrix of coefficients (which need not be constant in z) for spatial derivative and constant terms, and B contains the time derivative coefficients. The column of $\tilde{(\cdot)}$ variables then serve as the eigenvector, and σ is the eigenvalue (where the imaginary part of σ is the growth rate of an unstable mode). All eigenvectors and coefficients of A and B are discretized using Chebyshev spectral modes, and the problem is solved on a Gauss-Lobatto grid (see Boyd, 2001). This allows for finer resolution near the top and bottom of the domain where viscous boundaries are enforced. This also assures that the steeply decaying Stokes drift is well resolved. The eigenvalue problem is then solved with Matlab's solver *eig.m*. The Matlab code that is used in setting up and solving this problem is in appendix B.

Several of the comparisons presented in the following sections serve as a way of validating the code and methodology for solving the equations. In some instances, equations 3.8-3.11 collapse identically back to the equation set of other relevant previous linear stability problems. In these cases, the comparison serves as verification of the numerical method of solving the equations. In other cases, the equations that are compared are not identical, and therefore, the comparisons serve to show that the dominant dynamics are still captured in the present linear stability model.

3.1.2 Energetics

A very useful tool to help distinguish between unstable modes is the kind of energy those modes extract from the mean flow. The perturbation energy equation is formed by the dot product of the momentum equation with the velocity.

$$\delta Ro\left[\overline{\frac{D^L e'}{D_t}} + \underbrace{\overline{\nabla_h\cdot\mathbf{u}'p'} + \overline{\partial_z(w'p')}}_{PW} + \underbrace{\overline{\mathbf{u}'w'}\cdot\overline{\mathbf{U}}_z}_{ESP} + \underbrace{\overline{\mathbf{u}'w'}\cdot\mathbf{U}_z^S}_{SSP} + \underbrace{\overline{w'b'}}_{BP}\right] + \underbrace{-\frac{\delta^2 Ek}{\alpha^2}\left[\overline{e'_{zz}} + \overline{(\mathbf{u}'_z)^2} + \overline{w'^2_z}\right] - Ek\left[\overline{\nabla_h^2 e'} + \overline{(\nabla_h\mathbf{u}')^2}\right]}_{diss} = 0 \tag{3.13}$$

where $\frac{D^L}{D_t} \equiv \partial_t + (\mathbf{U}^L\cdot\nabla)$, $e' \equiv \frac{1}{2}(\mathbf{u}'\cdot\mathbf{u}' + w'w')$ is the kinetic energy of the perturbed flow, PW is the pressure work, ESP is the Eulerian shear production, SSP is the Stokes shear production, BP is buoyancy production, and $diss$ is energy dissipation.

The dominant energy production terms in equation 3.13 for each unstable mode help classify the type of instability. LC get their energy from a combination of ESP and SSP. Furthermore, if a mode produces negative SSP, it cannot be LC since the SSP term is identically the work done by the Stokes shear force on the vertical part of the circulation. This is another advantage of the considering the Stokes Shear force form of the WAB equations. SI obtain their energy mostly from the ESP whereas GI obtain their energy primarily from BP (e.g. Haine and Marshall, 1998). In general, the PW term is small, and the dissipation term will not be considered. These energetic properties are used to verify the type of unstable mode

throughout this chapter and chapter 4. In this chapter, where the more pure forms of the unstable modes are examined, identification based on the vertical structure and energetics is quite straightforward. Moving away from these far corners of parameter space reveals mixed modes with mixed energetics, and the distinction is less clear.

3.2 Quasi- Geostrophic (QG) Regime

Although none of the instabilities in the mixed layer are strictly QG, as discussed in section 1.3.2 the dynamics of QG GI are very similar to those of GI in the mixed layer. Therefore it is useful to show that the present linear stability model reproduces the GI found by Eady (1949). The QG regime exists where $Ro << 1, Ri >> 1, \delta = \sqrt{Ri}Ro, Ek = 0, \alpha << Ro, \gamma = 1, \mu = 0$. Since $Ro\delta,\ Ro\alpha^2 << 1$ the nonlinear terms as well as others can be neglected. Then the mean flow must satisfy the following:

$$\nabla_H \overline{P} + \hat{\mathbf{k}} \times \overline{\mathbf{U}}^L = 0 \tag{3.14}$$

$$\mu\lambda Ro \overline{\mathbf{U}}^L \cdot \mathbf{U}_z^S + \overline{P}_z - \overline{B} = 0 \tag{3.15}$$

$$\overline{B}_T + \gamma(\overline{\mathbf{U}}^L \cdot \nabla_H)\overline{B} = 0 \tag{3.16}$$

$$\nabla_H \cdot \overline{\mathbf{U}} + \frac{1}{\delta}\overline{W}_z = 0 \tag{3.17}$$

$$\overline{W} = 0 \quad on \quad z = 0, -1. \tag{3.18}$$

Note that the Stokes shear force was retained above. This is in order to inform a discussion of Stokes modified QG baroclinic instability in chapter 4. Any mean flow that satisfies this would be strictly geostrophic, but non-hydrostatic due to the Stokes shear force. However, in this section, the Stokes shear force term is neglected (i.e. $\mu = 0$). A simple steady state solution to the above equations is the Eady background state.

$$\begin{aligned} \overline{U} &= z + 1, \quad \overline{V} = 0, \quad \overline{W} = 0, \\ \overline{B} &= -Y + z, \quad \overline{P} = -Yz + \frac{1}{2}z^2 \end{aligned} \tag{3.19}$$

With this background state, the perturbation equations are

$$\frac{Ro}{\delta}\left[\mathbf{u}'_t + (\overline{\mathbf{U}}^L \cdot \nabla_h)\mathbf{u}' + w'\ \overline{\mathbf{U}}_z\right] + \nabla_h p' + \hat{\mathbf{k}} \times \mathbf{u}' = 0 \tag{3.20}$$

$$\frac{\mu\lambda Ro}{\delta}\mathbf{u}' \cdot \mathbf{U}^S_z + [p'_z - b'] = 0 \tag{3.21}$$

$$\sqrt{Ri}\ Ro\ \left[b'_t + (\overline{\mathbf{U}}^L \cdot \nabla_h)b'\right] + \sqrt{Ri}\ Ro\ (\mathbf{u}' \cdot \nabla_H)\overline{B} + Ri\ Ro\ w'\overline{B}_z = 0 \tag{3.22}$$

$$\nabla_h \cdot \mathbf{u}' + w'_z = 0 \tag{3.23}$$

$$w' = 0 \quad on \quad z = 0, -1. \tag{3.24}$$

Note that δ has been replaced with $\sqrt{Ri}Ro$. This highlights the fact that this regime is baroclinically unstable since $\left[Ri\left(\frac{Ro}{\delta}\right)^2\right]^{-1} = 1$, and the fact that $Ri >> 1$ and $\frac{Ro}{\delta} << 1$ implies that this is the QG regime. Here, the perturbation equations collapse identically back to the QGPV equations solved by Eady (see e.g. Pedlosky (1982) to convert from velocity to PV in the QG limit).

The following figures show that the Eady problem can be reproduced as in Vallis (2006).

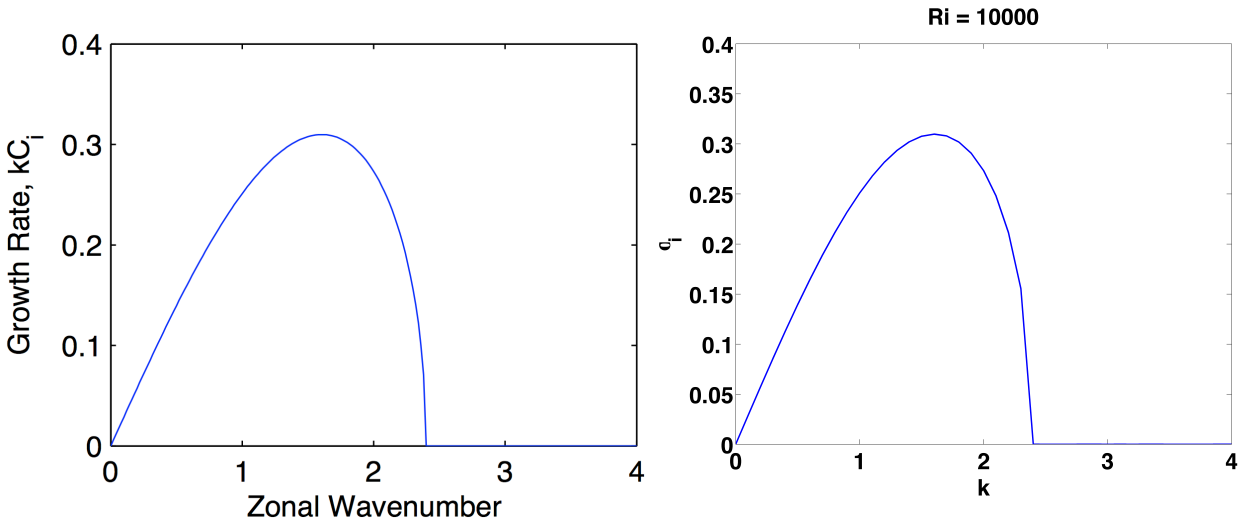

Figure 3.1: The fastest growing mode is plotted as a function of along front (zonal, 'k') wavenumber. Mixed cross-along front wavenumber perturbations (not shown) are also unstable, but less so. (left) Figure 6.10a from Vallis (2006). (right) Reproduced with equations 3.20-3.24.

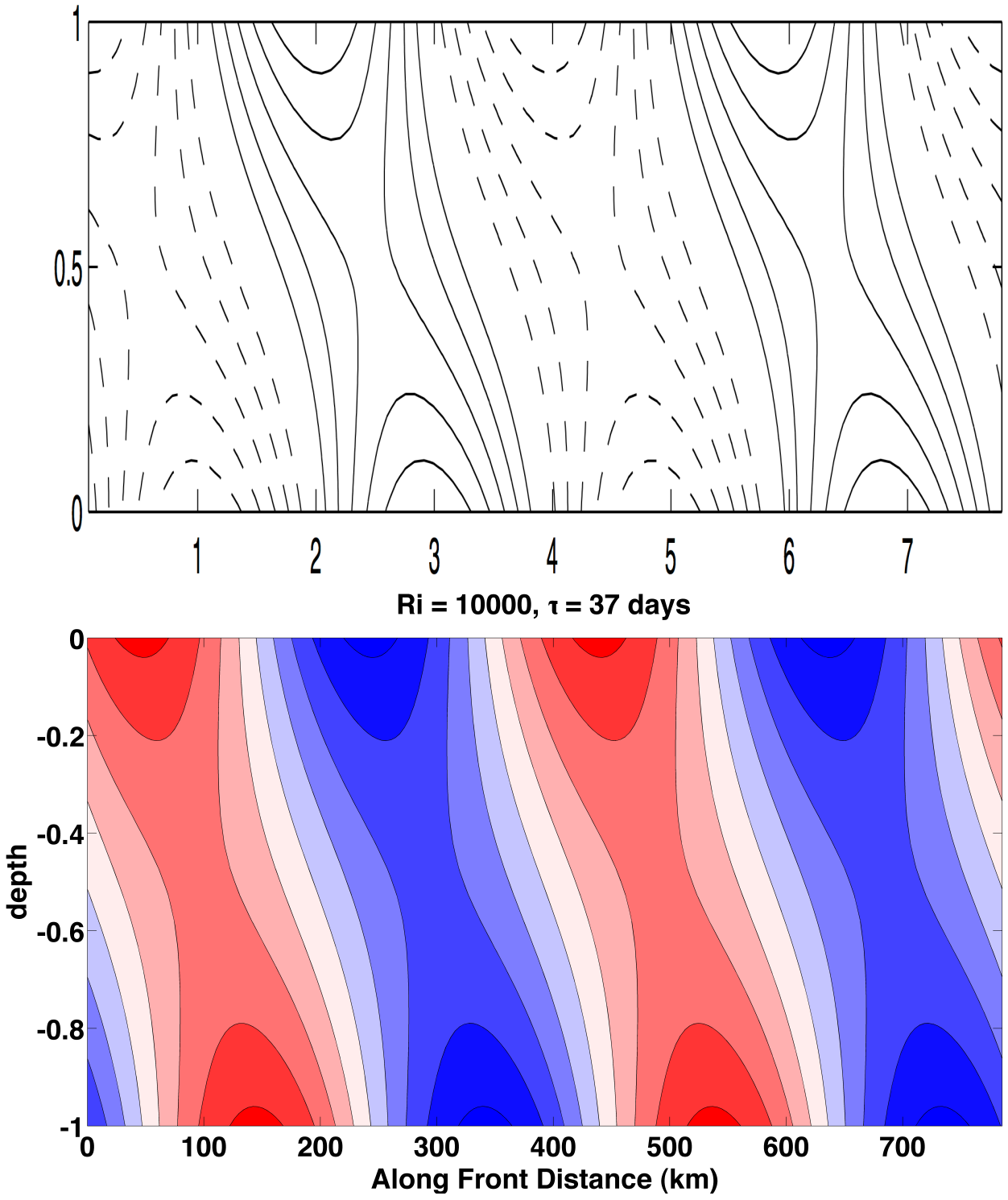

Figure 3.2: (top) Cross front velocity panel of Figure 6.12 from Vallis (2006). (bottom) Reproduced with equations 3.20-3.24.

As discussed in the introduction (chapter 1), GI in the QG regime is very similar to GI in the mixed layer. As Boccaletti et al. (2007) frame it, in both cases $RiRo^2 \sim 1$, so that the scale of the instability is on the scale of the Rossby radius of deformation ($L_d = \frac{NH}{f}$). The differences between QG GI and mixed layer GI are in the scale of L_d and the size of the dimensionless parameters. Nevertheless, the instabilities presented above give the best QG approximation to MLEs.

3.3 Submesoscale Flows

Stone (1971) explored the ageostrophic, non-hydrostatic instabilities which may occur in a geostrophically balanced front. The front is an inviscid, Eady-like mean flow , $Ro << 1, \delta = Ro, Ek = 0, \alpha \lesssim \sqrt{Ro}, \gamma = 1, \mu = 0$. Since $Ro\delta,\ Ro\alpha^2 << 1$ the nonlinear terms as well as others can be neglected. This yields the following set of equations averaged over the small (x, y, t) scales, and retaining $O(1)$ and larger terms.

$$\overline{W}\ \overline{\mathbf{U}}_z + \nabla_H P + \hat{\mathbf{k}} \times \overline{\mathbf{U}} = 0 \tag{3.25}$$

$$\mu\lambda Ro \overline{\mathbf{U}}^L \cdot \mathbf{U}_z^S + \overline{P}_z - \overline{B} = 0 \tag{3.26}$$

$$\overline{B}_T + \gamma(\overline{\mathbf{U}} \cdot \nabla_H)\overline{B} + Ri\overline{W}\ \overline{B}_z = 0 \tag{3.27}$$

$$\nabla_H \cdot \overline{\mathbf{U}} + \frac{1}{\delta}\overline{W}_z = 0 \tag{3.28}$$

One steady state solution to the above equations is the Eady-like background state.

$$\begin{aligned} \overline{U} &= z + 1, \quad \overline{V} = 0, \quad \overline{W} = 0, \\ \overline{B} &= -Y + z, \quad \overline{P} = -Yz + \frac{1}{2}z^2 \end{aligned} \tag{3.29}$$

Again the Stokes shear force term is retained to inform a discussion of wave forced ageostrophic baroclinic instability in chapter 4. This term will be neglected for the remainder of this sec-

tion. Then the perturbation equations are

$$\mathbf{u}'_t + (\overline{\mathbf{U}} \cdot \nabla_h)\mathbf{u}' + w' \, \overline{\mathbf{U}}_z + \hat{\mathbf{k}} \times \mathbf{u}' + \nabla_h p' = 0, \tag{3.30}$$

$$\left(\frac{\alpha}{Ro}\right)^2 \left[w'_t + (\overline{\mathbf{U}} \cdot \nabla_h)w'\right] + p'_z - b' = 0, \tag{3.31}$$

$$b'_t + (\overline{\mathbf{U}} \cdot \nabla_h)b' + (\mathbf{u}' \cdot \nabla_H)\overline{B} + Riw'\overline{B}_z = 0, \tag{3.32}$$

$$\nabla_h \cdot \mathbf{u}' + w'_z = 0, \tag{3.33}$$

$$w' = 0 \quad on \quad z = 0, -1. \tag{3.34}$$

Equations 3.30-3.34 are equivalent to equations 2.7-2.12 of Stone (1971). Although they do not look identical, they are equivalent. Merely replacing the buoyancy scaling with N^2H, and scaling all pressure gradient terms as such would yield the identical equations. Also note that here, $\frac{\alpha}{Ro}$ is equivalent to Stone's δ, and since the only mean shear is geostrophic, Ri here is as in Stone (1971). Therefore, this section serves as a verification of the numerical method of solving equations 3.30-3.34.

As expected, since the equations are equivalent, the non-hydrostatic effects on GI (figure 3.3) and SI (figure 3.4) are reproduced as in Stone (1971). The shapes of the curves are slightly different here. This is due to the fact that figure 1 of Stone shows an approximation to an analytic expression, whereby higher orders of the complex wave speed $c(k)$ are neglected (see equations 3.4, 3.11, and 3.12 of Stone (1971)). Furthermore, when compared to the analytic approximations for GI in Stone (1970) (his figure 10) the numerical solutions show the same asymmetric shape where growth rate falls steeply as the high wavenumber cutoff is approached.

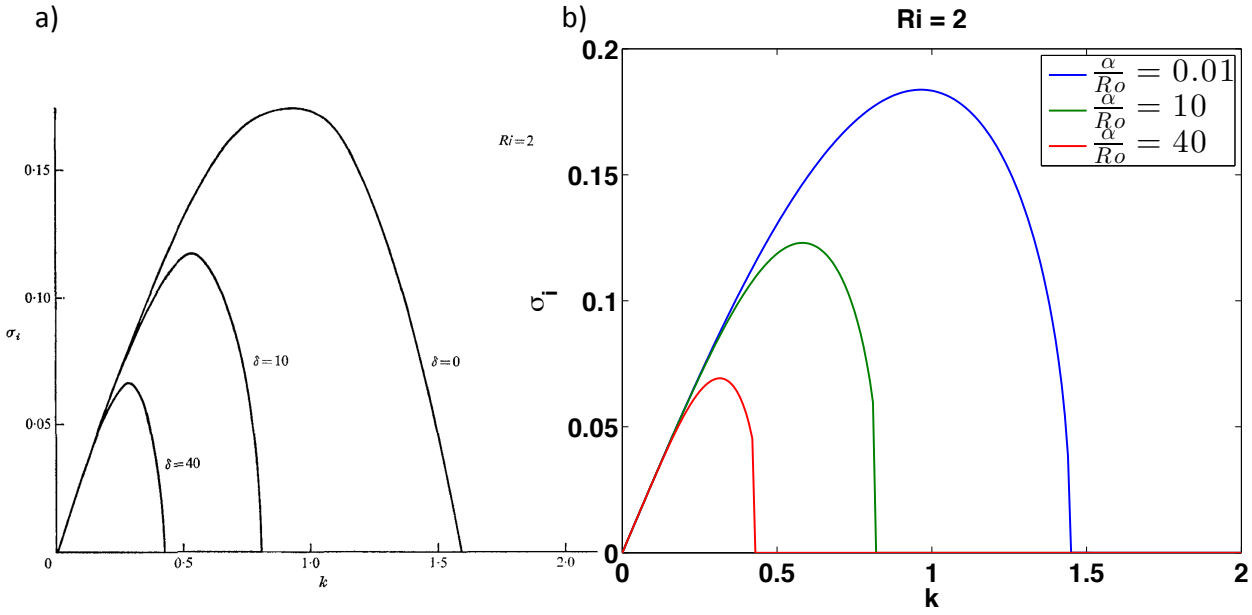

Figure 3.3: Growth rate as a function of along front wavenumber, k, for a mean flow with $Ri = 2$. The growth rate and wavenumber decrease as the perturbations become less hydrostatic. a) Figure 1 from Stone (1971). b) Reproduced with equations 3.30-3.33.

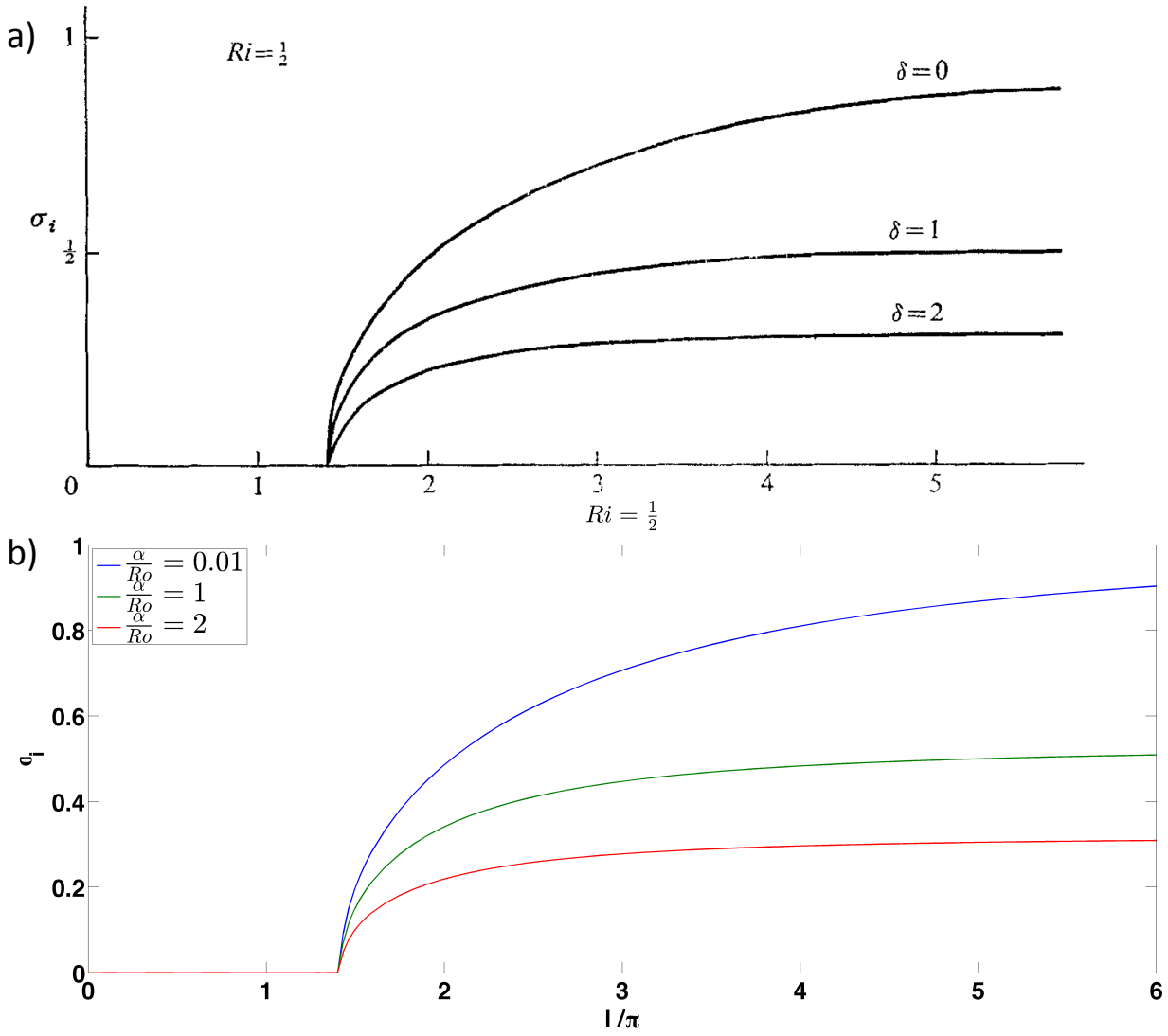

Figure 3.4: Growth rate, σ_i vs the normalized cross front wavenumber, l/π, for a symmetrically unstable flow ($Ri = 0.5$). The growth rate is significantly reduced with only $O(1)$ perturbations to hydrostasis. a) Figure 2 from Stone (1971). b) Reproduced with equations 3.30-3.33.

The most notable result of these figures is that perturbations from hydrostatic balance affect SI when $\delta \equiv \frac{\alpha}{Ro} \sim O(1)$, whereas, the growth rate of GI is not affected until $\delta \equiv \frac{\alpha}{Ro} \sim O(10)$. This is unsurprising when considering the along isopycnal motions of SI (Haine and Marshall, 1998). SI are generally active when isopycnals are steep, therefore, they have appreciable vertical velocities. When the $\delta \sim O(1)$, the vertical velocity terms can then strongly perturb hydrostatic balance. Based on parcel switching arguments, GI extract the most potential energy when they travel along a slope half as steep as the isopycnals, therefore implying weaker vertical velocities, and a smaller perturbation to hydrostatic balance.

Lastly, since the perturbation equations are equivalent, all results from Stone (1970, 1971) can be reproduced with with equations 3.30-3.33, however, it is assumed that the results above are sufficient for validation of the numerical method.

3.4 The LC Regime

Leibovich and Paolucci (1981) studied the viscid, vertically stratified, non-rotating mixed layer forced by Stokes drift and a surface wind stress. These results cannot be identically matched with the present linear stability model because their bottom boundary condition is applied at $z \to -\infty$. Nevertheless, qualitative similarities are attainable. Furthermore, the full extent of their analysis involves a time evolving Eulerian shear profile which becomes constant as $t \to \infty$. It is only in this long time limit in which the results may be compared to the steady mean flow implemented in the present model. Therefore, both the numerical implementation, and the presence of the same dominant features of the dynamics are vetted in this section where the present model configuration differs from that of Leibovich and Paolucci (1981). To reduce equations 3.8-3.11 to equations for the relevant regime, down wave/wind invariance is assumed, as well as $\gamma = 0, Ro >> 1, \delta = \frac{1}{Ro}, \alpha = \delta, \mu\lambda \sim O(1), Ek \sim \delta Ro$ (i.e. $Ek \lesssim 1$), and retaining $O(1)$ and

larger terms.

$$\overline{\mathbf{U}}_T + (\overline{\mathbf{U}}^L \cdot \nabla_H)\overline{\mathbf{U}} + \frac{1}{Ro}\overline{W}\ \overline{\mathbf{U}}_z + \nabla_H P - \frac{Ek}{Ro^3}\overline{\mathbf{U}}_{zz} = 0 \tag{3.35}$$

$$\overline{W}\ \overline{W}_z + \mu\lambda\overline{\mathbf{U}}^L \cdot \mathbf{U}_z^S + \overline{P}_z - \overline{B} = 0 \tag{3.36}$$

$$\overline{B}_T + \frac{Ri}{Ro}\overline{W}\ \overline{B}_z - \frac{Ek}{Ro^3 Pr}\overline{B}_{zz} = 0 \tag{3.37}$$

$$\nabla_H \cdot \overline{\mathbf{U}} + \frac{1}{\delta}\overline{W}_z = 0 \tag{3.38}$$

One steady state solution which satisfies the above is

$$\overline{\mathbf{U}} = z + 1, \quad \overline{W} = 0 \tag{3.39}$$

$$\overline{B} = z, \quad \overline{P} = \frac{1}{2}z^2, \tag{3.40}$$

Since the mean Stokes shear force term ($\mu\lambda\overline{\mathbf{U}}^L \cdot \mathbf{U}_z^S$) is horizontally invariant, it can be absorbed into the pressure gradient term (see chapter 1 and Suzuki and Fox-Kemper (2015)). With this mean flow, the perturbation equations are:

$$\mathbf{u}'_t + w'\ \overline{\mathbf{U}}_z + \nabla_h p' - \frac{Ek}{Ro^2}\left[\mathbf{u}'_{zz} - \nabla_h^2\mathbf{u}'\right] = 0 \tag{3.41}$$

$$w'_t + \mu\lambda\mathbf{u}' \cdot \mathbf{U}_z^S + p'_z - b' - \frac{Ek}{Ro^2}\left[w'_{zz} - \nabla_h^2 w'\right] = 0 \tag{3.42}$$

$$b'_t + Riw'\overline{B}_z - \frac{Ek}{Ro^2 Pr}\left[b'_{zz} - \nabla_h^2 b'\right] = 0 \tag{3.43}$$

$$\nabla_h \cdot \mathbf{u}' + w'_z = 0 \tag{3.44}$$

$$w' = 0, \quad and, \quad \mathbf{u}'_z, b'_z = 0 \quad on \quad z = 0, -1,$$

$$w'_{zz} = 0 \quad on \quad z = -1, \tag{3.45}$$

These equations are analogous to equations 29a-c in Leibovich and Paolucci (1981). To make the comparison, the following translation of parameters is necessary.

$$La^{LP} = \frac{\nu k_w^2}{u_*}\frac{(\sigma\nu)^{\frac{1}{2}}}{\epsilon\sigma} = \frac{\lambda^{\frac{3}{2}}Ek}{2Ro\ \alpha\ \mu^{\frac{1}{2}}\hat{\tau}^{\frac{1}{2}}} \tag{3.46}$$

$$Ri^{LP} = \frac{\beta g\overline{T}'(z)}{(a_w u_* k_w)^2(\sigma_w/\nu)} = \frac{4Ri}{\mu\lambda\hat{\tau}}, \tag{3.47}$$

$$l^{LP} = \hat{l}k_w^{-1} = l\frac{2\alpha}{\lambda\delta}, \tag{3.48}$$

where $(\cdot)^{LP}$ indicates a dimensionless parameter from Leibovich and Paolucci (1981), a_w, k_w, and σ_w are the amplitude, wavenumber, and frequency of the waves respectively. $\hat{l}$ indicates a dimensional horizontal length scale.

Leibovich and Paolucci (1981) showed that the mixed layer is stable to LC regardless of wavenumber (i.e. globally stable) when $La \gtrsim 1$, and that for smaller values of La, LC are more unstable at lower wavenumbers. Results were obtained for $Ri^{LP} = 0, 0.1, 0.25$, however only the $Ri^{LP} = 0.1$ case will be shown here as they are all qualitatively and quantitatively similar. Figure 3.5 shows this result, and a qualitative comparison is made with the present linear stability model (figure 3.6).

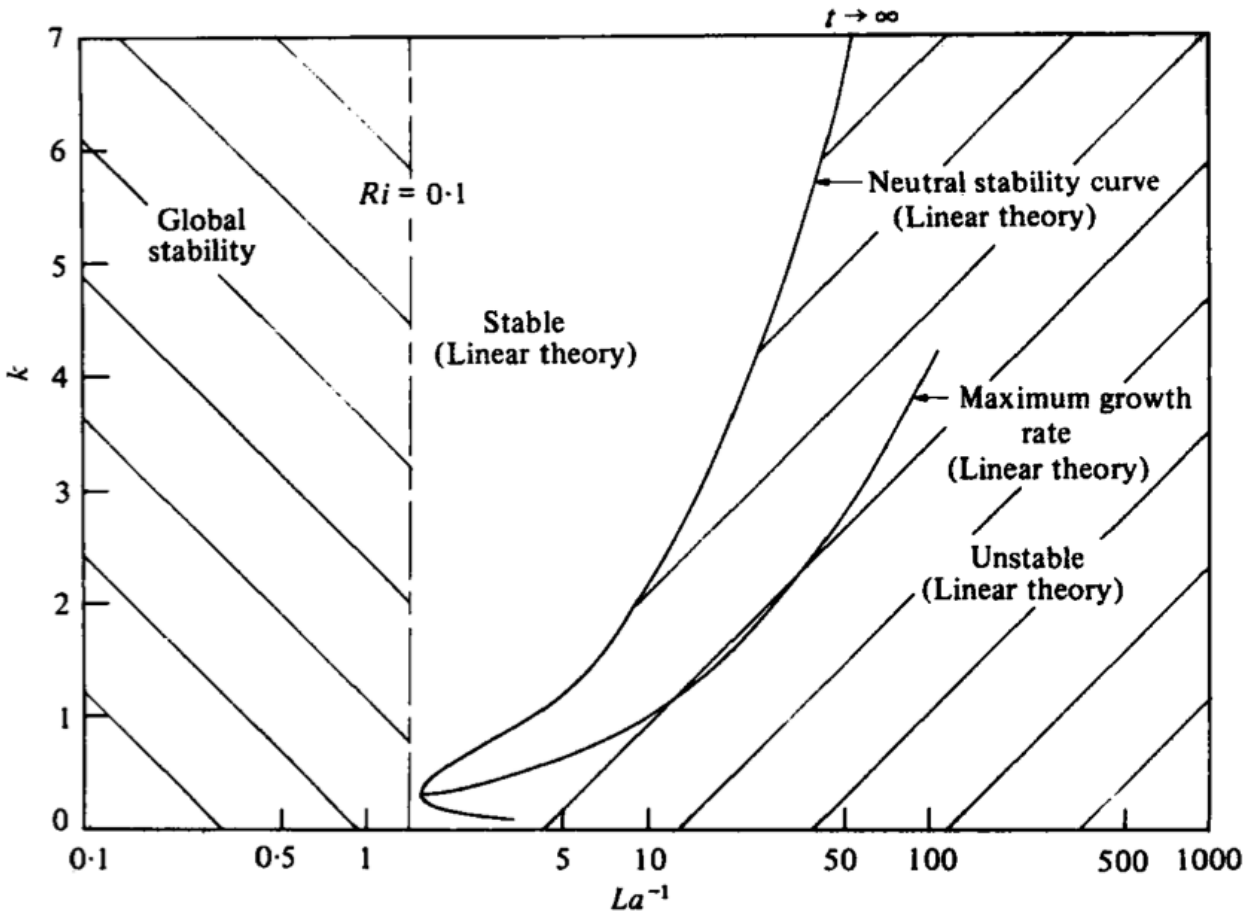

Figure 3.5: Figure 7 from Leibovich and Paolucci (1981). Stability boundaries for LC are shown.

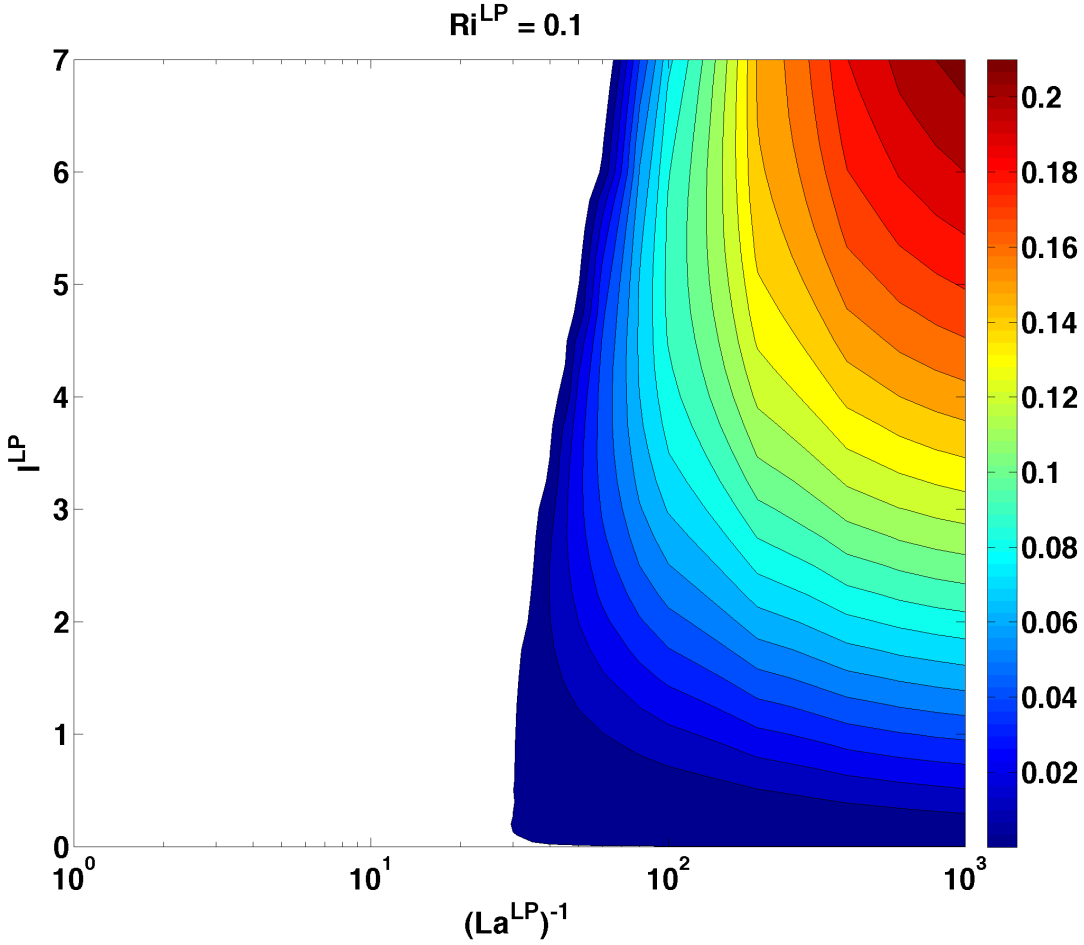

Figure 3.6: Figure 7 from Leibovich and Paolucci (1981) reproduced with equations 3.41-3.44. Growth rates for LC are contoured.

As mentioned above, the present model is not expected to achieve identical results because of the finite depth domain used here, unlike the infinite depth domain in Leibovich and Paolucci (1981). Nevertheless, the supercritical region is qualitatively similar, and the stability boundary for high wavenumbers is similar. This implies that the dominant dynamics of LC are captured in the present linear stability model despite quantitative differences from that of Leibovich and Paolucci (1981).

3.5 The Stokes-Ekman Layer

Gnanadesikan and Weller (1995) studied the effects of Stokes drift on the mean Ekman flow, and the instabilities that develop from it. The Stokes drift alters the Ekman flow by creating a partially opposing Eulerian flow. This anti-Stokes Eulerian flow must exist in order to maintain the same Lagrangian transport of the flow in the absence of Stokes drift. This arises because the Stokes Coriolis force alters the usual Ekman balance, thus requiring a change in the Eulerian flow. The Stokes Coriolis force also plays this role in geostrophically balanced fronts (McWilliams and Fox-Kemper, 2013). The Stokes-Ekman layer lies in the parameters space where $Ro << 1, \delta \sim o(Ro), Ek \sim o(Ro), \alpha = \delta, \gamma = 0, Ri = 0$. A steady mean flow must then solve

$$\nabla_H \overline{P} + \hat{\mathbf{k}} \times \overline{\mathbf{U}}^L - Ek \nabla_H^2 \overline{\mathbf{U}} - \frac{Ek}{\alpha^2} \overline{\mathbf{U}}_{zz} = 0 \tag{3.49}$$

$$\mu\lambda \overline{\mathbf{U}}^L \cdot \mathbf{U}_z^S + \overline{P}_z - \frac{Ek}{Ro\delta} \overline{W}_{zz} = 0 \tag{3.50}$$

$$\nabla_H \cdot \overline{\mathbf{U}} + \frac{1}{\delta} \overline{W}_z = 0 \tag{3.51}$$

A steady state solution to the above equations is as follows:

$$\begin{aligned} \overline{U} + i\overline{V} &= \frac{1}{(1+i)\eta} \left[\hat{\tau} e^{i\theta^\tau} - \frac{2i\lambda\mu e^{i\theta}}{(\frac{\lambda}{\eta})^2 - 2i} \right] e^{(1+i)\eta z} + \frac{2i\mu e^{i\theta}}{(\frac{\lambda}{\eta})^2 - 2i} e^{\lambda z}, \\ \overline{W} &= 0, \qquad \overline{P}(z) = \int \mu\lambda \overline{\mathbf{U}}^L \cdot \mathbf{U}_z^S dz, \end{aligned} \tag{3.52}$$

where $\eta \equiv \frac{H}{H^{Ekman}} = \frac{\alpha}{\sqrt{2Ek}}$ is the normalized inverse Ekman depth, $\hat{\tau} \equiv \frac{\tau}{\rho\nu \overline{U}_z^L}$ is the normalized surface wind stress magnitude, and θ^τ is the wind direction. The Ekman-Stokes solution for $\overline{U} + i\overline{V}$ is derived with Pierson-Moskowitz Stokes drift in Gnanadesikan and Weller (1995), monochromatic Stokes drift (one for swell and one for wind waves) in McWilliams et al. (2014), and including a geostrophically balanced front with an external buoyancy source (as in 3.52) in appendix C.

Gnanadesikan and Weller (1995) use the wavenumber of the peak of the Pierson-Moskowitz spectrum which is analogous to the length scale used for monochromatic waves

in Leibovich and Paolucci (1981). Matching this with the e-folding depth of monochromatic Stokes drift gives an underestimate of the Stokes shear since the Pierson-Moskowitz spectrum decays faster than exponential with depth. Nevertheless, I proceed with qualitative comparisons. The underestimate of Stokes shear will mean weaker instabilities for all cases, and LC that are rotated further to the right than if the Stokes shear was stronger. The latter effect is because, as discovered in Gnanadesikan and Weller (1995), LC align with the Lagrangian shear, which is further rightward when the Stokes shear is weaker.

Given the mean flow above, the perturbation equations are

$$\frac{Ro}{\delta}\left[\mathbf{u}'_t + (\overline{\mathbf{U}}^L \cdot \nabla_h)\mathbf{u}' + w'\ \overline{\mathbf{U}}_z + \nabla_h p'\right] + \hat{\mathbf{k}} \times \mathbf{u}' - \frac{Ek}{\delta^2}\left[\mathbf{u}'_{zz} + \nabla_h^2 \mathbf{u}'\right] = 0 \qquad (3.53)$$

$$w'_t + (\overline{\mathbf{U}}^L \cdot \nabla_h)w' + \mu\lambda \mathbf{u}' \cdot \overline{\mathbf{U}}^S_z + p'_z - \frac{Ek}{Ro\delta}\left[w'_{zz} + \nabla_h^2 w'\right] = 0 \qquad (3.54)$$

$$\nabla_h \cdot \mathbf{u}' + w'_z = 0 \qquad (3.55)$$

$$w' = 0, \quad \textit{and,} \quad \mathbf{u}'_z = 0 \quad \textit{at} \quad z = 0, -1,$$

$$w'_{zz} = 0 \quad \textit{at} \quad z = 0, \qquad (3.56)$$

The dimensionless parameters in Gnanadesikan and Weller (1995) relate to those in the present work as follows:

$$La = \frac{\nu}{a_w^2 \sigma} = \frac{Ek\lambda}{2Ro\mu\alpha}, \qquad F = \frac{f}{a_w^2 k_w^2 \sigma} = \frac{2\alpha}{\mu\lambda Ro} \qquad (3.57)$$

Gnanadesikan and Weller (1995) show how the growth and direction of LC changes as these two parameters change (figure 3.7). As we learned from Leibovich and Paolucci (1981) in the previous section, LC become more unstable with decreasing La, and the stability boundary lies near $La \sim 1$. Gnanadesikan and Weller (1995) have a different definition for La, and the aforementioned differences due to stronger Stokes shear, but their results are fairly consistent. As F increases, the effect of the Coriolis force becomes stronger relative to Stokes shear, rotating the Eulerian shear, and therefore the LC, to the right. All of these results are qualitatively reproduced by equations 3.53-3.56 in figure 3.8 with the caveats discussed above. The parameter spaces of the two figures correspond exactly (the reader

may verify through 3.57), however the non-dimensional parameters of the present model are displayed in figure 3.8. Instead of La, I choose to show the relative strength of the Stokes shear force compared to the viscous forces in the vertical velocity equation (see equation 3.54). Instead of F I choose to show the strength of the advective terms compared to the Coriolis force (see equation 3.53).

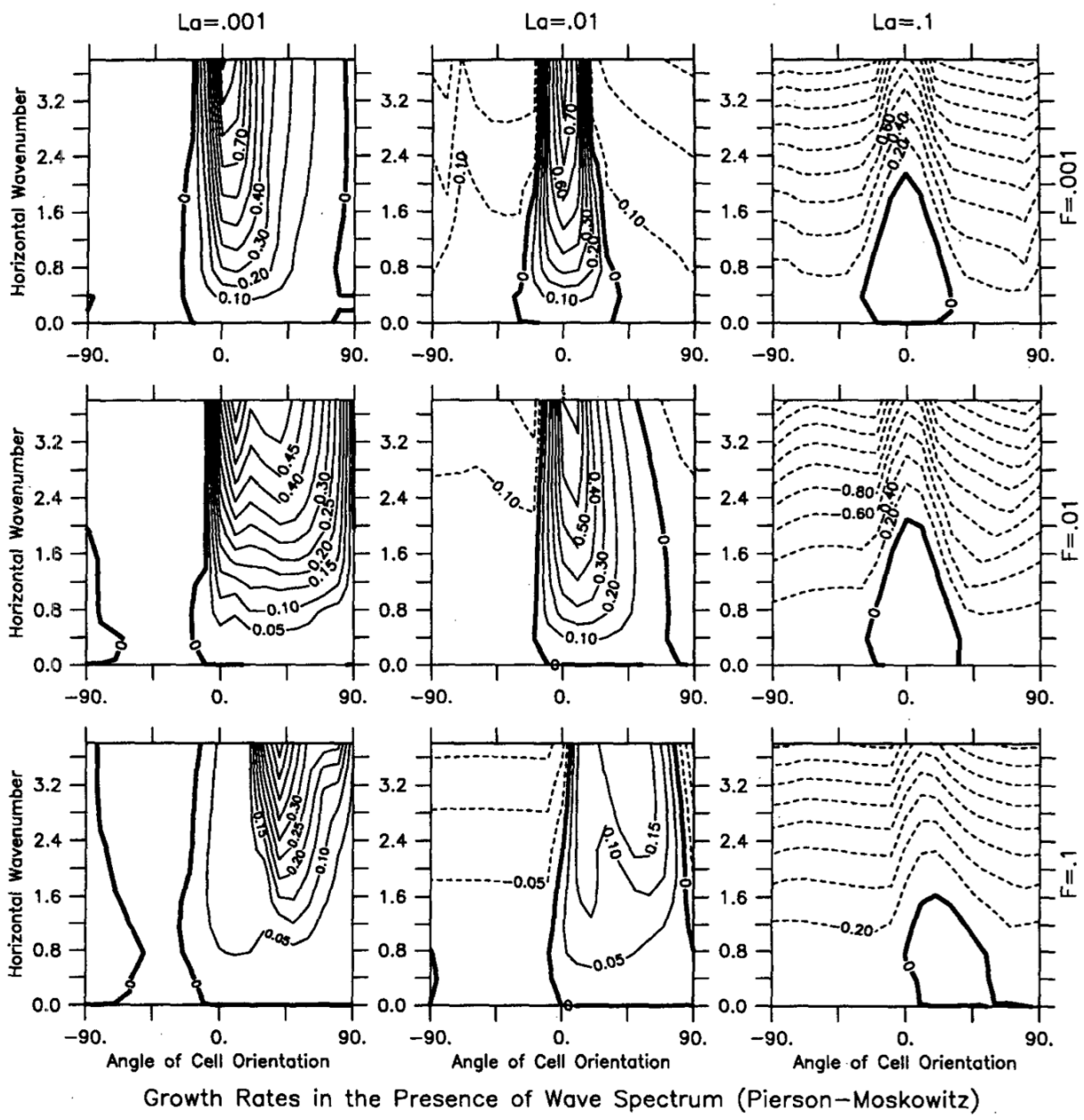

Figure 3.7: Figure 7 from Gnanadesikan and Weller (1995). Growth rates for LC are contoured. Dashed contours indicate negative growth (decaying modes). The thick black contour indicates neutral stability. An angle of zero degrees for cell orientation implies that the vorticity axis of LC is aligned with the Stokes drift.

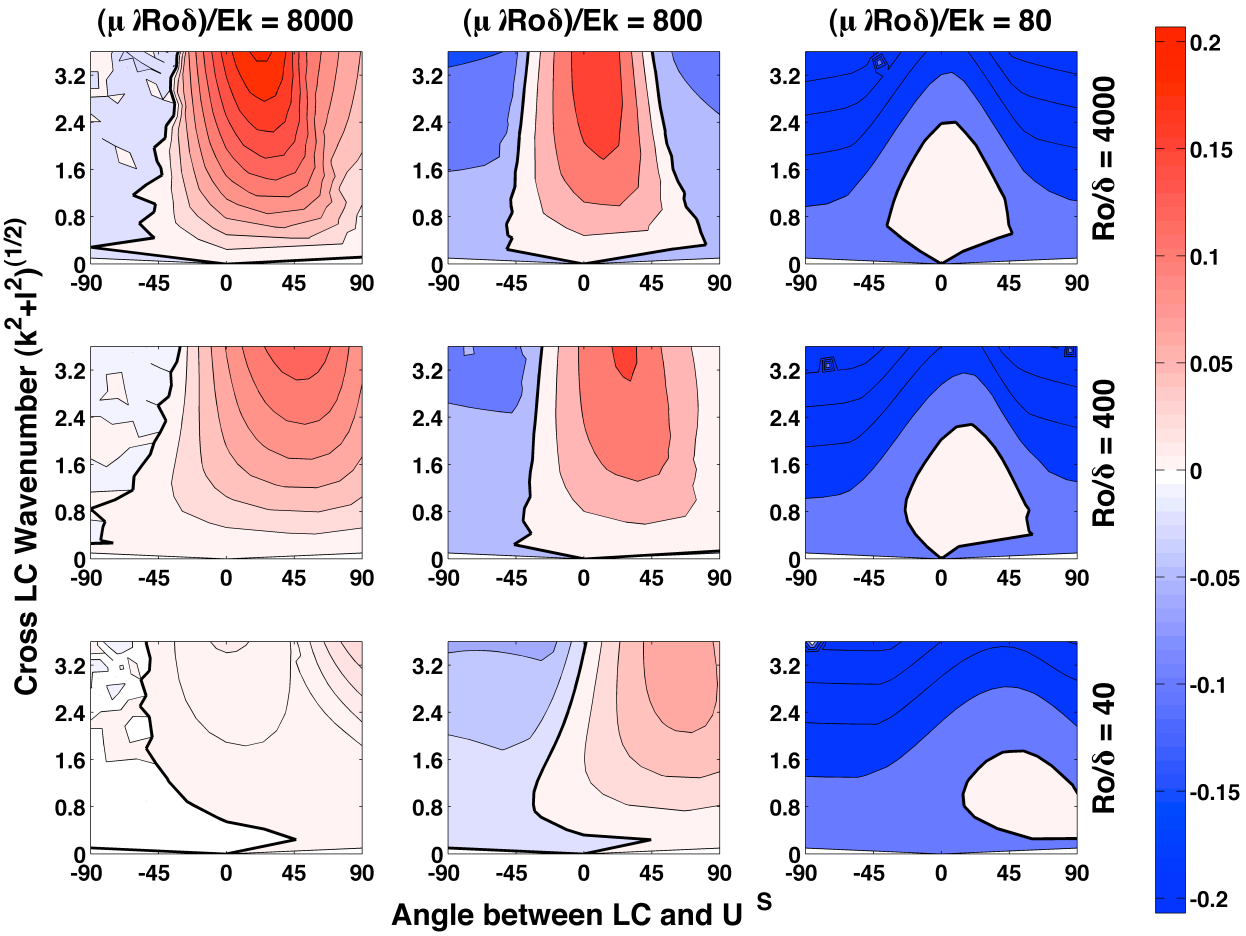

Figure 3.8: Figure 7 from Gnanadesikan and Weller (1995) reproduced with equations 3.53-3.56. Red indicates growing modes, and blue indicates decaying modes. The thick black contour indicates neutral stability. Note that the dimensionless parameters correspond to those in figure 3.7, however the dimensionless parameters for the present model are displayed here.

The strong qualitative similarities imply that the dominant dynamics of LC in an Ekman layer are captured in the present model, and that the numerical implementation is working well. The quantitative differences are well explained by differences in the Stokes profiles between the two models (Pierson-Moskowitz vs monochromatic), which results in differences in Stokes shear. The different Stokes shears allow for predictably different behavior in the strength and dominant direction of LC.

3.6 Hybrid LC/SI Modes

As mentioned in chapter 1, Li et al. (2012) explored the interaction between fronts and LC through linear stability analysis. They found what they call a hybrid LC/SI mode that exists for $Ri^E > 1$, where they suggest that SI should not exist. However, not unlike FSI (discussed in section 1.3.3), Stokes drift, as with any ageostrophic shear, breaks the direct relation between Ri^E and PV. This implies that $Ri^E > 1$ does not indicate that SI cannot exist.

The results of this paper can be identically reproduced since their equations $10-13$ are a subset of equations 3.8-3.11. This section will demonstrate this equivalence by reproducing figures 3-5 in Li et al. (2012). First assume, $Ro << 1, \delta \sim o(Ro), Ek \sim o(Ro), \alpha = \delta, \gamma = 1$. Also assume a linear Stokes drift profile in the along front direction, $\mathbf{U}^S = \mu(1+z)\hat{\mathbf{i}}$. Lastly assume no variability in the along front direction. This allows for a mean flow that satisfies

$$\nabla_H \overline{P} + \hat{\mathbf{k}} \times \overline{\mathbf{U}}^L - Ek\nabla_H^2 \overline{\mathbf{U}} - \frac{Ek}{\alpha^2}\overline{\mathbf{U}}_{zz} = 0 \tag{3.58}$$

$$\mu\lambda \overline{\mathbf{U}}^L \cdot \mathbf{U}_z^S + \overline{P}_z - \frac{Ek}{Ro\delta}\overline{W}_{zz} = 0 \tag{3.59}$$

$$\overline{B}_T + (\overline{\mathbf{U}} \cdot \nabla_H)\overline{B} + Ri\overline{W}\ \overline{B}_z = 0 \tag{3.60}$$

$$\nabla_H \cdot \overline{\mathbf{U}} + \frac{1}{\delta}\overline{W}_z = 0 \tag{3.61}$$

$$\overline{W} = \overline{B}_z = 0, \quad \overline{\mathbf{U}}_z = 1-\mu \quad on \quad z = 0, -1,$$

$$and \quad \overline{W}_{zz} = 0 \quad on \quad z = 0$$

A simple solution is given by

$$\overline{U} = (1-\mu)(1+z), \qquad \overline{V} = \overline{W} = 0, \tag{3.62}$$

$$\overline{B} = Y + z, \qquad \overline{P} = Yz + \frac{1}{2}z^2. \tag{3.63}$$

Although this background state solves the viscid equations, unlike the Ekman flow, the surface boundary condition is given such that the wind stress exactly matches the stress induced by the Eulerian part of the geostrophic shear. Therefore, no Ekman layer develops, and the flow is steady. Despite the lack of realism in this assumption, it allows for a horizontal buoyancy gradient to coexist with a viscous, rotating, shear flow. Without the perfectly matched wind stress, the Ekman flow would drive a net cross isopycnal Ekman transport, tipping the front over, creating an unsteady flow. This mean flow is then perturbed as follows:

$$\frac{Ro}{\delta}\left[\mathbf{u}'_t + w'\,\overline{\mathbf{U}}_z + \nabla_h p'\right] + \hat{\mathbf{k}}\times\mathbf{u}' - \frac{Ek}{\delta^2}\left[\mathbf{u}'_{zz} + \nabla_h^2\mathbf{u}'\right] = 0 \tag{3.64}$$

$$w'_t + \mu\mathbf{u}'\cdot\overline{\mathbf{U}}^S_z + p'_z - b' - \frac{Ek}{Ro\delta}\left[w'_{zz} + \nabla_h^2 w'\right] = 0 \tag{3.65}$$

$$b'_t + \frac{\delta}{Ro}(\mathbf{u}'\cdot\nabla_H)\overline{B} + Riw'\overline{B}_z - \frac{Ek}{RoPr\delta}\left[b'_{zz} + \nabla_h^2 b'\right] = 0 \tag{3.66}$$

$$\nabla_h\cdot\mathbf{u}' + w'_z = 0 \tag{3.67}$$

$$w' = 0, \quad \textit{and,} \quad \mathbf{u}'_z = 0 \quad \textit{at} \quad z = 0, -1,$$

$$w'_{zz} = 0 \quad \textit{at} \quad z = 0, \tag{3.68}$$

Equations 3.64-3.67 are equivalent to equations 10-13 in Li et al. (2012). This equivalence is easily obtained with minimal algebra, and the follow translation of parameters:

$$\begin{aligned} S &= \frac{U^S}{U^E} = \frac{\mu}{1-\mu}, \qquad Ri_v = \frac{N^2H^2}{U^{E,2}} = \frac{Ri}{(1-\mu)^2}, \qquad Ri_h = \frac{M^2H^2}{U^{E,2}} = \frac{\gamma\alpha}{Ro(1-\mu)^2} \\ La &= \frac{\nu}{U^E H} = \frac{Ek}{(1-\mu)Ro\alpha}, \qquad Pe' = \frac{U^E H}{\kappa} = \frac{Pr(1-\mu)Ro\alpha}{Ek} \end{aligned} \tag{3.69}$$

Lastly, to adequately compare the results, one must rescale the growth rate.

$$\sigma' = \hat{\sigma}\frac{H}{U_e},\ \sigma = \hat{\sigma}\frac{l}{U^L} \rightarrow \sigma = \sigma'(1-\mu) \tag{3.70}$$

where $\hat{\sigma}$ is the dimensional growth rate, and the σ' is the dimensionless growth rate in Li et al. (2012).

Figures 3.9-3.11 show that the linear stability results of Li et al. (2012) are identically reproduced. The only notable difference is a phase shift in the vertical structure functions, however, this phase is arbitrary, and not constrained by the dynamics.

The identical reproduction of the results of Li et al. (2012) in this section and the reproduction of other mixed layer linear instability results of previous sections demonstrates the strength and versatility of the present linear stability model. All of the previous linear stability models that are compared to in this chapter are confined to a narrow place in parameter space in which the flow is either rapidly rotating ($Ro << 1$) or slowly rotating ($Ro >> 1$), viscid ($Ek > 0$) or inviscid ($Ek = 0$), with the absence ($\gamma = 0$) or presence of fronts ($\gamma = 1$), and with ($\mu \sim 1$) or without ($\mu = 0$) Stokes drift. In reality, the mixed layer resides somewhere in the middle of these places in parameter space. The present linear stability model is capable of reproducing these extreme cases, and can smoothly transition to a more realistic setting. Linear instability of the ocean mixed layer with these more realistic parameters will be examined in the the next chapter.

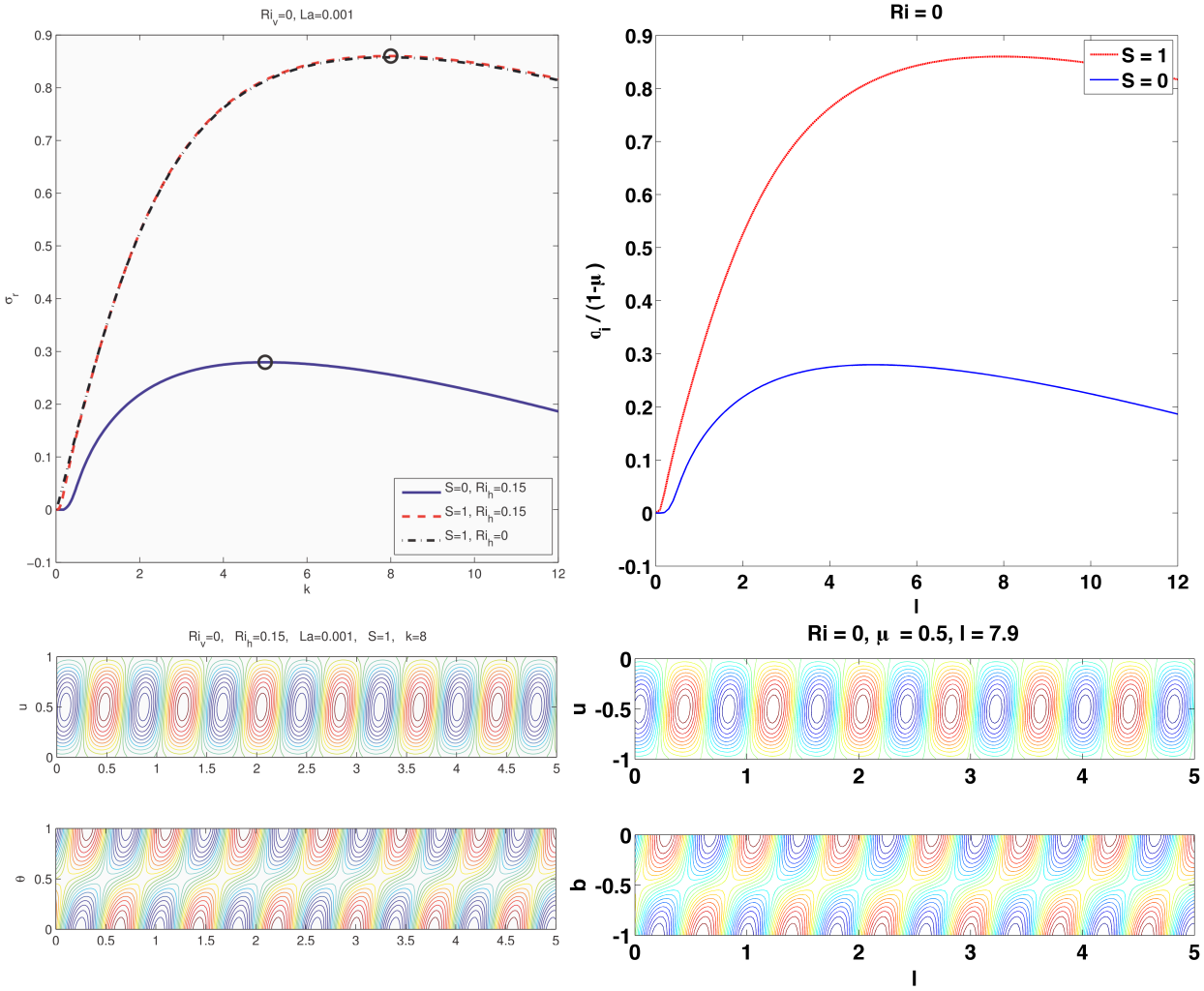

Figure 3.9: Figure 3 (left) from Li et al. (2012) and (right) reproduced with equations 3.64-3.67. Upper panels: Growth rates for LC or hybrid LC/SI mode (red) and SI (blue) as a function of the wavenumber along the horizontal buoyancy gradient. Lower panels: vertical structure for u' and b' for the fastest growing modes with $S = 1$. $Ri_v = 0, La = 0.001, Pe = 4000, Ri_h = 0.15$. Note that the parameter regime is identical in (right) and (left), but the parameters for the present model are displayed (right). The reader may verify this equivalence with equations 3.69. The growth rate has been rescaled as in equation 3.70 for convenient comparison.

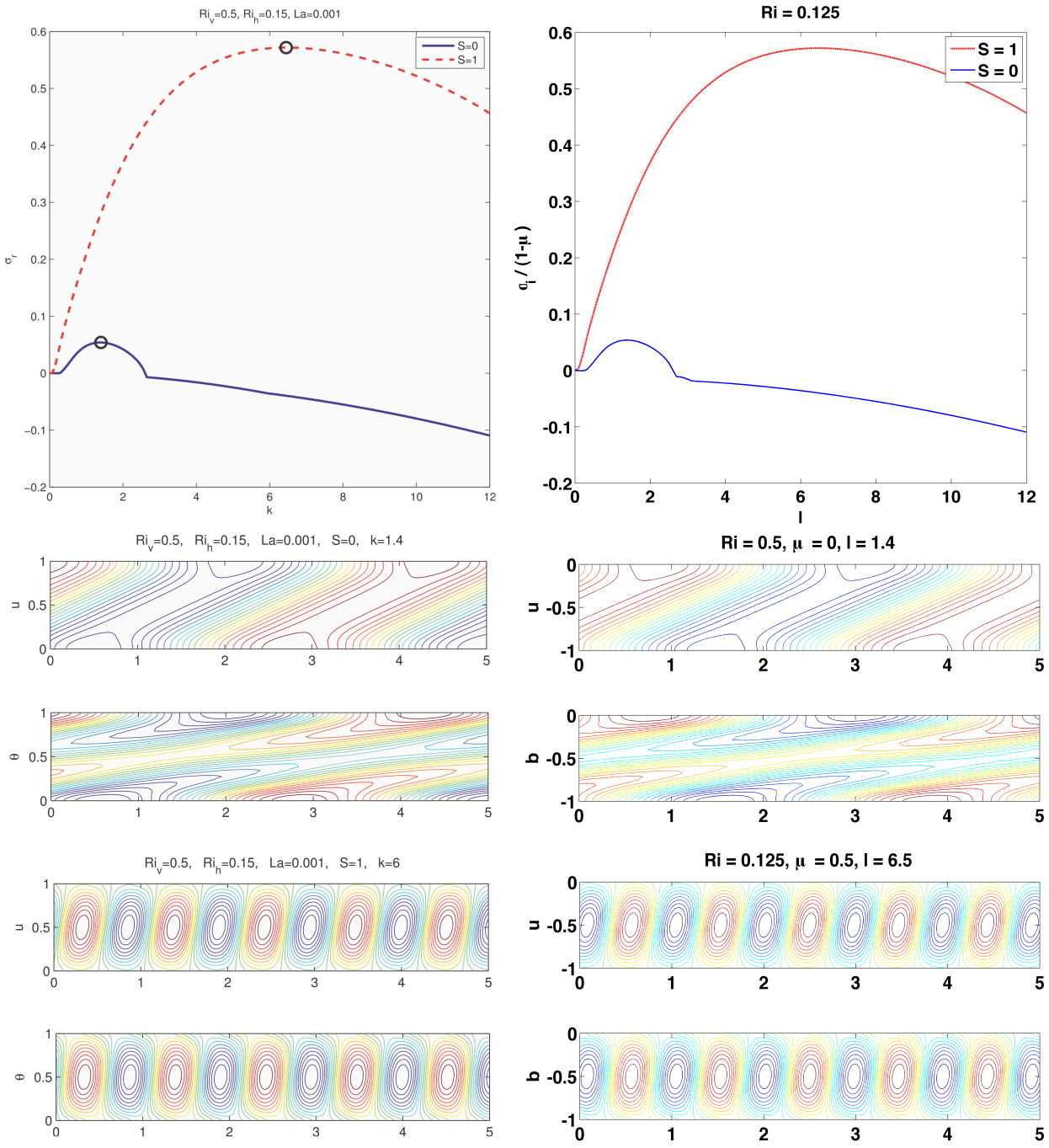

Figure 3.10: As in figure 3.9 but for figure 4 from Li et al. (2012).

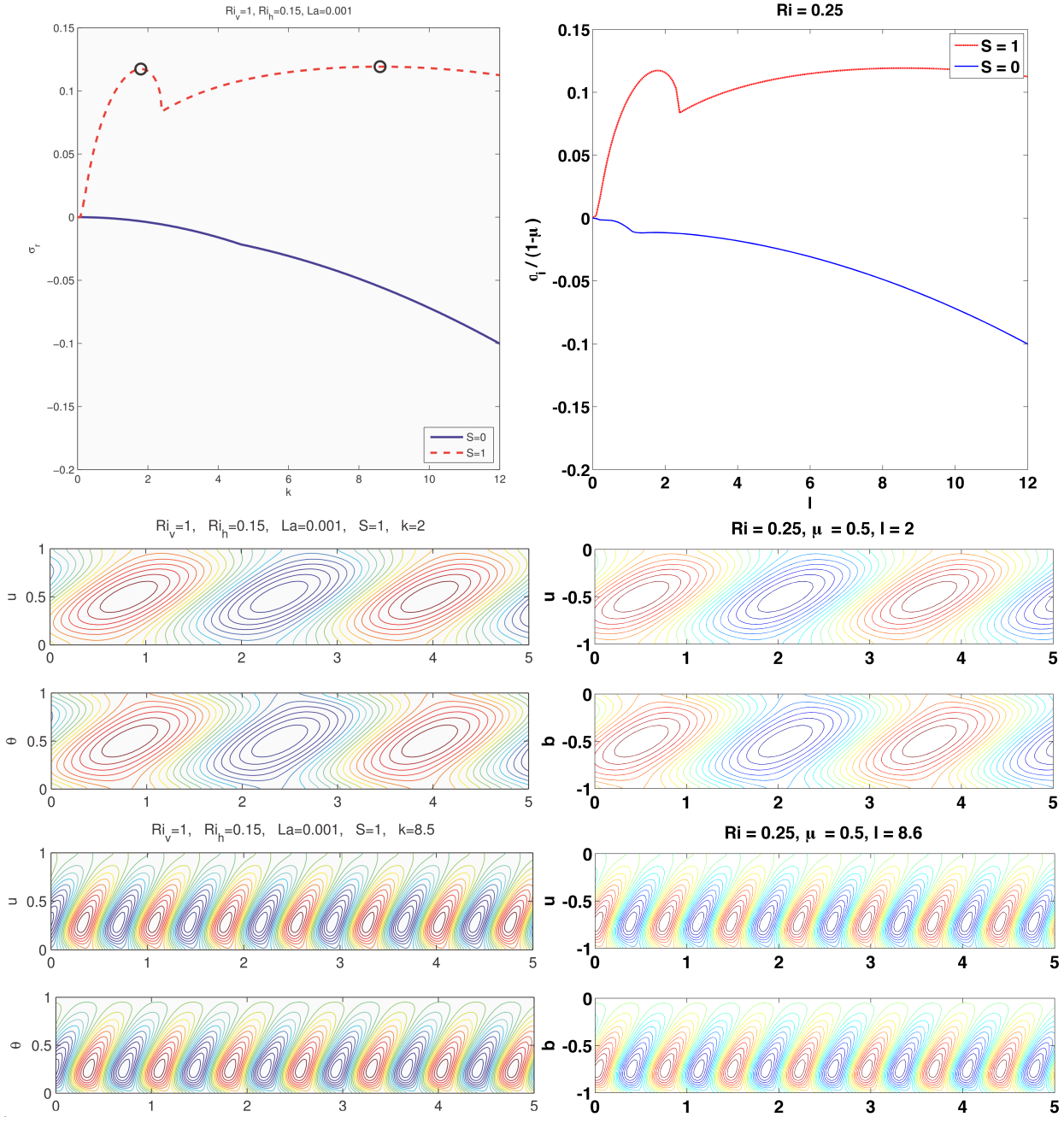

Figure 3.11: As in figure 3.9 but for figure 5 from Li et al. (2012).

Chapter 4

Wave-Front Interactions: Linear Stability

Several instances of wave-front interactions have already been discussed including hybrid LC/SI modes (Li et al., 2012) and the anti-Stokes Eulerian flow that is induced by the Stokes Coriolis force (Gnanadesikan and Weller, 1995; McWilliams and Fox-Kemper, 2013; McWilliams et al., 2014). In this chapter I will explore some consequences of the anti-Stokes Eulerian flow, and perturb many of the instabilities discussed in the previous chapter from their far corners of the vast parameter space toward a more realistic regime.

In a regime in which GI, SI, and LC may all exist, there are several interesting questions that arise relating to the interaction between these modes, however, since this chapter addresses the linear dynamics, mode interactions are entirely absent. Nonetheless, the regime in which all three modes exist, means that GI, and SI will be exposed to Stokes Coriolis and shear forces, while LC will be subjected to additional Eulerian shear through the geostrophic shear, and a horizontal buoyancy gradient. These mean state changes to the flow motivate several questions about what happens to the instabilities within them:

(1) How does the Stokes Coriolis force change the mean flow to affect GI and SI?

(2) Is it the Stokes shear, the Eulerian shear, or the Lagrangian shear that matters most to GI, SI, and LC?

(3) How does the perturbation Stokes shear force ($\mu\lambda u' U_z^S$; the primary driver of LC) act on SI and GI?

(4) How do the energy sources of Stokes altered SI and GI compare their no Stokes counterparts?

(5) How is LC influenced by the change in mean flow due to geostrophic shear?

(6) Does the horizontal buoyancy gradient restrict or enhance the LC due to mixing or restratification?

One might split these questions into two categories: 1) Changes in the horizontal momentum, with changes to the total Coriolis force (likely affecting SI and GI) and total Eulerian shear (possibly affecting SI, GI, or LC), and 2) Changes in the vertical momentum with the Stokes shear force acting on SI and GI, and vertical and horizontal buoyancy advection affecting the LC through the vertical momentum. First the horizontal momentum questions are addressed.

4.1 Analytic Stability Criteria

I will first focus on the inviscid case of the WAB equations to highlight some consequences of the anti-Stokes Eulerian flow. First, to highlight what is meant by the anti-Stokes Eulerian flow, imagine an inviscid, horizontally invariant flow which is in thermal wind balance with a constant horizontal buoyancy gradient (a front). If the front is encountered by remotely generated waves, after about one inertial period, the Eulerian flow adjusts to the presence of the Stokes Coriolis force induced by the waves, and the front is again in thermal wind balance, where the thermal wind is now Lagrangian. This adjustment process has been discussed for finite width fronts and filaments in McWilliams and Fox-Kemper (2013), where they solve for the resulting perturbed buoyancy and velocity fields. In the cases we will consider, the front is effectively infinitely wide, and the only adjustment required is a change in the Eulerian flow. Now we look at the Eulerian flow after Lagrangian thermal

wind balance has been achieved.

$$\hat{\mathbf{k}} \times \overline{\mathbf{U}}_z^L = -\nabla_H \overline{B}, \qquad \textit{or equivalently,} \tag{4.1}$$

$$\hat{\mathbf{k}} \times (\overline{\mathbf{U}}_z + \mathbf{U}_z^S) = -\nabla_H \overline{B} \tag{4.2}$$

Without the Stokes drift, the tilting of planetary vorticity by the Eulerian shear must balance the baroclinic torque. In the presence of Stokes drift, the baroclinic torque is partially balanced by the tilting of planetary vorticity by Stokes shear. Therefore, the resultant Eulerian Coriolis torque can be written as the total necessary Coriolis torque to balance the baroclinic torque minus the Stokes Coriolis torque.

$$\underbrace{\nabla_H \overline{B} - \hat{\mathbf{k}} \times (\mathbf{U}_z^S}_{Eulerian\ Coriolis\ Torque} - \underbrace{\mathbf{U}_z^S}_{Stokes\ Coriolis\ Torque}) = -\nabla_H \overline{B} \tag{4.3}$$

Furthermore, in the absence of any horizontal buoyancy gradient, the Stokes and Eulerian Coriolis torques must exactly balance. This suggests that the dynamics of the Lagrangian flow are unaffected, and that therefore, the wave forcing may not influence the stability of the mean state. On the other hand, a strongly sheared Stokes drift will substantially perturb the Eulerian flow, and therefore any stability criteria that depends on the Eulerian flow will be affected by wave forcing. The following sections present an example of each of these cases.

4.1.1 Wave Forced Geostrophic Instability

Section 3.2 showed that the linear stability model presented in this work can reproduce QG baroclinic instability, however, we will take a step back and consider a more general QG setting in which horizontal variations in geostrophic shear and Coriolis force may exist. These generalizations are not within the capabilities of the numerical linear stability code which has been developed for horizontally invariant mean flows. In this section I adapt the Charney-Stern-Pedlosky criteria for QG baroclinic instability to accommodate a mean flow with Stokes drift. These criteria are a generalization of the Rayleigh stability criterion for linear, incompressible, inviscid flow and Fjortoft's theorem (Eliassen, 1983).

First, consider the QG potential vorticity (QGPV)

$$q = \nabla^2\psi + Ro^{-1}\hat{\beta}Y + (RiRo^2)^{-1}\partial_z\left(\frac{\psi_z^L}{b_z}\right) \tag{4.4}$$

where q has been normalized by $\frac{U^L}{L}$ and $\hat{\beta} \equiv \frac{L}{f_0}f_Y$. Again, recall that baroclinic instability occurs when $(RiRo^2)^{-1} \equiv \left(\frac{L}{L_d}\right)^2 \sim 1$. ψ^L is a stream function that satisfies $u + U^S = -\psi_y^L$, and $v + V^S = \psi_x^L$. If the meridional velocity (v^L) is taken to be zero, then the background $QGPV$ is given by

$$\overline{Q}^L = -\overline{\Psi}_{YY} + Ro^{-1}\hat{\beta}Y + (RiRo^2)^{-1}\partial_z\left(\frac{\overline{\Psi}_z^L}{\overline{B}_z}\right) \tag{4.5}$$

Then the perturbation QGPV is obtained by taking the curl of equation 3.30 and utilizing the hydrostatic relation $b' = \psi'_z$, while the conservation of buoyancy is applied at the boundary (Vallis, 2006).

$$q'_t - \overline{\Psi}_Y^L q'_x + \psi'_x\overline{Q}_Y^L = 0, \qquad -1 < z < 0, \tag{4.6}$$

$$b'_t - \overline{\Psi}_Y^L b'_x + \frac{\gamma\delta}{Ro}\psi'_x\overline{B}_Y = 0, \qquad z = -1, 0, \tag{4.7}$$

where the perturbation velocity-stream function relation is as in the background flow but without Stokes components. The QG perturbations may vary in any direction, and normal mode form is assumed for the along front (x) direction.

$$q' = \psi'_{xx} + \psi'_{yy} + \left(RiRo^2\right)^{-1}\frac{\psi'_{zz}}{\overline{B}_{zz}}, \tag{4.8}$$

$$\psi' = \Re\left[\tilde{\psi}(y,z)e^{ik(x-ct)}\right], \tag{4.9}$$

Then the QGPV and buoyancy conservation (on the boundaries) become

$$(U^L - c)\left(\tilde{\psi}_y y + \left(RiRo^2\right)^{-1}\frac{\psi'_{zz}}{\overline{B}_{zz}} - k^2\tilde{\psi}\right) + \overline{Q}_Y^L\tilde{\psi} = 0, \tag{4.10}$$

$$(U^L - c)\tilde{\psi}_z + U_z^L\tilde{\psi} = 0. \tag{4.11}$$

The energy equation is then formed by dotting $\tilde{\psi}$ into equation 4.10. Then considering the imaginary part of the volume integral of the energy equation,

$$c_i\int_{y_1}^{y_2}\left\{\int_{-H}^{0}\frac{\overline{Q}_Y^L}{|U^L - c|^2}|\tilde{\psi}|^2 dz + \left[\frac{\frac{f_0^2}{N^2}U_z^L}{|U^L - c|^2}|\tilde{\psi}|^2\right]_{-H}^{0}\right\}dy = 0 \tag{4.12}$$

If $c_i \neq 0$, then at least one of the following must be true,

(1) $\overline{Q}_Y^L$ changes sign in the interior of the domain,

(2) $\overline{Q}_Y^L$ is the opposite sign as U_z^L at $z = 0$.

(3) $\overline{Q}_Y^L$ is the same sign as U_z^L at $z = -H$.

(4) U_z^L has the same sign at $z = -H$ and $z = 0$.

Therefore, in order for GI to occur, c_i must be nonzero, so at least one of the above constraints on $\overline{Q}_Y^L$ and U_z^L must be true. This implies that the presence or lack of baroclinic instability is unchanged so long as the QGPV and mean shear are appropriately interpreted in the Lagrangian context as in equation 4.5. This suggests that once the front reaches Lagrangian thermal wind balance, the onset of onset of GI is unchanged, and therefore the Stokes drift appears to do very little to alter GI. However, these are only stability criteria that are derived from the mean state, and do not indicate what changes GI might undergo with the perturbation Stokes shear force acting on them. This will be explored later in this chapter.

4.1.2 Wave Forced Symmetric Instability

As alluded to, when the Stokes Coriolis torque contributes to balancing the baroclinic torque, the Eulerian contribution to the Coriolis torque is altered. In other words, the Eulerian shear is changed. Hoskins (1974) showed that a flow is symmetrically unstable if the PV (now Ertel PV as opposed to QGPV), $q < 0$. Recall that the PV depends on the strength and alignment of the absolute vorticity with the buoyancy gradient ($q = (\nabla \times \mathbf{u}) \cdot \nabla b$). Since the Stokes drift itself does not have relative vorticity, it does not contribute to the PV, however in the Lagrangian thermal wind balance described above, the presence of Stokes drift changes the Eulerian vorticity by creating the anti-Stokes Eulerian flow. In this section I reproduce Hoskins' proof while assuming a mean Lagrangian thermal wind.

Assume the flow is invariant in the direction of the geostrophic flow (which is aligned with the Stokes drift here). The following equation set can be derived from the inviscid dimensional version of equations 3.64-3.67.

$$\omega'_t + U^S_z u'_y - f u'_z - b'_y = 0 \tag{4.13}$$

$$u'_t - f\psi_z - \overline{U}_z \psi'_y = 0 \tag{4.14}$$

$$b'_t + M^2 \psi_z - N^2 \psi'_y = 0 \tag{4.15}$$

$$\omega' + \nabla^2 \psi' = 0 \tag{4.16}$$

Eliminating ω', u', and b', and assuming a normal mode solution of the form $\psi \sim e^{i\sigma t} e^{ik(y \sin\phi + z\cos\phi)}$ yields

$$\left(\frac{\sigma}{\cos\phi}\right)^2 = (N^2 - U^S_z \overline{U}_z)\tau^2 - (f U^S_z + M^2 - f\overline{U}_z)\tau + f^2 + i\frac{\overline{U}_{zz}}{k\cos\phi} \tag{4.17}$$

where $\tau \equiv \tan\phi$. If we consider only Stokes drift profiles with constant shear, we find a necessary criterion for unstable ($\sigma^2 < 0$) modes.

$$fq = \underbrace{f^2 N^2 - M^4}_{Geostrophic\ PV} - \underbrace{f M^2 U^S_z}_{Stokes-modified\ PV} < 0 \tag{4.18}$$

Hoskins original negative PV criterion is obtained, where the anti-Stokes flow has altered the PV. Note that the PV in equation 4.18 is normalized by f to accommodate for either hemisphere. Often the criterion $Ri < 1$ is used in place of the negative PV criterion (e.g. Li et al., 2012; Hamlington et al., 2014), however, no sensible Richardson number may be formed (not with Eulerian, Lagrangian, Stokes, or some geometric mean of shears) to give an equivalent criterion. One can relate the geostrophic Richardson number , Ri^g, to the Stokes shear to form a criterion that depends on Ri^g and the Stokes shear.

$$Ri^g + \mu\cos\theta < 1, \tag{4.19}$$

Where, μ is the shear of a linear Stokes profile. It is clear that in the presence of ageostrophic Eulerian shear, the usual criterion ($Ri^g < 1$) for SI to exist is not accurate, and it is therefore

better to consider the PV since the criterion on Ri was simply derived from the PV criterion while maintaining the assumption that the only shear is geostrophic.

The Stokes altered PV is directly analogous to wind driven PV changes that induce FSI (discussed in section 1.3.3) in that a non-conservative force alters the PV by changing the Eulerian shear near the surface. Recall that down front winds reduce PV. Since it is the anti-Stokes flow that alters the PV, the orientation is opposite, i.e. the PV is reduced (increased) when the Stokes drift is directed up (down) front. This suggests that aligned winds and waves blowing up or down front will have competing effects. The implications of the this change to the background state are that the stability of the layer to SI is very different from what would be inferred from accounting for only the geostrophic velocity. Furthermore, a good estimate of the geostrophic flow, and the surface wind stress can lead to an assumed strong FSI, however if strong waves are present and unaccounted for, the near surface PV will be very different than expected. This means that the turbulence induced by SI will be under or over estimated which will lead to an incorrect estimate of the turbulent fluxes of momentum and buoyancy in the mixed layer. Lastly, it is notable that this section only addresses the Stokes altered mean state, but it is clear from equations 3.8-3.11 that the perturbation Stokes shear force has an influence on the vertical momentum of the perturbed motions (rather than the horizontal momentum of the mean state). The influence of the perturbation Stokes shear force will be addressed in the next several sections and in chapter 5.

4.1.3 Parcel Theory for Symmetric Instability

Since the PV criterion for instability can be somewhat opaque, it is elucidating to consider the available energy for SI. To do this I compute the energy release from switching parcels along a particular path within the Lagrangian thermal wind. This parcel switching analysis has been done by Haine and Marshall (1998) for a flow in thermal wind balance without wave forcing. Here I follow their method exactly, but include the effects of Stokes

drift. The primary assumption is to consider along front tubes of along front Eulerian momentum. Since these tubes are invariant in the along front direction their momentum is conserved ($\frac{Dm}{D_t} = 0$). Then consider the exchange of two of these tubes along some path in the $y - z$ plane. The energy released by this processes is the energy available for SI. Since we are only considering the along front momentum, and there is no along front pressure gradient, the pressure does no work. Also, since the Stokes drift is induced by the waves, it is therefore confined to the surface. The Stokes drift plays a role in advecting momentum, but it cannot be advected itself (see chapter 1 and the WAB equations). Therefore, the along front momentum is composed of three parts: the geostrophic velocity (u^g), the anti-Stokes Eulerian flow (u^E), and the contribution from cross front momentum that has turned into the along front direction due to the Coriolis force ($-fy$), $m = u^g + u^E - fy$. Although the anti-Stokes flow is of greatest interest here, the reader may consider u^E to be any ageostrophic Eulerian flow. Thus as the parcel moves across the front, the change in momentum is given by: $\Delta u = -f\Delta y$. From this change in momentum we can compute the change in kinetic energy (ΔK). The change in potential energy (ΔP) is exactly as in Haine and Marshall (1998). Then the total energy change from parcel switching is

$$\Delta E = \Delta K + \Delta P = \rho_0 \Delta y^2 \left[\underbrace{f^2}_{K_p} - \underbrace{f u_y^g + s M^2}_{GS} - \underbrace{f(u_y^E + s u_z^E)}_{ES} + \underbrace{N^2 s \left(s + \frac{M^2}{N^2} \right)}_{M} \right] \quad (4.20)$$

where s is the slope of the path along which the parcels exchange, and $-\frac{M^2}{N^2}$ is the isopycnal slope. The individual sources of energy are: the kinetic energy required for cross-front motion of the parcels (K_p), the available kinetic energy from the geostrophic shear (GS) and the ageostrophic Eulerian shear (ES), and the potential energy that needs to be overcome which can be thought of as mixing (M), or restratification, and potential energy loss from the front, if this term is negative. Equation 4.20 is written such that a negative ΔE means a loss of energy from the front to the perturbed motions. Therefore, to find the maximum available energy for parcel switching we find the minimum value of ΔE with respect to the path slope,

s, that the parcel takes. This gives the energy available for SI.

$$\frac{N^2\Delta E_{min}}{\rho_0 \Delta y^2} = \underbrace{fN^2\zeta}_{K_p+GS+ES} - \underbrace{M^4}_{GS} + \underbrace{fM^2 u_z^E}_{GS+ES+M} - \underbrace{\frac{1}{4}f^2 u_z^{E,2}}_{ES+M} \tag{4.21}$$

where $\zeta = f - u_y^g - u_y^E$ is the absolute vertical vorticity. The first three terms on the right hand side comprise the PV normalized by f as in equation 4.18. If we take the Eulerian shear (u_z^E) used throughout the parcel switching to be specifically the anti-Stokes Eulerian shear ($-U_z^S$) then we see that the two expressions only differ in the last term on the right hand side of 4.20 (and that the parcel switching accounts for relative vertical vorticity contained in ζ). The final term on the right hand side is the increased kinetic energy due to the anti-Stokes Eulerian shear. Note that this term always increases the energy available for SI (negative ΔE implies the mean state loses energy to a perturbation). This result is at odds with that of section 4.1.2 since there may be available energy but positive PV. This means that the PV criterion is stricter, and that the energy criterion is necessary, but not sufficient. This dissonance will be explored with numerical linear stability calculations in the next section.

4.2 Stokes Modified Baroclinic Instabilities: Numerical Results

The analytic stability criteria of the previous section tell us when GI and SI will exist, but they do not tell us how the growth rates or vertical structures of the instabilities themselves might change with Stokes drift. Furthermore, in deriving the criterion for SI we had to assume that the Stokes drift had constant shear. This is unrealistic, even for the idealized monochromatic waves which will be considered throughout this work. These issues will be examined by numerically solving equations 3.30-3.34 while retaining the Stokes shear force term ($\mu\lambda u' U_z^S$).

Although the Stokes modified criteria for GI (section 4.1.1) was derived for QG perturbations, the dynamics of ageostrophic GI are similar. Furthermore, all the cases that have been tested have a mean shear which does not change sign throughout the flow, and is therefore always unstable to GI. Given that the changes (from no Stokes flow) to the instability

criteria only require considering the Lagrangian velocity, one might expect little or no change in the GI. Figure 4.1 shows growth rates for GI with aligned and anti-aligned Stokes drift. The aligned case shows that the fastest growing mode occurs at higher wavenumber than the anti-aligned case. This is likely due to the fact that GI are the result of interacting edge waves. Nakamura (1988) showed that the reason ageostrophic baroclinic instability occurs at lower wavenumber than QG baroclinic instability (compare figures 3.1 and 3.3) is because the stronger shear in the ageostrophic case reduces the penetration depth of the edge waves, and therefore, the edge waves must be longer in order to interact and form GI. This appears to be the case for Stokes modified GI, and it is the Eulerian shear that is relevant in reducing the penetration depth of the edge waves.

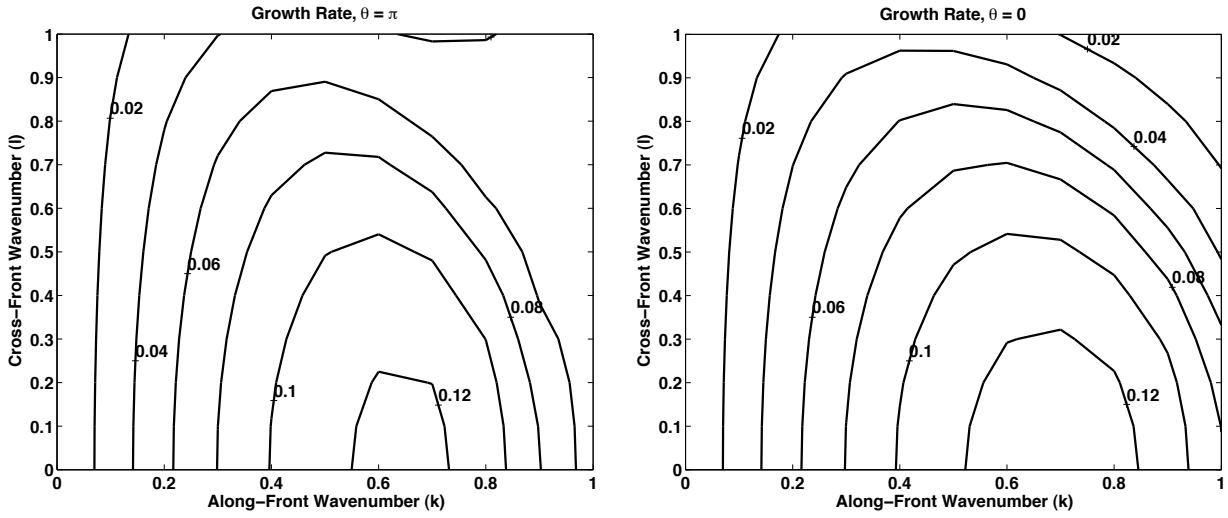

Figure 4.1: Growth rates for GI with aligned ($\theta = 0$) and anti-aligned ($\theta = \pi$) Stokes drift. $Ri = 5$, $\mu = 1$, $\lambda = 5$, $Ro = \delta = 10^{-2}$, $\alpha = 10^{-4}$, $Ek = 0$.

The analytic PV criterion for Stokes modified SI (section 4.1.2) required assuming a constant shear Stokes drift profile. Numerical solutions with exponentially decaying Stokes profiles confirm that SI are active when $PV < 0$. Figure 4.2 shows the cross front velocity for aligned and anti-aligned Stokes drift cases. In the aligned case, the PV below the influence of the Stokes drift is negative, allowing for SI. The anti-Stokes Eulerian flow near the surface

makes the PV positive, making the surface layer stable to SI. In the anti-aligned case the anti-Stokes Eulerian flow destabilizes the surface layer to SI. These cases also show that neither $Ri < 1$ nor $Ri^E \equiv \frac{N^2}{U_z^{E,2}} < 1$ would accurately predict SI.

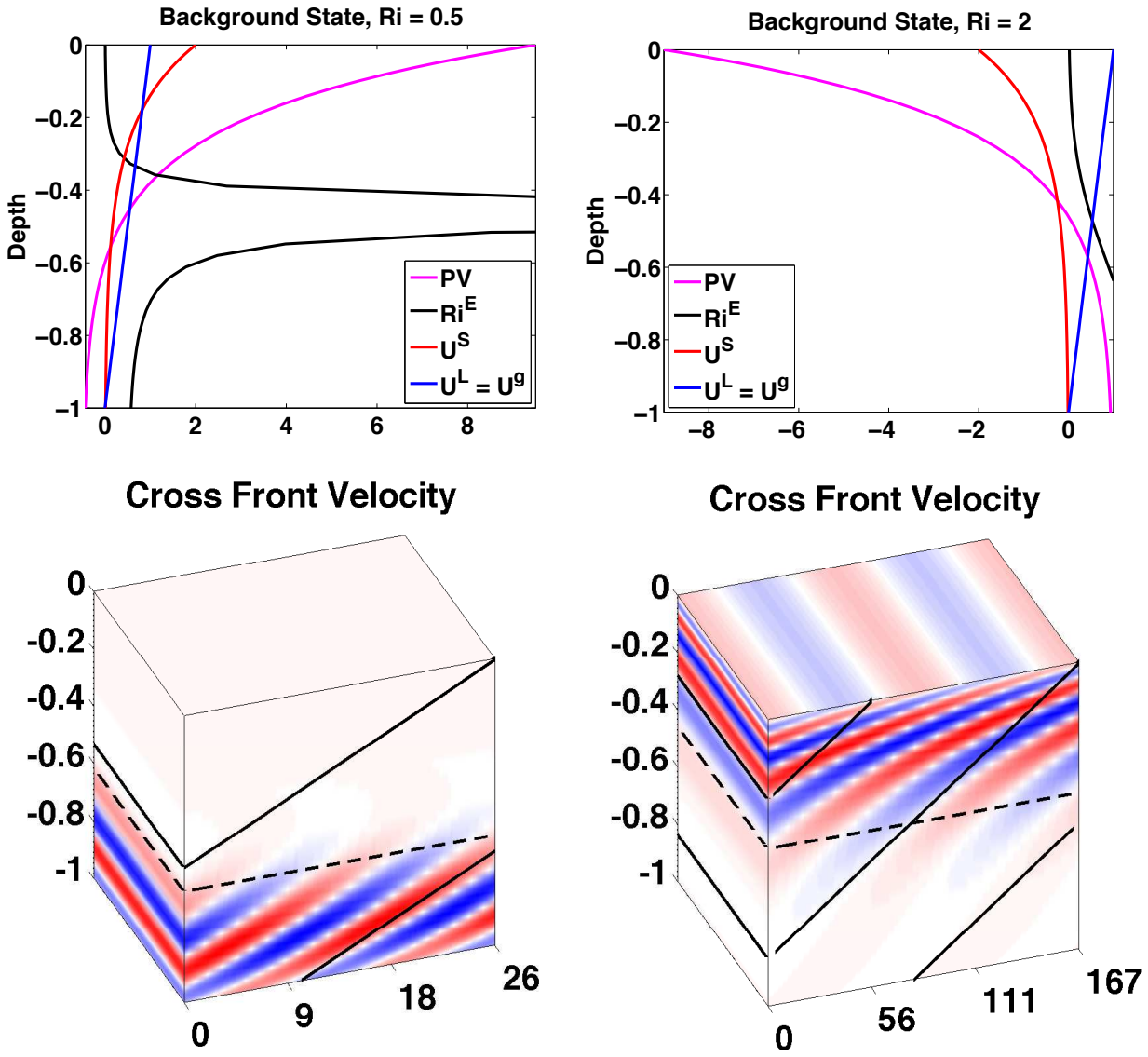

Figure 4.2: (Upper): Profiles of background state conditions for flows with aligned ($\theta = 0$; the $Ri = 0.5$ case) and anti-aligned ($\theta = \pi$; the $Ri = 2$ case) Stokes drift. (lower): Cross-front velocity (v') for the fastest growing modes in each case. The thick black contours show isopycnals. The dashed line is the $PV = 0$ line. In both cases, $\mu = 2$, $\lambda = 5$, $Ro = \delta = 10^{-2}$, $\alpha = 10^{-4}$, $Ek = 0$.

Within the negative PV regions, the paths of strongest cross front velocity (the par-

cel switching paths) become shallower where the anti-Stokes Eulerian shear is stronger, and steeper where it becomes weaker (or negative). This implies that although the parcel switching analysis does not provide a sufficient criterion for instability, when the PV is also negative, the active SI extract energy as predicted by equation 4.21.

Haine and Marshall (1998) say that "...the stability of the layer will depend on the sign of ∇b measured in the [momentum] surface (corresponding to gravitational instability) or the sign of the absolute vorticity normal to the [buoyancy] surface (corresponding to centrifugal instability). Both viewpoints are complementary and entirely equivalent." Although both interpretations imply negative PV criteria for instability, it appears untrue that both viewpoints are entirely equivalent when the momentum surfaces do not coincide with the isopycnals. This can be seen in the lower right panel of figure 4.2. The instabilities move along a path that is closer to the momentum surfaces where the anti-Stokes Eulerian flow is strong. This is because in the momentum surface, there is no loss of momentum (from $-f\Delta y$) when moving horizontally. Therefore, when the momentum surfaces are closer to horizontal, more potential energy may be extracted from cross isopycnal exchange because the gains from the potential energy are far greater than the energy used in parcel switching. The closer the parcel switching path is to the momentum surface, the more appropriate the "slantwise convection" interpretation is. When the parcel paths are in the isopycnals, the centrifugal instability interpretation is most appropriate. In reality, SI is a combination of these two mechanisms, and the degree to which each contributes: 1) depends on the shapes of the momentum surfaces and isopycnals and 2) determines the rate of buoyancy and shear production. More slantwise convection implies more buoyancy production, whereas more centrifugal instability implies more shear production.

Figure 4.3 shows vertical profiles of the Reynolds stress terms that contribute to buoyancy and shear production for the SI in figure 4.2. In the case where SI only appear at depth, the ESP is dominant. This is unsurprising because as figure 4.2 shows the motions are mostly along isopycnals there (and so BP cannot be accomplished). Therefore, the cen-

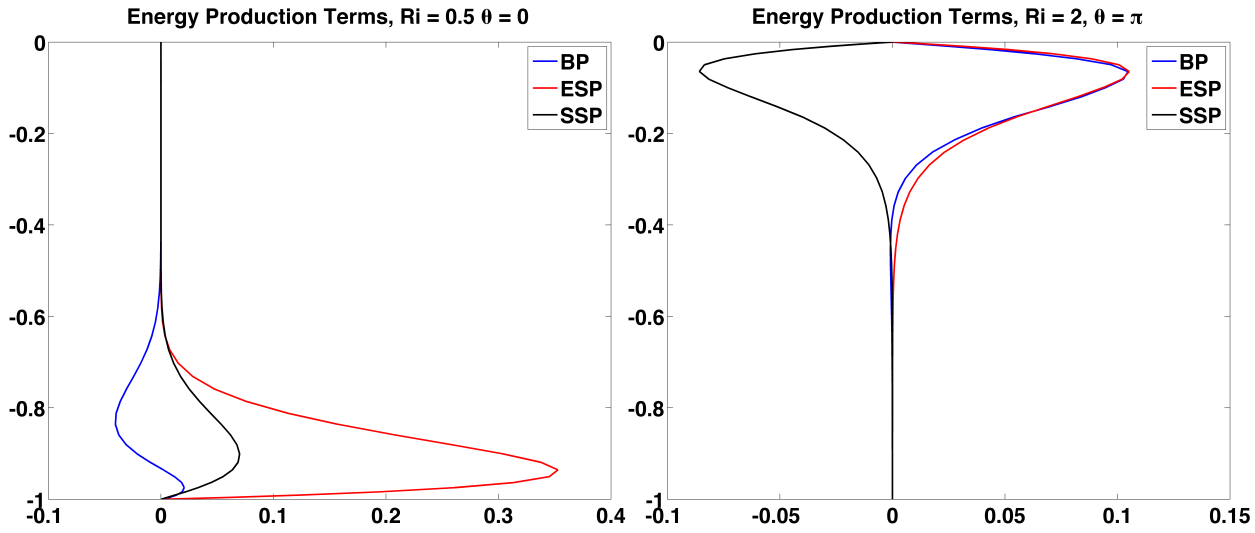

Figure 4.3: a-b): Profiles of Reynolds stress terms ($BP \sim \overline{w'b}'$, $ESP \sim \overline{u'w'U}_z$, and $SSP \sim \overline{u'w'U}_z^S$) for flows with aligned ($\theta = 0$; the $Ri = 0.5$ case) and anti-aligned ($\theta = \pi$; the $Ri = 2$ case) Stokes drift as in figure 4.2. Recall, $\mu = 2$, $\lambda = 5$, $\gamma = 1$, $Ek = 0$, $\alpha = 10^{-4}$, and $Ro = \delta = 10^{-2}$.

trifugal instability interpretation of SI is most appropriate. In the case where the Stokes modified PV makes the surface layer unstable to SI, ESP and BP are comparable in magnitude (right panel of figure 4.3). This is again unsurprising because in figure 4.2 the SI are more aligned with the momentum surfaces. A mixed centrifugal, slantwise convective instability interpretation is relevant for this case. Therefore, this is a mechanism by which Stokes drift may indirectly drive restratification.

Every mean flow with negative PV (except when the perturbed motions are forced to be strongly non-hydrostatic) that was tested (not shown) was unstable to SI regardless of Ri or Ri^E. Furthermore, every mean flow with positive PV was stable to SI. This reaffirms the proof in section 4.1.2 that negative PV is a necessary condition for SI, and it suggests that this is also sufficient. This however, only addresses the mean flow affect of Stokes drift. The perturbation Stokes shear force ($\mu\lambda u' U_z^S$) may also affect SI and GI. This is very apparent in figure 4.3 since SSP is identically the work done on the perturbed motion by the Stokes shear force. In the context of SI, SSP is positive when the Stokes and Eulerian shears are

aligned. This is because SI act to restore the PV to zero, and the only way to do this through shear production is through Eulerian shear production because it is only the Eulerian shear that affects the PV. Therefore, when SI are active, the sign of $\overline{w'b'}$ will always be the same as the sign of the Eulerian shear. This implies that SSP is positive when the Stokes and Eulerian shears are aligned. In the context of figure 4.3, SSP is negative in the right panel because near the surface, the Stokes and anti-Stokes flows directly oppose each other, and the Eulerian part of the geostrophic flow is not strong enough to change the sign of the total Eulerian flow. In the left panel, at depth the Eulerian geostrophic flow is stronger than the anti-Stokes flow, and therefore the net Eulerian flow (and shear) is positive, which aligns with the Stokes shear, resulting in positive SSP.

4.3 Viscid Instabilities

The previous section only addressed inviscid baroclinic instabilities. Here I will explore a wider range of the parameter space to characterize how each instability mechanism changes with each of the parameters. First we must have a mean flow that can be unstable to all of the instabilities discussed in Chapter 3, and this requires a viscid flow. Beginning from equations 3.8-3.11, assume $Ro << 1, \delta < 1, Ek \lesssim Ro$. The first two assumptions allow the neglect of all nonlinear terms. The mean flow must satisfy

$$\nabla_H \overline{P} + \hat{\mathbf{k}} \times \overline{\mathbf{U}}^L - Ek\nabla_H^2 \overline{\mathbf{U}} - \frac{Ek}{\alpha^2}\overline{\mathbf{U}}_{zz} = 0 \tag{4.22}$$

$$\overline{P}_z - \overline{B} = 0 \tag{4.23}$$

$$\overline{B}_T + \frac{\gamma}{RoM_r}(\overline{\mathbf{U}}^L \cdot \nabla_H)\overline{B} + \frac{RoRi}{\delta}\overline{W}\ \overline{B}_z - \frac{Ek}{RoPr\alpha^2}\overline{B}_{zz} = S^B \tag{4.24}$$

$$\nabla_H \cdot \overline{\mathbf{U}} + \frac{1}{\delta}\overline{W}_z = 0, \tag{4.25}$$

$$\overline{W} = 0, \quad \textit{and,} \quad \overline{B}_z = 1 \quad \textit{at} \quad z = 0, -1,$$

$$\overline{\mathbf{U}}_z = \hat{\tau} \quad \textit{at} \quad z = 0, \quad \textit{and,} \quad \overline{\mathbf{U}}_z = \gamma \quad \textit{at} \quad z = -1.$$

S^B is an external buoyancy source that exactly balances the horizontal advection term. In the Stokes-Ekman layer examined in Gnanadesikan and Weller (1995), the buoyancy equation is absent, however, the mean state (3.52) used to reproduce their results is perhaps the closest example already presented that would solve the above equations, but it does not allow for baroclinic instabilities. Therefore, the assumption of S^B will allow for a steady horizontal buoyancy gradient that affects the perturbation without tipping over due to the Ekman flow. A steady state solution to the above equations is as follows:

$$\begin{aligned} \overline{U} + i\overline{V} &= \frac{1}{(1+i)\eta}\left[\hat{\tau}e^{i\theta^e} - \gamma - \frac{2i\lambda\mu e^{i\theta}}{(\frac{\lambda}{\eta})^2 - 2i}\right] e^{(1+i)\eta z} + \gamma z + \frac{2i\mu e^{i\theta}}{(\frac{\lambda}{\eta})^2 - 2i} e^{\lambda z} \qquad (4.26) \\ \overline{W} &= 0, \qquad \overline{B} = Y + z, \qquad \overline{P} = Yz + \frac{1}{2}z^2, \end{aligned}$$

This solution is derived in appendix C. This mean state is depicted in figure 4.4. With this mean flow, the perturbation equations are

$$\frac{Ro}{\delta}\left[\mathbf{u}'_t + (\overline{\mathbf{U}}^L \cdot \nabla_h)\mathbf{u}' + w'\,\overline{\mathbf{U}}_z + \nabla_h p'\right] + \hat{\mathbf{k}} \times \mathbf{u}' - \frac{Ek}{\alpha^2}\mathbf{u}'_{zz} - \frac{Ek}{\delta^2}\nabla_h^2\mathbf{u}' = 0 \qquad (4.27)$$

$$\frac{\alpha^2}{\delta^2}\left[w'_t + (\overline{\mathbf{U}}^L \cdot \nabla_h)w'\right] + \mu\lambda\mathbf{u}' \cdot \overline{\mathbf{U}}^S_z + [p'_z - b'] - \frac{Ek}{Ro\delta}w'_{zz} - \frac{Ek\alpha^2}{Ro\delta^3}\nabla_h^2 w' = 0 \qquad (4.28)$$

$$\left[b'_t + (\overline{\mathbf{U}}^L \cdot \nabla_h)b'\right] + \frac{\delta\gamma}{Ro}(\mathbf{u}' \cdot \nabla_H)\overline{B} + Riw'\overline{B}_z - \frac{Ek\delta}{RoPr\alpha^2}b'_{zz} - \frac{Ek}{RoPr\delta}\nabla_h^2 b' = 0 \qquad (4.29)$$

$$\nabla_h \cdot \mathbf{u}' + w'_z = 0 \qquad (4.30)$$

$$w' = 0, \quad \textit{and,} \quad \mathbf{u}'_z, b'_z = 0 \quad \textit{at} \quad z = 0, -1, \qquad (4.31)$$

$$w'_{zz} = 0 \quad \textit{at} \quad z = -1,$$

First, before drifting far from the most familiar versions of all of the instabilities of interest, I will show how the growth and energy sources of each mode change as a function of each dimensionless parameter. Initially, this is done near the limit that would yield the classic version of that mode (e.g. the inviscid, non-hydrostatic limit for SI and GI). The non-dimensional parameters for the classical cases of each instability and their perturbed range is given in table 4.1. It is convenient at this time to point out that the motions of the perturbations depend on the small scale Rossby number ($Ro' \equiv \frac{Ro}{\delta} = \frac{U}{fl}$) and small

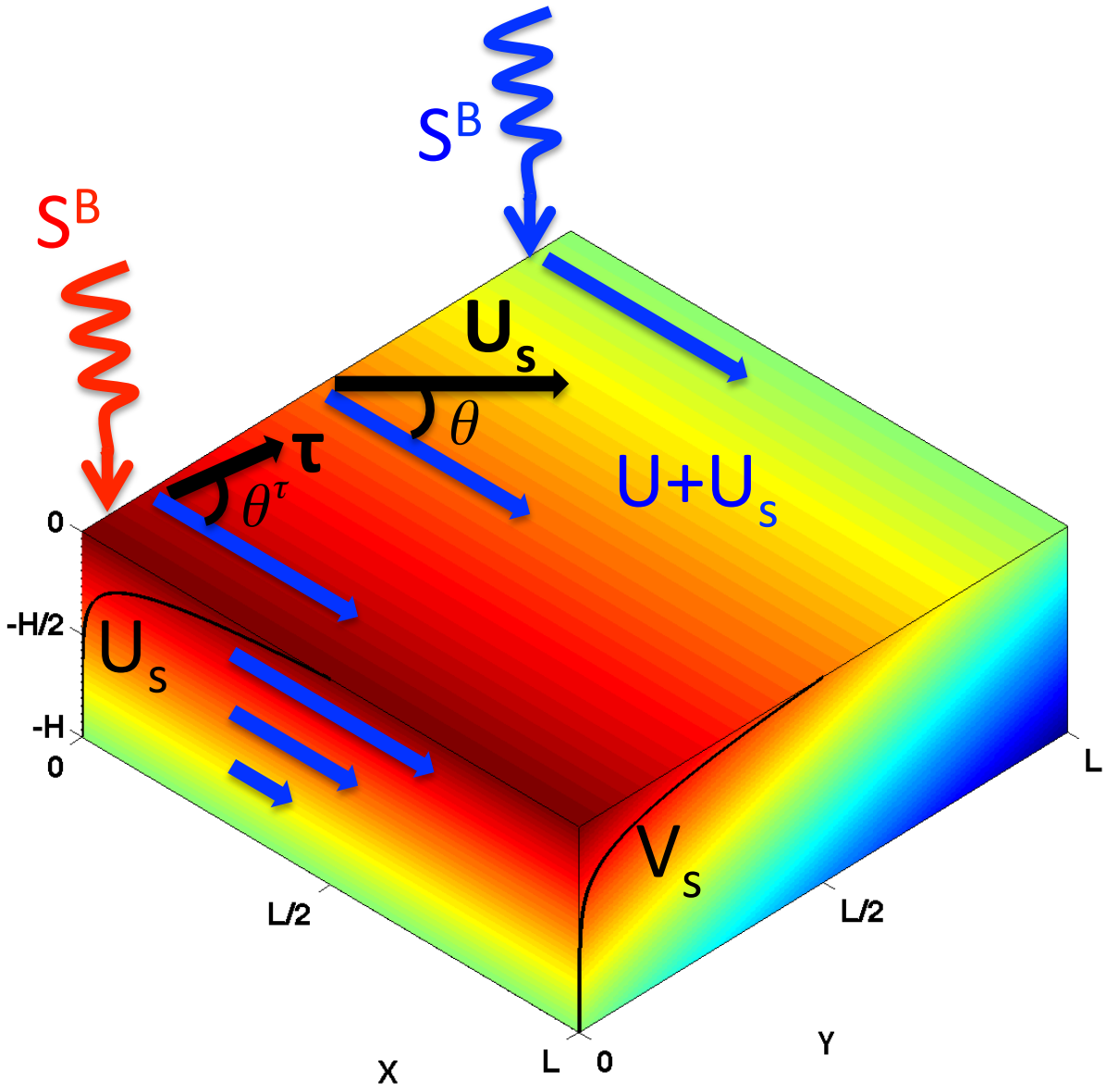

Figure 4.4: The mean state with wind stress, τ, Stokes drift, U^S, and a front with a geostrophic flow (blue) is depicted. The stabilizing external buoyancy source is also shown.

scale aspect ratio ($\alpha' \equiv \frac{\alpha}{\delta} = \frac{H}{l}$). To determine the dependence of each mode on the non-dimensional parameters, equations 4.27-4.31 are solved over the parameter range in table

Instability	GI	SI	LC
Ri	1.7 ± 0.1	0.5 ± 0.1	0.02 ± 0.01
γ	1 ± 0.1	1 ± 0.1	0.1 ± 0.05
$\mu\lambda$	0.2 ± 0.1	0.2 ± 0.1	0.3 ± 0.1
λ	20 ± 15	20 ± 15	20 ± 15
$\alpha' \equiv \frac{\alpha}{\delta}$	0.01 ± 10^{-3}	0.01 ± 10^{-3}	1 ± 0.1
$Ro' \equiv \frac{Ro}{\delta}$	1 ± 0.1	1 ± 0.1	100 ± 10

Table 4.1: The nondimensional parameters and their perturbations for a typical case of each instability.

4.1. The power law behavior is determined as follows:

$$a_1 = \frac{\partial(log(\sigma))}{\partial(log(Ri))}, \tag{4.32}$$

where $a1$ is then the exponent for Ri, i.e. $\sigma \sim Ri^{a_1}$, and similarly for the other non-dimensional parameters. The growth rate, and energy production for GI depend on the non-dimensional parameters as follows:

$$\sigma \sim Ro'^{1.59} Ri^{-0.83} \alpha'^{0.21} \gamma^{0.11} \lambda^{-0.0045} \mu\lambda^{0.0023} \tag{4.33}$$

$$BP \sim Ro'^{5.6} Ri^{-1} \gamma^{-0.38} \alpha'^{-0.05} \lambda^{-0.0065} \mu\lambda^{10^-4} \tag{4.34}$$

$$ESP \sim Ro'^{9.4} Ri^{-0.99} \gamma^{-0.18} \lambda^{0.012} \alpha'^{0.0071} \mu\lambda^{0.004} \tag{4.35}$$

As has been shown previously, the growth rate scales inversely with a fractional power of Ri (Stone, 1966). The dependence is slightly different here ($Ri^{-0.83}$ vs $Ri^{-0.5}$ in Stone (1966)). however, that is likely partly due to the higher Ri, and presence of Stokes drift. Ro' also substantially effects the growth rate, and all energy production terms. This demonstrates that these ageostrophic baroclinic instabilities are still very rotationally constrained, and even more ageostrophic motions would grow faster and be more energetic. The dependence on small scale aspect ratio, geostrophic shear, Stokes shear and Stokes depth are all quite weak.

The growth rate and energy production terms for SI have some similar dependencies

to GI on the non-dimensional parameters.

$$\sigma \sim \gamma^{2.3} Ri^{-1.1} Ro'^{1.1} \alpha'^{0.11} \mu\lambda^{10^{-4}} \lambda^{10^{-4}} \tag{4.36}$$

$$BP \sim Ri^{8.5} \alpha'^{-1.22} \lambda^{-0.50} Ro'^{0.22} \gamma^{0.0055} \mu\lambda^{0.05} \tag{4.37}$$

$$ESP \sim \gamma^{2.3} Ro'^{0.94} Ri^{-0.066} \alpha'^{0.059} \mu\lambda^{-0.030} \lambda^{0.03} \tag{4.38}$$

SI also weakens when Ri is increased, and the dependence is stronger than with GI. SI is also strongly rotationally constrained as is evident by the increased strength with larger Ro', although this dependence is weaker than for GI. SI are most strongly dependent on the strength of the geostrophic shear (γ) which is unsurprising since they are driven primarily by ESP. As with GI, with such weak wave forcing, SI are only very weakly dependent on the Stokes shear ($\mu\lambda$) and Stokes depth (λ), however, the presence of Stokes drift appears to slightly increase the growth rate and energy production. Note that for the range of parameters explored, the PV is almost always negative. This is then consistent with the idea that if the PV is negative, the total available energy (equation 4.21) can be utilized, and the anti-Stokes Eulerian shear always increases this available energy. Figure 4.5 shows this modest change in growth rate for various values of Ri and $\mu\lambda$. Note that as the PV becomes positive near the surface due to the anti-Stokes Eulerian shear (when $Ri = 0.7$, $\mu\lambda = 0.3$, $PV \approx Ri - 1 + \mu\lambda \sim 1$), the Stokes perturbations reduce the growth rate because energy may only be extracted from the flow below the Stokes layer, where the PV is still negative, just as in the lower left panel of figure 4.2.

As expected, the dependence on the non-dimensional parameters is quite different for LC.

$$\sigma \sim \alpha'^{-2.5} \mu\lambda^{1.6} Ro'^{-1.5} \lambda^{-1.4} Ri^{-1.1} \gamma^{0.44} \tag{4.39}$$

$$BP \sim \alpha'^{-1.22} \lambda^{-1.2} \mu\lambda^{0.96} Ro'^{0.22} Ri^{0.072} \gamma^{0.0055} \tag{4.40}$$

$$ESP \sim \alpha'^{-1.7} \lambda^{-1.1} \mu\lambda^{1.0} Ro'^{0.82} Ri^{-0.90} \gamma^{0.42} \tag{4.41}$$

$$SSP \sim \mu\lambda^{2.3} \lambda^{-1.9} \alpha'^{-1.8} Ro'^{0.95} Ri^{-0.87} \gamma^{0.41} \tag{4.42}$$

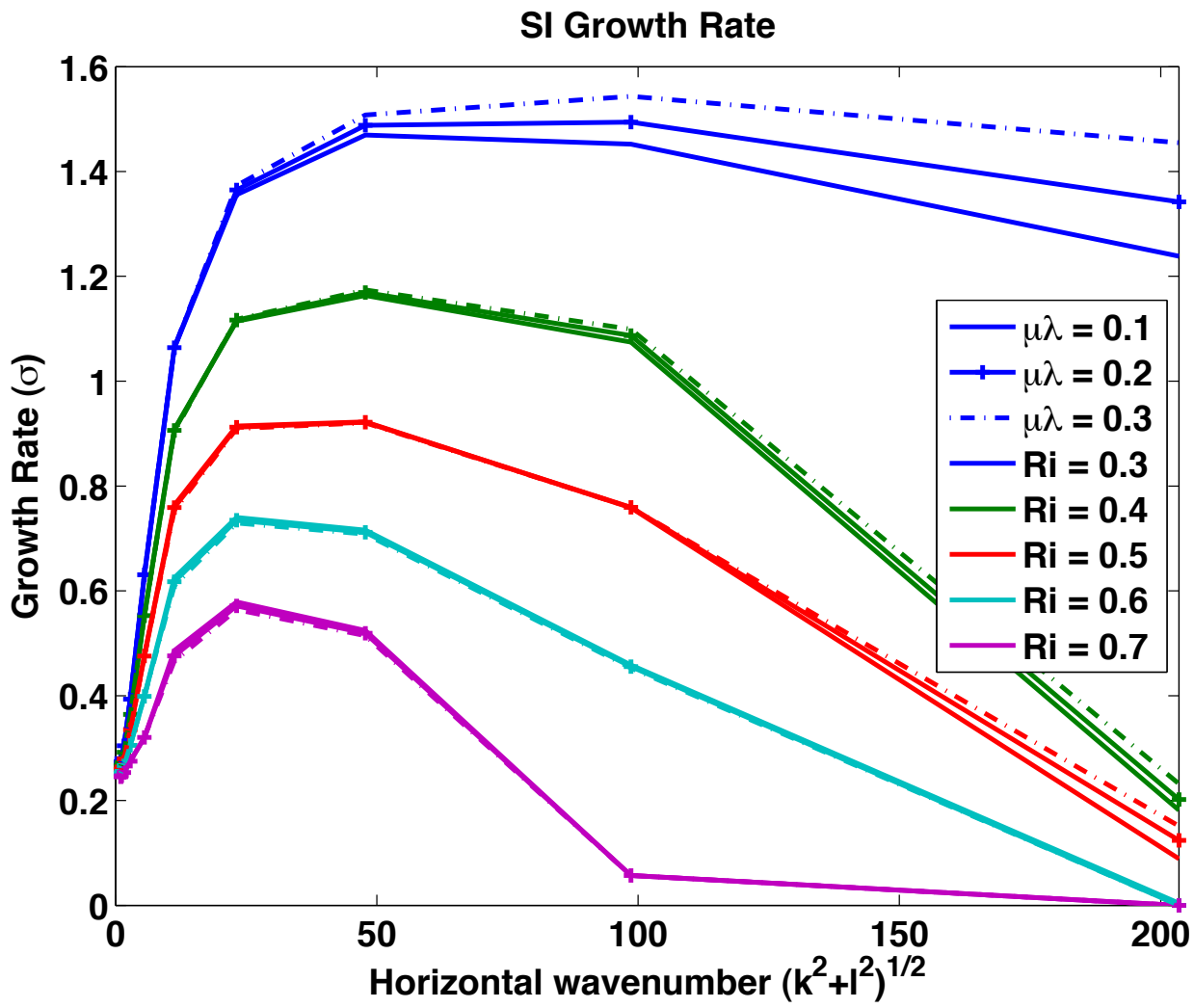

Figure 4.5: Growth rates for SI as a function of horizontal wavenumber for five values of Ri and three values of Stokes shear ($\mu\lambda$).

Since LC get their energy from a combination of SSP and ESP, it is unsurprising that the growth rate and energy production are strongly dependent on the Stokes shear. Decreasing the Stokes depth (increasing $\lambda \equiv \frac{H}{H^S}$) reduces the depth over which the LC act, and therefore reduces their total growth rate and energy production since they are confined to a smaller volume. As with the other instabilities, constraining LC to be partially (in fact only slightly here) geostrophic reduces the growth rate. As has been shown previously (Leibovich and

Paolucci, 1981), LC are generally weakened by increased vertical stratification (Ri). The presence of a front (geostrophic shear, γ) slightly increases the strength of LC. This is unsurprising, and consistent with the fact that LC derive their energy from both SSP and ESP. Since the front and Stokes drift are aligned in all the cases in this section, the increased geostrophic shear increases the total Eulerian shear that is useable by LC. The changes due to geostrophic shear are not as substantial as those due to Stokes shear, but the changes in geostrophic shear are noticeable. Figure 4.6 shows the marginal stability curves for LC as a function of Stokes shear, wavenumber, and geostrophic shear. This figure is analogous to figure 3.5, but with the wavenumbers and non-dimensional parameters ($\mu\lambda$) used in the present linear stability model.

These instabilities represent fairly small perturbations from their respective classical regimes, which are all somewhat far from the regime in which the real ocean typically resides. Specifically, the Stokes shear is often much stronger than the geostrophic shear. Nevertheless, the dependence of each instability on the dimensionless parameters serves as a useful guide to finding a place in parameter space where all of these instabilities might exist. The next section explores a more realistic regime for the ocean mixed layer.

4.4 Instabilities in a Realistic Mixed Layer

To determine the most realistic non-dimensional parameters given the dimensional scales of the ocean mixed layer, it is helpful to start with the waves. Although we are using idealized monochromatic waves, we can choose realistic parameters for the wave height and period. Monochromatic Stokes drift has the form

$$U^S = 2a_w^2 k_w \sigma_w e^{2k_w z} \tag{4.43}$$

where a_w, k_w, and σ_w are the wave amplitude, wavenumber, and frequency respectively. For a swell with a 4.5 s period ($\frac{2\pi}{\sigma_w}$), we can compute the wavelength and therefore the Stokes

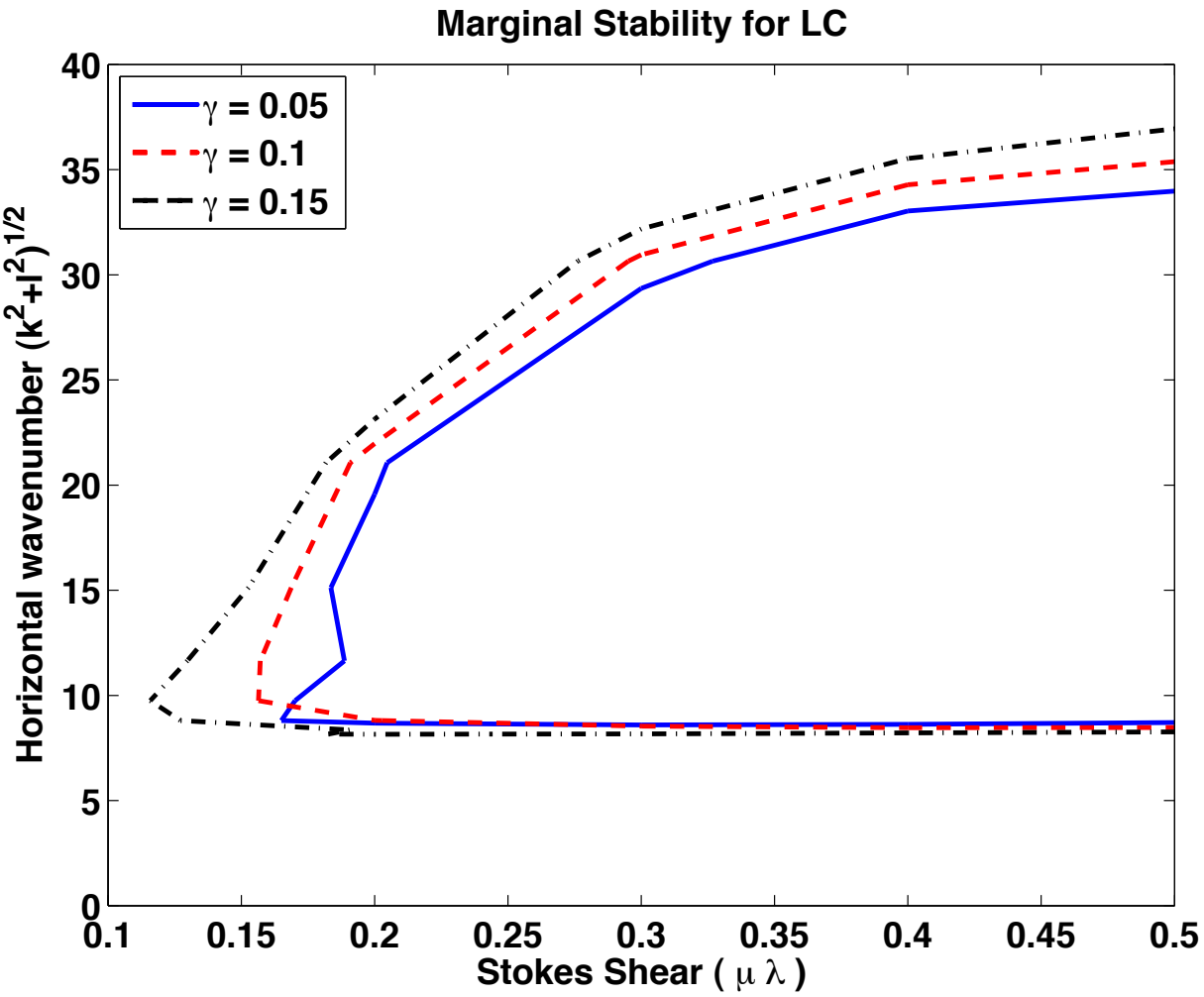

Figure 4.6: LC marginal stability curves ($\sigma = 0.01$) for three values of geostrophic shear (γ). The unstable region is bounded by the curves, outside of these curves, the flow is stable to LC.

depth using the deep water dispersion relation.

$$\sigma = \sqrt{gk} \tag{4.44}$$

$$H^S = (2k)^{-1} = \frac{g}{2\sigma^2} \tag{4.45}$$

This implies a Stokes depth of roughly 2.5 m (and a wavelength of $\approx$ 30 m), and for a 50 m deep mixed layer, $\lambda = 20$. To determine the Stokes shear we also need to know the amplitude of the waves, so we will assume $1m$ waves. Then the Stokes shear is $\approx 0.2\ s^{-1}$.

As discussed in chapter 1, for fully developed waves, $La_t \approx 0.3$. The surface Eulerian shear, which is maintained by the wind stress, can be computed as follows:

$$La_t = \sqrt{\frac{u^*}{U^s}}, \qquad u^{*,2} = \nu U_z^E, \tag{4.46}$$

$$\frac{La_t^{-4}\nu}{U^S} = U_z^E \tag{4.47}$$

If we pick an eddy viscosity $\nu = 10^{-2}$, then the Eulerian and Stokes shears are of the same magnitude, and therefore, $\mu\lambda \sim \frac{1}{2}$. Then the total Lagrangian shear is $\approx 0.4s^{-1}$. Boccaletti et al. (2007) report the near surface geostrophic shear to be $[1-5]\times 10^{-4}\ s^{-1}$ and the near surface vertical buoyancy gradient N^2 to be $10^{-6}-10^{-7}\ s^{-1}$. This implies that $\gamma \sim [2.5-10]\times 10^{-4}$, and $Ri \sim 6\times[10^{-7}-10^{-6}]$. The linear stability of this realistic regime will be explored with $Ri = 2\times 10^{-7}$, $\gamma = 6\times 10^{-4}$, $\mu\lambda = 0.9$, $\lambda = 20$, $\eta = 15$, $Ro' = 10$, $\alpha' = 10^{-3}$, and $\theta = 0$. This choice represents a very wavy, very weakly stratified mixed layer with a fairly strong front that is aligned with the waves.

First, it is common with linear stability to seek the fastest growing mode with the assumption that this mode attains a finite amplitude faster than other modes, and is therefore the dominant feature of the ensuing turbulence. This scenario is perhaps most believable when the mean flow is uniform, and the most unstable modes are unstable throughout the domain. Given the strong surface forcing from wind and waves, the fastest instabilities that develop near the surface cannot exist at depth. As such, it is helpful to consider two or three separate layers which are naturally defined by the three vertical length scales: the full mixed layer depth, H, the Stokes depth, H^S, and the Ekman depth, H^E. With the results of the previous section, and the previous chapter, one expects a near surface LC layer, a transition layer of some kind, and a deeper layer comprised of the rest of the mixed layer, and dominated by baroclinic (both GI and SI) instabilities. If the Stokes layer is deeper than the Ekman layer, one might expect the dynamics in the transition layer to be dominated by the Stokes modified baroclinic instabilities discussed in sections 4.1-4.2. If the Ekman depth is greater than the Stokes depth, similar instabilities may ensue since the Ekman shear alters

the PV just like the anti-Stokes shear, but since it turns with depth, the orientation will not always favor increased or reduced PV. It is clear from the analyses of these independent layers that the growth rates for each instability are different, yet may not dominate the structure of the entire mixed layer. It is also extremely clear from non-linear simulations (e.g. Hamlington et al., 2014) that despite quickly developing LC, the mixed layer eddies are slower to develop as expected, but are not remotely dominated by LC.

The linear stability of the realistic regime discussed above reveals all three instabilities: LC, SI, and GI. There are in fact many more, particularly surface intensified shear instabilities, but I will focus on the ones which have been discussed up to this point. First, as expected LC are the fastest growing mode with an e-folding time (τ) of seconds. They are strongly surface confined, which is unsurprising given the shallow Stokes and Ekman depths. Also as expected, they extract energy from the Eulerian shear, and the Stokes shear force does positive work on them to make them more unstable (see table 4.2). Figure 4.7 shows the fastest growing mode, which is LC. The horizontal length scale (l) for one period of the LC is about 25 m, which is consistent with observations. They are rotated ≈ 0.4 radians to the right of the front and Stokes drift (which are aligned). This is roughly twice the predicted value based on the Lagrangian shear direction integrated over the full depth of the mixed layer. Van Roekel et al. (2012) say that with strongly misaligned cases like this, the mean vorticity biases the LC direction toward larger angles.

SI also exist, and although they are a sub-dominant mode for this wavenumber, the faster modes all act exclusively in the thin Stokes and Ekman layers while SI act on the deeper part of the mixed layer. Figure 4.8 shows the Stokes and Ekman modified SI mode. The length scale of the SI mode (not shown) is about 160 m, which is consistent with the viscid linear stability SI mode in the absence of wave forcing, as well as non-linear simulations (e.g. Thomas et al., 2013). The e-folding time (5 h) is consistent with the SI mode in the absence of wave forcing. The intensity of the SI varies more with depth than in the inviscid case due to the rotating Ekman shear. When aligned with the geostrophic shear, the Ekman

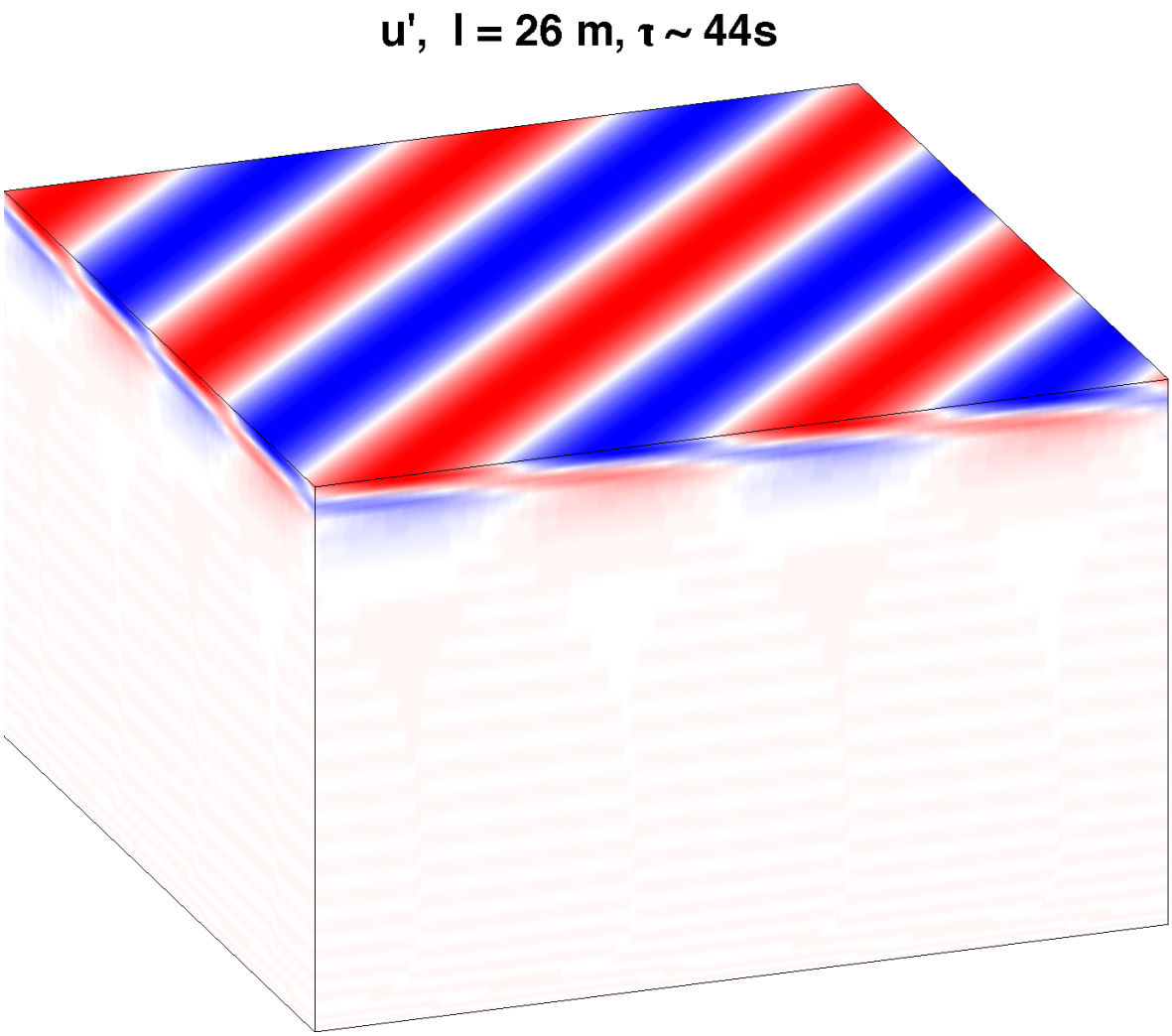

Figure 4.7: Perturbation down front velocity (u') of the fastest growing mode is shaded.

shear reduces the PV. The SI are rotated to the right due to the Ekman shear, with the fastest growing mode at an angle 0.17 radians to the right of the geostrophic shear. As discussed in section 4.1.3, since the PV is negative throughout the lower part of the layer, and the SI will arrange themselves to extract the most energy, which includes extracting Ekman shear.

GI are also present, and in a fairly unperturbed form. Again, the GI are a sub-dominant

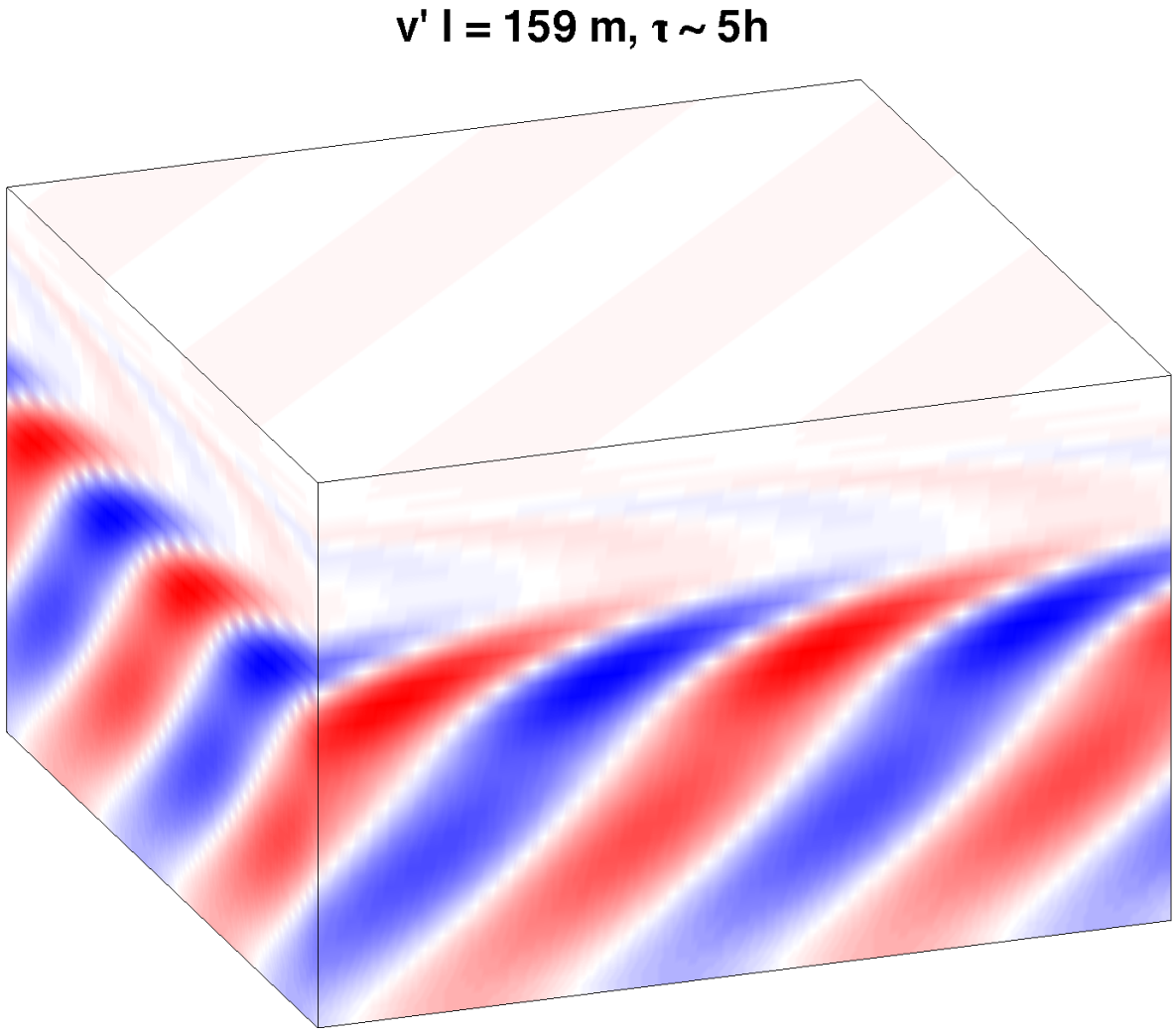

Figure 4.8: Perturbation cross front velocity (v') of the fastest growing SI mode is shaded.

mode at their wavenumber, but the dominant mode is a surface confined mode that grows more slowly than LC. Figure 4.9 shows the fastest growing GI. The GI mode has a horizontal length scale of roughly 1 km, which is consistent with other studies of mixed layer eddies (e.g. Fox-Kemper et al., 2008), and with the GI mode in the absence of waves (not shown). The timescale (19 h) is also consistent with other linear stability and nonlinear model results.

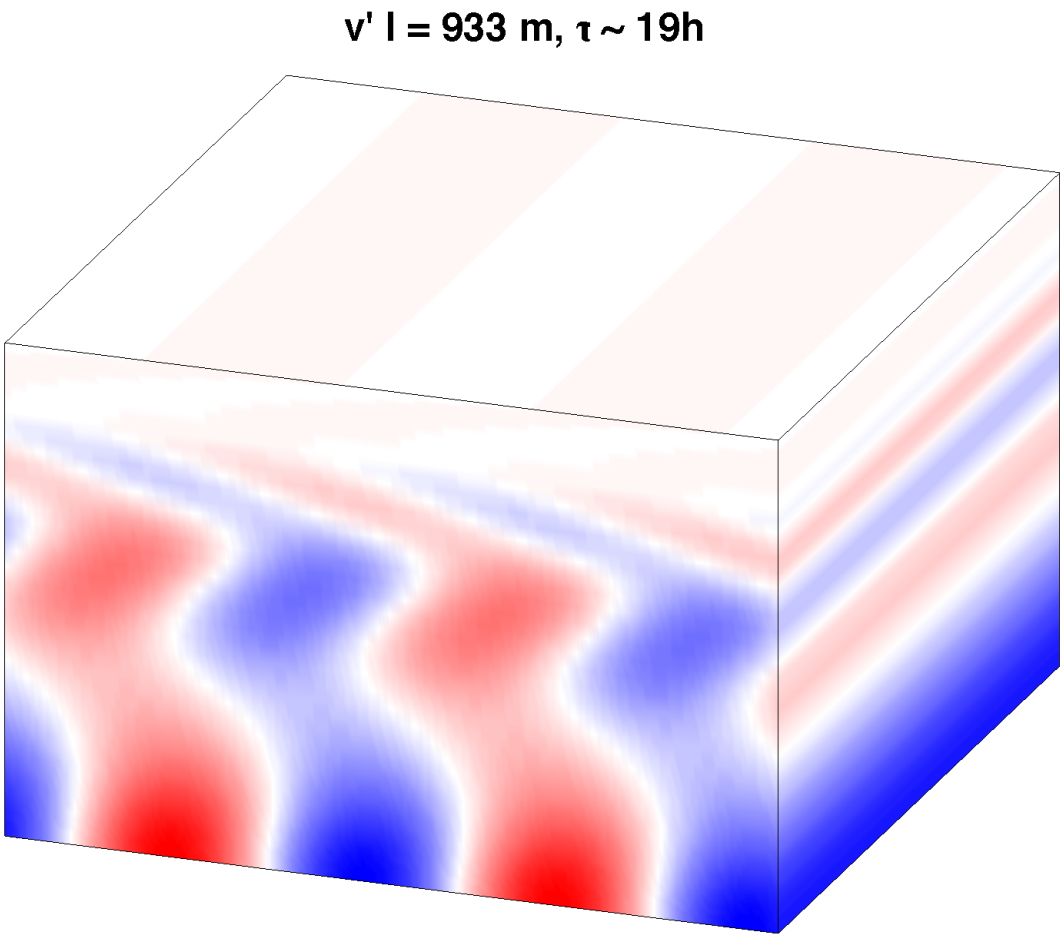

Figure 4.9: Perturbation cross front velocity (v') of the fastest growing GI mode is shaded.

4.4.1 Energetics

To understand the net effect of these instabilities on the structure of density, and shear in the mixed layer, the energy production terms are a helpful tool. As stated in chapter 1, the buoyancy production indicates how much mixing or restratification is done by the turbulent motions. The shear production is the kinetic energy extracted by the perturbation from the mean shear. In the case of SSP, this description is not quite accurate because the WAB equations used here are not coupled to a wave action equation which would allow for a small

loss of energy in the waves as the Stokes shear is converted to perturbation energy. Therefore, it is more accurate to think of the SSP as the work done on the perturbed motions by the Stokes shear force, and this force, like the imposed wind stress, is a constant, external source of energy since the Stokes drift does not evolve. The dominant energy production terms for each instability are shown in table 4.2. The energy production terms are dimensionless, and have been scaled by the dimensionless growth rate to more accurately compare the energy production of modes that grow at different rates.

Instability Type	LC	SI	GI
BP	-1×10^{-4}	0.02	0.04
ESP	5	0.09	-0.005
SSP	14	0.008	0.003

Table 4.2: Energy production terms for the three instability types.

It is clear that although the LC do mix the surface layer, the overall buoyancy production by the combination of SI and GI is far greater. However, recall that SI and GI are not active, or rather are severely Stokes modified in the Stokes layer. In fact $\overline{w'b'} < 0$, for both the SI and GI modes when only integrated over the Stokes layer, although this contribution to mixing is several orders of magnitude smaller than the LC contribution. Although the vertical structure is significantly modified by the Stokes and Ekman shears, GI exhibit the expected distribution of energy production which is dominated by BP. SI have a comparable BP rate, however this mode is still dominated by ESP as in the classical case. The shear production terms for LC completely dominate any shear production by either SI or GI in the Stokes layer. This suggests that even if the Stokes direction was opposing the geostrophic flow, in order to favor near surface PV reduction (as in the lower right panel of figure 4.2), the LC are so efficient at using that shear that the SI would not get a chance to access it. That said, since the Stokes drift is a constant source of energy (i.e. there is no feedback on the waves), if the mean flow is to remain near an Ekman-Stokes-front balance, the anti-Stokes

Eulerian shear would need to persist. If this happens, the anti-Stokes Eulerian shear would therefore provide a constant source of negative PV to favor near surface SI. However, time dependent mean flows are not addressed by the linear stability model, so we will return to this topic in the next chapter.

4.5 Discussion

It is extremely clear from the proof in section 4.1.2 with constant shear Stokes profiles, and from numerical linear stability solutions with exponentially decaying Stokes profiles that SI exist if and only if the PV is negative. Since PV only depends on the Eulerian shear, SI are most influenced by the Eulerian shear, which is altered by the Stokes shear through Lagrangian geostrophy. Furthermore, unless the flow is purely Eulerian and geostrophic, the sign of the PV cannot be determined by Ri alone, no matter what kind of shear (Eulerian or Lagrangian) is used in Ri. Therefore, the mean flow changes induced by Stokes drift can act as a switch for SI.

The changes in the mean horizontal momentum appear to affect GI and LC considerably less. The Charney-Stern-Pedlosky criteria for QG GI remain the same with the appropriate adaptations to Lagrangian shear and Lagrangian stream function (which affects the QGPV). Therefore, it is the Lagrangian shear that affects the onset of GI. When GI are present, their wavenumber and growth rate appear to be modulated by the Eulerian shear. Strong positive (negative) Eulerian shear appears to reduce (increase) the growth rate and wavenumber as suggested by Nakamura (1988). In a realistic regime, the Stokes and Ekman shears are several orders of magnitude larger than the geostrophic shear, therefore, the marginal gain in growth rate that LC gets from geostrophic shear is negligible.

The vertical momentum changes due to Stokes shear have very little effect on GI as seen by the minimal SSP. The similarity in dynamics between mixed layer GI and QG GI suggest that GI have very weak vertical velocities. The primary difference between the two forms of GI is the more dominant role of the ageostrophic components of the horizontal momentum

equation, but the vertical momentum balance remains mostly hydrostatic. Therefore, the weak vertical velocities implies that very little energy could be gained or lost due to work done by the Stokes shear force. Although the vertical momentum changes to LC through buoyancy perturbations appear small, in the realistic regime, several modes were found (not shown) to have positive BP with some mix of SSP and ESP. These mixed modes were considered to be shear instabilities due to the Ekman shear since the ESP was far larger than SSP regardless of the magnitude of the Stokes shear.

The vertical momentum changes due to the perturbation Stokes shear force have a noticeable and predictable effect on SI. Since SI work to restore the PV to zero through shear production, they must do so through ESP since it is the Eulerian shear that affects PV. Therefore, when SI are active, SSP will be positive if the Stokes shear is of the same sign as the Eulerian shear, and negative otherwise. In realistic situations where the anti-Stokes shear dominates the Eulerian shear in the surface layer, this implies that SSP will be negative near the surface. Deeper, where the Eulerian shear is dominated by the geostrophic shear, SSP will be weak (because it is deep and the Stokes shear has decayed) and positive if the Stokes and geostrophic shears are aligned, or weak and negative otherwise.

Chapter 5

Large Eddy Simulations

The previous chapters show how individual physical processes scale with different mean flow conditions, however these processes may behave very differently in the presence of each other. This interaction of motions at different scales is the very nature of turbulence. Chapters 3-4 necessarily omitted all turbulent interactions between modes because the appropriate assumptions were made in order to neglect the non-linear advection terms. In this chapter, I explore the complete, nonlinear WAB equations using Large Eddy Simulations (LES).

Since these nonlinear simulations allow for the interactions of motions on different scales, we might ask whether these scale interactions alter the dynamics that would otherwise be predicted by the results of the previous chapter. Furthermore, since the mean flow will evolve in time, several questions can be answered about the net effects of the instabilities on the larger scale flow.

(1) Is the strength of LC reduced or enhanced in the presence of SI?

(2) Is the strength of SI reduced or enhanced in the presence of LC?

(3) Do SI do more BP (than no Stokes SI modes) near the surface as predicted by the linear stability results?

(4) Is LC able to mix a shallow, near surface layer while unable to penetrate deeper as implied by the linear stability results?

(5) Is the energy production in SI dominant or LC dominant regions comparable to predictions?

Since the interactions between the Stokes modified mean flow and SI are the most substantial and robust results of the previous chapter, it is reasonable to expect that this criterion is predictive even for a nonlinear flow. Therefore, several cases of Stokes drift and front alignment are considered, and there effects on PV and SI induced SSP are summarized in table 5.1. This serves as a guide for predictions of SI in the different LES cases.

Front	$Ri^g \equiv \frac{Ri}{\gamma^2}$	θ	Stokes Layer	Deep Mixed Layer
F1	0.5	0	No SI	SI, $SSP > 0$
F2	0.5	π	Strong SI, $SSP < 0$	SI, $SSP < 0$
F1	2	0	No SI	No SI
F2	2	π	SI, $SSP < 0$	No SI

Table 5.1: The presence of SI is shown depending on the strength of the front and its alignment with the Stokes drift. Realistic assumptions about the non-dimensional parameters are made. $\mu\lambda > \gamma$, implies that the Stokes and anti-Stokes shears dominate the geostrophic shear at the surface. $\mu\lambda e^{-\lambda} < \gamma$, implies that the Stokes depth is sufficiently shallow that the geostrophic shear dominates somewhere above the pycnocline (i.e. the geostrophic shear is relevant for PV in the deep mixed layer). In this sense, the deep mixed layer is defined as the layer below z_d where z_d is defined by $\mu\lambda e^{\lambda z_d} = \gamma$. Since the LES runs will each contain two fronts, the fronts are labeled F1 and F2 with F1 always containing aligned Stokes and geostrophic shears (see figure 5.2).

5.1 Model Description and Setup

In previous work I helped perform LES of LC in misaligned wind-wave scenarios (Van Roekel et al., 2012). This gave me familiarity with the National Center for Atmospheric Research (NCAR) LES model (Moeng, 1984; Sullivan and Patton, 2011), which I have now used to complement the linear stability analysis of the previous chapters. Horizontal derivatives in this model are computed pseudo-spectrally, and vertical derivatives are solved with a second order finite difference scheme. This model is thoroughly described in

McWilliams et al. (1997) where Stokes drift was added, allowing the model to solve the WAB equations.

I chose to setup the model to be most similar to the scenario in figure 4.2 to test the PV criteria. Since the horizontal derivatives in the code are pseudo-spectral, periodic side boundaries are required. This necessitates simulating two fronts. These fronts will be referred to throughout this chapter as F1 (in the center of all cross section images) and F2 (a single front that wraps around both sides of all cross section images; see figure 5.2). The domain is intentionally restricted in the along front direction so as not to allow the development of GI. As GI reach finite amplitude they become MLE's which can grow to several km in diameter. To resolve the small horizontal and vertical scales required to retain the LC dynamics and contain MLE's within the domain, the computational cost becomes prohibitive (e.g. Hamlington et al., 2014, $O(10^6)$ cpu hours). As such, here I choose to focus on interactions between SI and LC, with a wide, but short front. The computational cost, $O(10^4)$ cpu hours, is reasonable enough to run a few different cases. Here I will focus three cases: a control case without Stokes, and cases that mimic the two background states in figure 4.2.

The buoyancy profile is specified piecewise continuously with smoothing at the transitions. The fronts are given constant stratification in the horizontal and vertical in order to tightly control Ri. Hyperbolic tangent profiles for the horizontal component of the buoyancy such as what was used in Hamlington et al. (2014) did not allow for a sufficiently wide frontal region with a tightly constrained Ri. Therefore, here, fronts are connected with "turnaround points", sections that smoothly transition from one constant buoyancy gradient to the opposite. The initial geostrophic velocity is then given by the thermal wind relation, $\overline{U}_z|_{t=0} = -\frac{\overline{B}_y|_{t=0}}{f}$. A monochromatic Stokes drift just as in chapter 4 is chosen with the strength of the Stokes shear depending on the case. The anti-Stokes Eulerian flow is subtracted from the geostrophic flow to give the Eulerian flow that the model evolves. The horizontal velocity (both u and v) is then given a small amplitude, random (white

noise) perturbation. In addition to the two front buoyancy structure, a strongly stratified ($N^2_{pyc} = 10^{-4}$) pycnocline is used at $\sim 50\ m$ deep to create a more realistic mixed layer than in the linear stability analysis (which had a simple rigid, no slip bottom boundary).

In the two cases with Stokes drift, the near surface PV is negative where the Stokes drift opposes the geostrophic shear and positive where they are aligned. In the case with higher vertical stratification ($Ri = 2$), the PV is positive at depth, and in the case with lower vertical stratification ($Ri = 0.5$) the PV at depth is negative (as in the control case; figure 5.2). The initial Eulerian velocity structure for each case is shown in figure 5.1. Note that near the surface in the Stokes cases, the Eulerian velocity in the central front is slightly weaker (in amplitude) than in the other front because the geostrophic flow opposes the anti-Stokes Eulerian flow in the central front (F1). The two separate frontal regions denoted F1 and F2, which will be referred to throughout the rest of this chapter, are indicated in figure 5.2.

The boundary conditions are no stress and no flux at the surface and bottom. There is no surface wind stress applied in order to emulate a swell only, rather than locally generated wind wave conditions. Several of the model parameters are given in table 5.2.

Computation Grid, N_x, N_y, N_z	$128 \times 2048 \times 72$		
Physical Domain Size, L_x, L_y, H	$500m \times 8km \times -75m$		$500m \times 8km \times -70m$
Grid Resolution, Δx, Δy, Δz	$3.9\ m \times 3.9\ m \times 1\ m$		$3.9\ m \times 3.9\ m \times 1\ m$
Horizontal Stratification, M^2	$7.0 \times 10^{-8} s^{-2}$		
Mixed Layer Stratification, N^2	$3.5 \times 10^{-7} s^{-2}$		$1.4 \times 10^{-6} s^{-2}$
Pycnocline Stratification, N^2_{pyc}	$10^{-4} s^{-2}$		
Deep Stratification, N^2_{deep}	$4N^2$		
Latitude	$35°N$		
Coriolis Frequency	$8.3 \times 10^{-5}\ s^{-1}$		
Mixed Layer Depth, H	$50\ m$		
Wind Stress, τ	$0\ Nm^{-2}$		
Surface Stokes Drift, U_0^S	$0\ ms^{-1}$	$0.083\ ms^{-1}$	$0.042\ ms^{-1}$
Stokes Drift e-folding Depth, H^S	$10\ m$		
Dimensionless Parameters			
Richardson Number, Ri	0.5	0.5	2
Stokes Shear, $\mu\lambda$	0	10	5
Geostrophic Shear, γ	1	1	1
Stokes Depth, λ	5		

Table 5.2: The physical parameters of the LES.

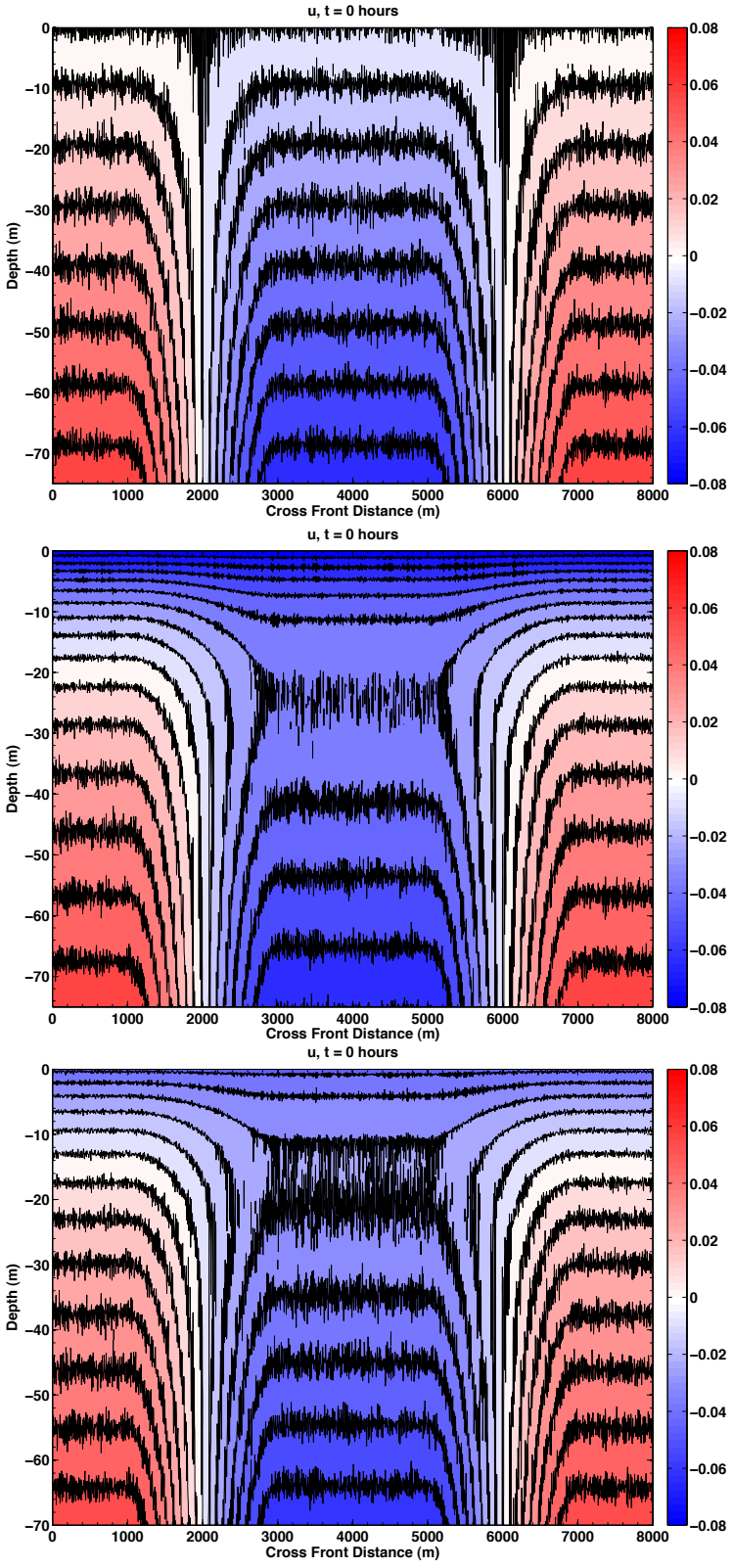

Figure 5.1: The initial along front, Eulerian velocity structure is shaded and contoured. The high frequency oscillations are due to the initial random white noise imposed on top of the mean flow. (top) $Ri = 0.5,\ \mu = 0$. (middle) $Ri = 0.5,\ \mu = 2$. (bottom) $Ri = 2,\ \mu = 1$.

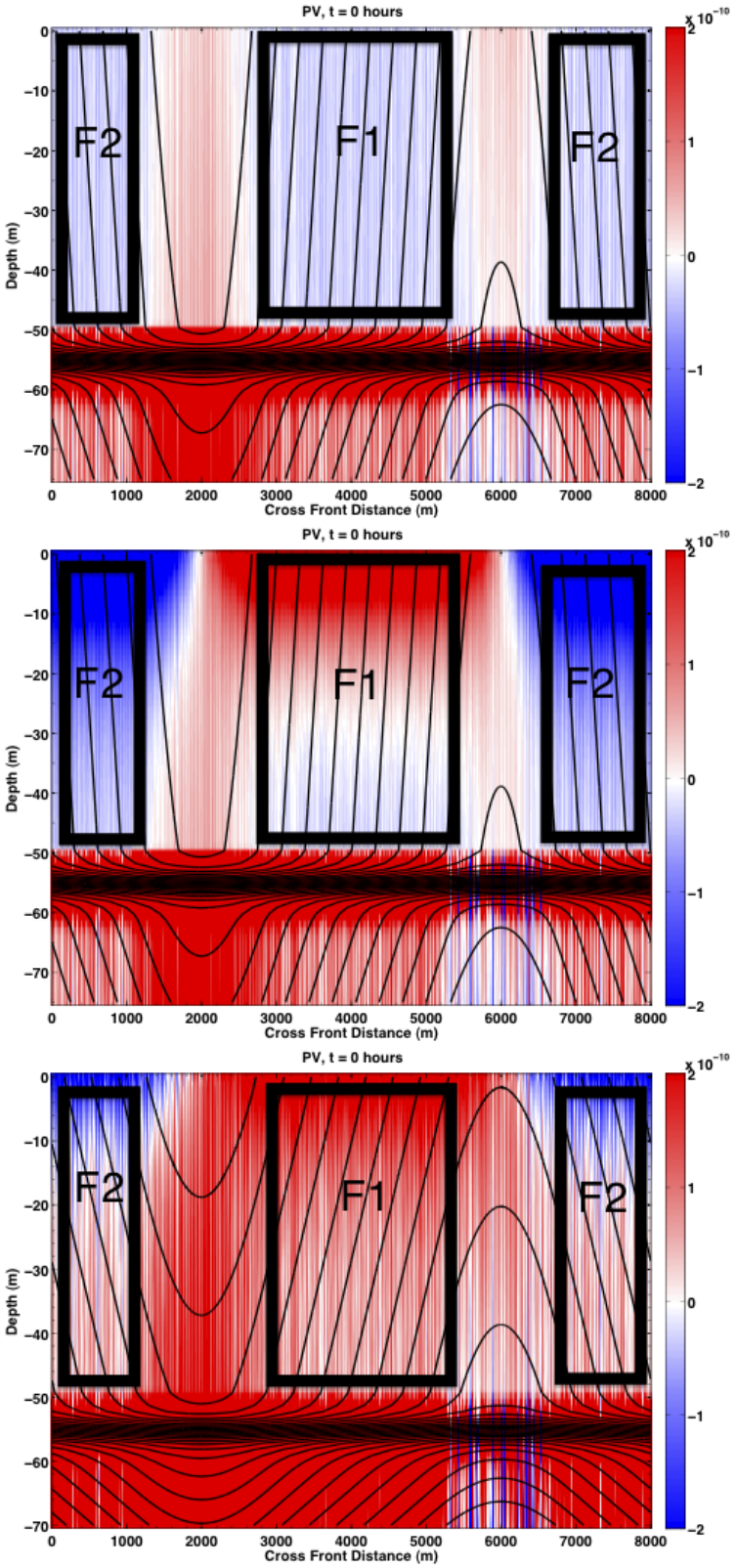

Figure 5.2: The initial PV structure is shaded. The black contours show the initial buoyancy structure. Black boxes indicate the two fronts which are referred to as F1 and F2. (top) $Ri = 0.5,\ \mu = 0$. (middle) $Ri = 0.5,\ \mu = 2$. (bottom) $Ri = 2,\ \mu = 1$.

5.2 Ekman Layer Development

Since the model was initialized without wind stress, one might expect there not to be an Ekman layer, however one develops quite quickly. This is due to the fact that the initial mean flow applies a stress to the surface, which is unmatched by the wind, or lack thereof, which pins the surface shear to be zero. This stress is due partially to the anti-Stokes Eulerian flow and partially to the geostrophic stress, and therefore an Ekman flow develops to balance this stress. This is exactly analogous to the frontal spindown described by Thomas and Rhines (2002); Thomas and Ferrari (2008), except in their cases, the applied surface stress was due to the geostrophic stress only. The total Eulerian velocity is then a combination of Ekman, geostrophic, and anti-Stokes flows.

$$\overline{U} + i\overline{V} = \underbrace{\frac{1}{(1+i)\eta}\left[\hat{\tau}e^{i\theta^e} - \gamma - \frac{2i\lambda\mu e^{i\theta}}{(\frac{\lambda}{\eta})^2 - 2i}\right]e^{(1+i)\eta z}}_{Ekman} + \underbrace{\gamma z}_{front} + \underbrace{\frac{2i\mu e^{i\theta}}{(\frac{\lambda}{\eta})^2 - 2i}e^{\lambda z}}_{Stokes} \tag{5.1}$$

Once the Ekman flow has developed (about one inertial period, $\sim 21\ h$ at 35° N), the laminar, analytic, solution for the Ekman-Stokes-Front layer (equation 5.1) is a good approximation to the horizontally averaged flow in the LES (figure 5.3). To obtain a similar Ekman spiral the Ekman depth (H^E) was tuned, and the along front averaged horizontal buoyancy gradient was used to compute the geostrophic component for the analytic solution. McWilliams et al. (2014) showed this similarity between the analytic solution and the LES in their cases in which fronts were absent (i.e. $\gamma = 0$). Furthermore, McWilliams et al. (2014) note that the steady state solution for the Stokes Ekman layer must conserve the Lagrangian Ekman transport, i.e. the Ekman transport (the vertically integrated Ekman flow) is the same with and without Stokes drift. This means that the front is either stabilized or destabilized by the Lagrangian transport (this is also clear from the buoyancy conservation equation 3.2). The good agreement between the laminar and turbulent solutions suggests that the linear solutions in chapter 4 were forced appropriately with this mean flow. Furthermore, as the right panel of figure 5.3 shows, that forcing is fairly steady and so remains a source of kinetic

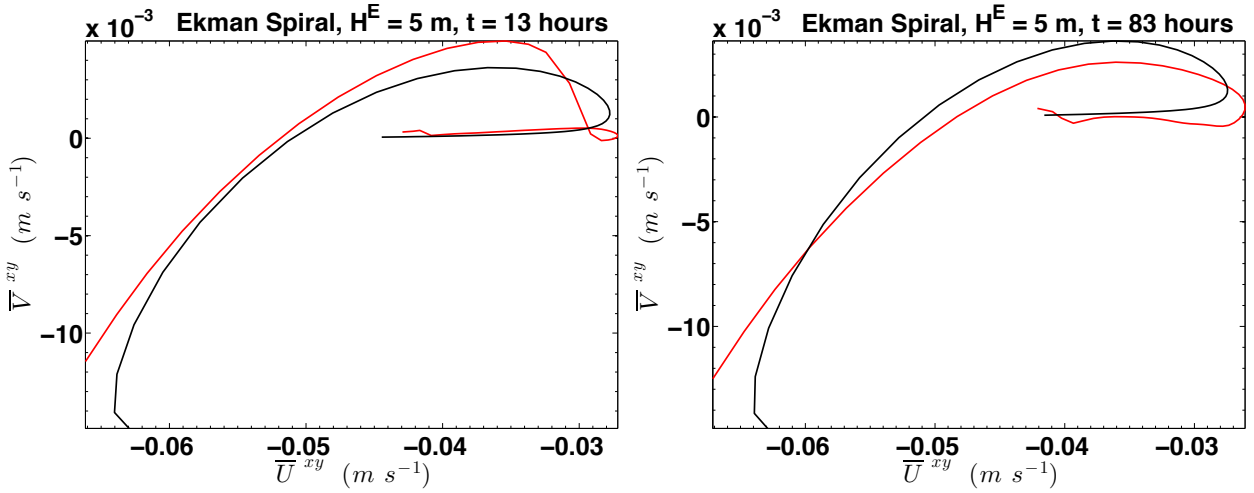

Figure 5.3: Hodographs of the Eulerian velocity from the $Ri = 0.5,\ \mu = 2$ case (red), and as computed from equation 4.26 (black), utilizing the geostrophic shear and the estimated Ekman depth at the respective model time step. The bottom of the layer is where $\overline{V}^{xy} = 0$. An early time (13h), prior to much turbulent activity is shown (left) and later time (83h) when the turbulence has become more substantial is shown (right).

energy even after substantial turbulent interactions are occurring.

5.2.1 Frictional PV Injection from Stokes Drift

As is evident in figure 5.3, the Ekman spiral is maintained for long periods of time despite not being forced by winds. In the spin down problem discussed by Thomas and Ferrari (2008), this would not be the case since the Ekman layer there is driven by the geostrophic stress, which evolves as the Ekman flow stabilizes or destabilizes it through the Ekman buoyancy flux. When the anti-Stokes Eulerian shear is the primary driver of the Ekman layer, this spin down will not occur because the Stokes Coriolis force is an external force that is unperturbed by the flow. The stationary flow described by the Ekman-Stokes-Front layer will indeed match the no stress condition right at the boundary, however, this Eulerian flow is sheared just below that, and the source of this shear is external, and so cannot be dissipated (i.e. spun down).

This scenario is analogous to a constant wind, which induces FSI when the winds blow

down front. The wind induces a destabilizing Ekman transport and and increased vertical shear aligned with the geostrophic shear, both which reduce the PV in the front. The Stokes drift effectively injects PV in a similar manner. The Stokes drift remains unperturbed because the flow does not feed back onto the waves, so the Stokes Coriolis force is constantly inducing an anti-Stokes Eulerian flow. This anti-Stokes flow injects PV if the Stokes drift is down front, aligning the anti-Stokes against the geostrophic shear. The anti-Stokes flow extracts PV if the alignment is opposite.

5.3 Phenomenology of the Ensuing Turbulence

Once the Ekman layer develops, turbulent motions of many varieties appear. Here I will focus on the turbulent motions that are characteristic of the instabilities discussed in the previous chapter (i.e. SI, LC, KHI).

The control case shows SI, which is exactly what one expects from a geostrophically balanced front with negative PV. The characteristic along isopycnal motions of SI (figure 5.4) take about one day to form. This is roughly 3-9 e-folding times for the growth of the linear mode. The horizontal scale of the SI ($\sim 200\ m$) is very close to the SI mode in the linear stability calculations ($\sim 160\ m$). The SI restore the initially negative PV to zero by entraining high PV water from the pycnocline (figure 5.5). Since the surface stress in this case is only due to geostrophic stress, the surface PV flux is extremely weak, but negative (downward; PV into the ocean), although this PV source is not substantial.

The two cases with Stokes also show signs of SI as well in the negative PV regions, although somewhat weaker than in the no Stokes case. The $Ri = 2, \mu = 1$ case shows weak SI near the surface in F2, where the PV is negative (figures 5.6-5.7). A common visual indicator of LC is strong vertical velocity fluctuations on scales of $10 - 500\ m$. Recall that LC are counter rotating cells with horizontal vorticity. This means that near the surface, the flow forms lines of convergence (where one would see windrows of floating debris) and divergence which forces strong negative and positive vertical velocities respectively. There is

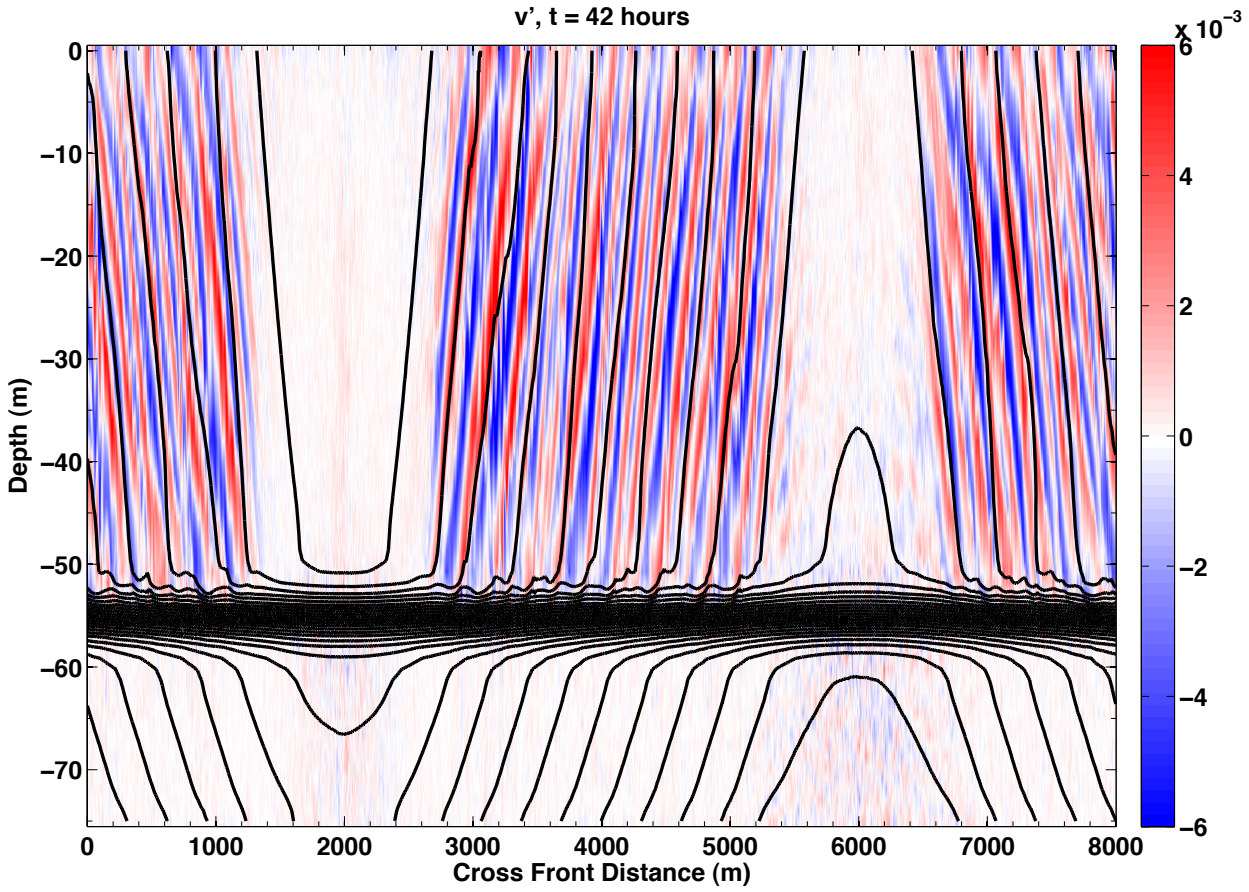

Figure 5.4: Turbulent cross-front velocity (v') is shaded for the $Ri = 0.5,\ \mu = 0$ (no Stokes) case. The black contours are along front averaged isopycnals.

effectively no LC in this region (figure 5.8). This is partially because the Stokes drift opposes the geostrophic shear here. This anti-alignment also means that the resulting Ekman flow acts to restratify the front, therefore suppressing LC. At depth, F2 has positive PV, and is therefore, comparatively quiescent. On the other hand, F1 shows signs of weak LC (figure 5.8), but no SI due to the positive PV throughout F1 (figures 5.6-5.7). F1 is more favorable for LC because the Ekman flow destabilizes the front.

The $Ri = 0.5,\ \mu = 2$ case shows very strong SI in F2, and considerably weaker SI in the deep part of F1 (figure 5.9). This is because the SI exchange low PV water for high PV water from the pycnocline, but in F2, there is effectively an infinite source of Eulerian

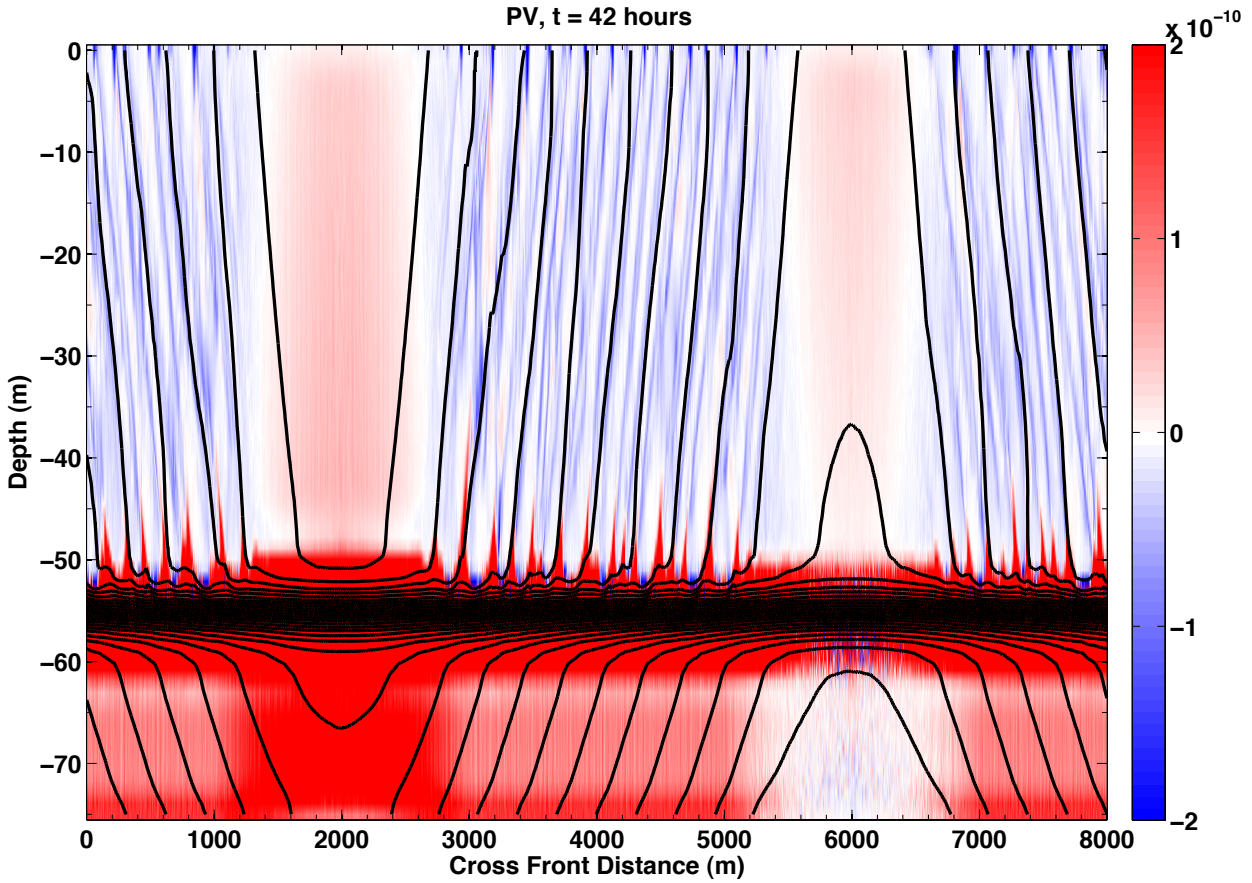

Figure 5.5: PV is shaded for the $Ri = 0.5,\ \mu = 0$ (no Stokes) case. The black contours are along-front averaged isopycnals.

shear, and a very strong source of negative PV (because the anti-Stokes flow is an external PV source). This PV source strengthens SI throughout F2 as they attempt to restore the PV of the Stokes layer to zero (see the excursions of positive PV into the Stokes layer in figure 5.10). SI are notably absent from the near surface region of F1, which is consistent with positive PV, however, other criteria based on Ri would have failed to predict this. SI are not the dominant feature of the turbulence near the surface, even in F2 where the PV is strongly negative. LC dominate the turbulence near the surface in F2 (figure 5.11). In F1, the near surface turbulence is eventually LC-like, however initially it appears to be a mixed convective-shear instability. Figure 5.12 shows rolls with their vorticity aligned with the

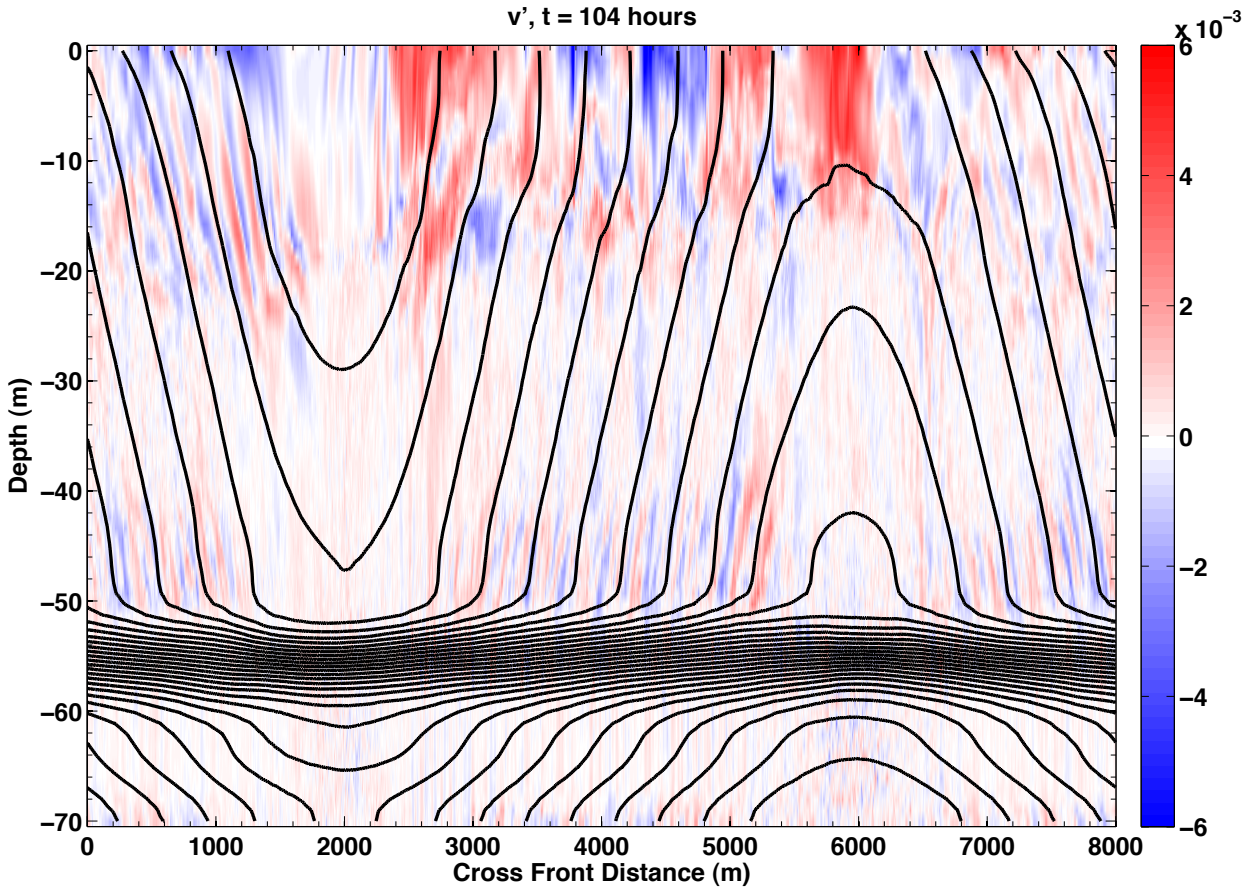

Figure 5.6: Turbulent cross front velocity (v') is shaded for the $Ri = 2,\ \mu = 1$ case. The black contours are along front averaged isopycnals.

mean horizontal vorticity. After roughly one day, these begin to transition to wide LC-type instabilities (figure 5.12).

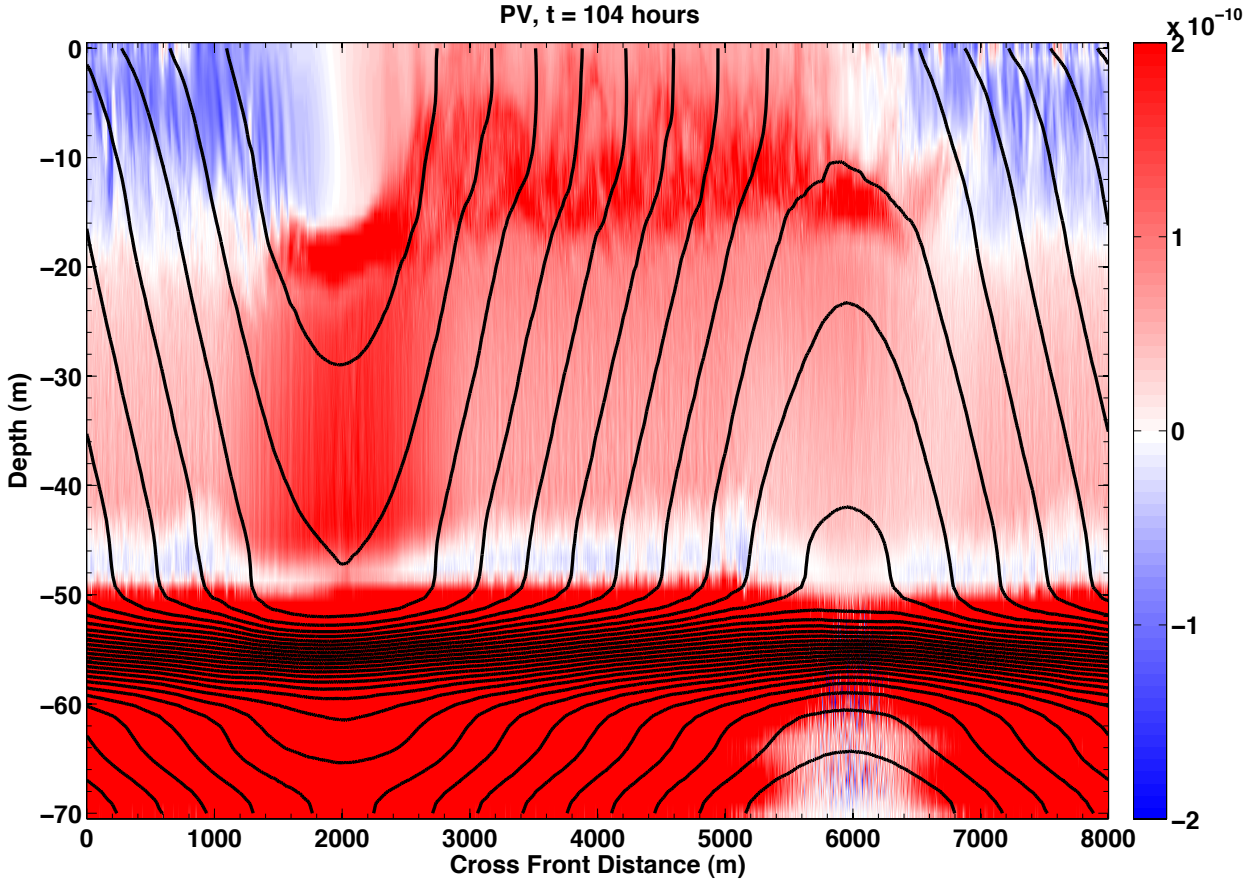

Figure 5.7: PV is shaded for the $Ri = 2,\ \mu = 1$ case. The black contours are along front averaged isopycnals.

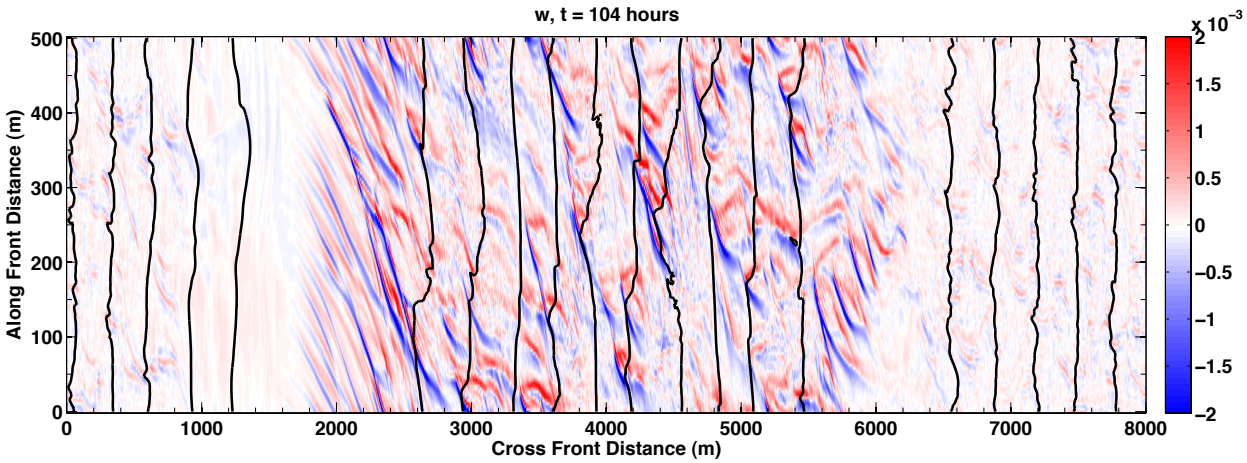

Figure 5.8: Vertical velocity (w) at $\approx 5\ m$ is shaded for the $Ri = 2,\ \mu = 1$ case. The black contours are isopycnals. Strong, alternating vertical velocities on scales of $10 - 500\ m$ indicate LC.

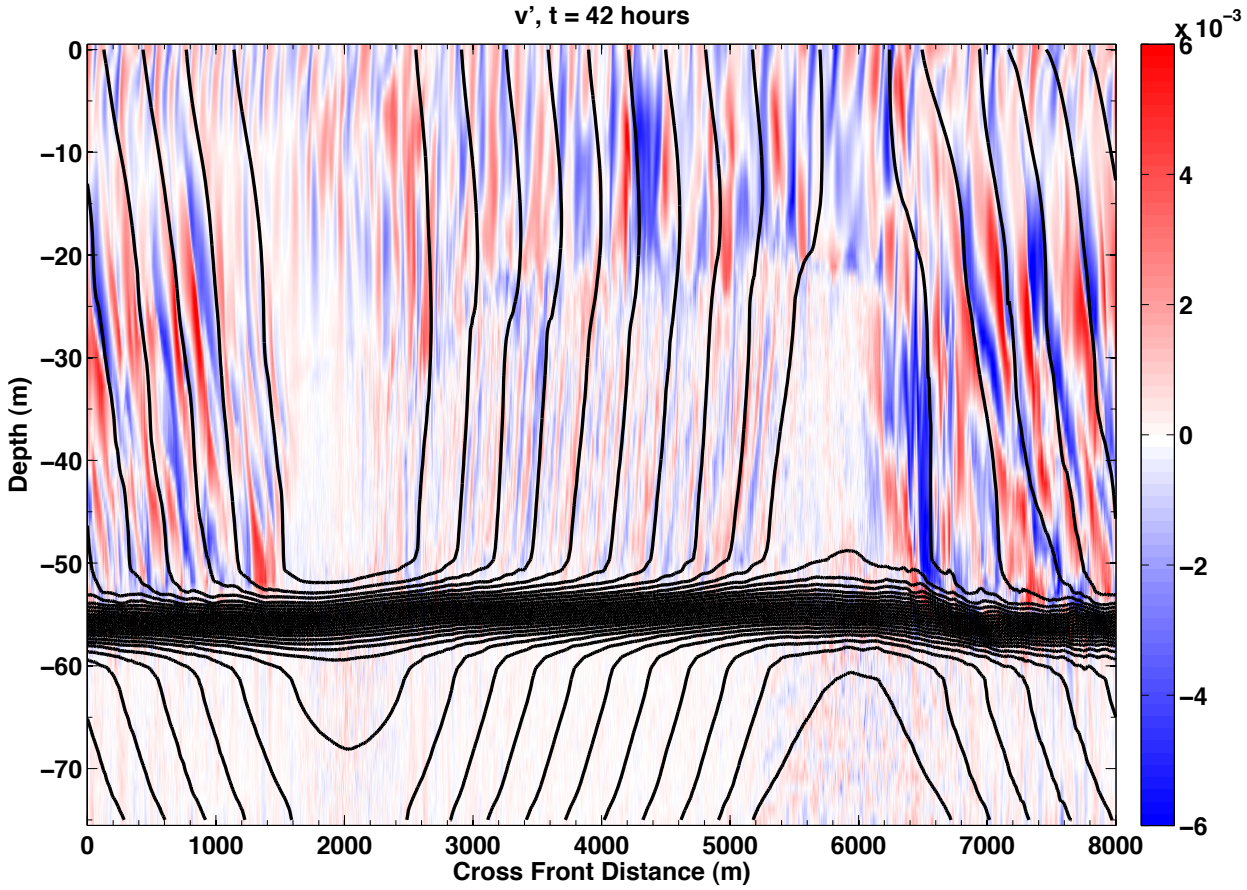

Figure 5.9: Turbulent cross front velocity (v') is shaded for the $Ri = 0.5,\ \mu = 2$ case. The black contours are along front averaged isopycnals.

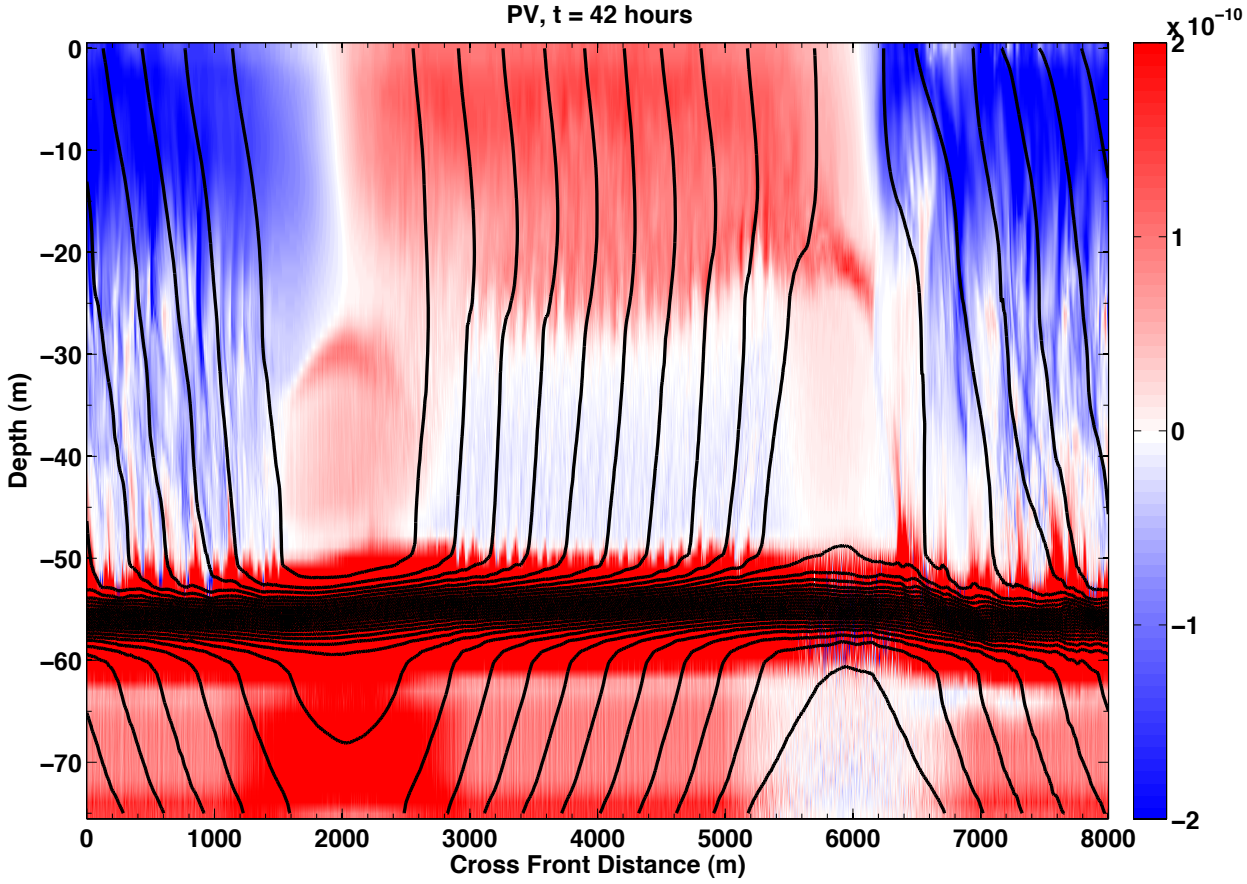

Figure 5.10: PV is shaded for the $Ri = 0.5,\ \mu = 2$ case. The black contours are along front averaged isopycnals.

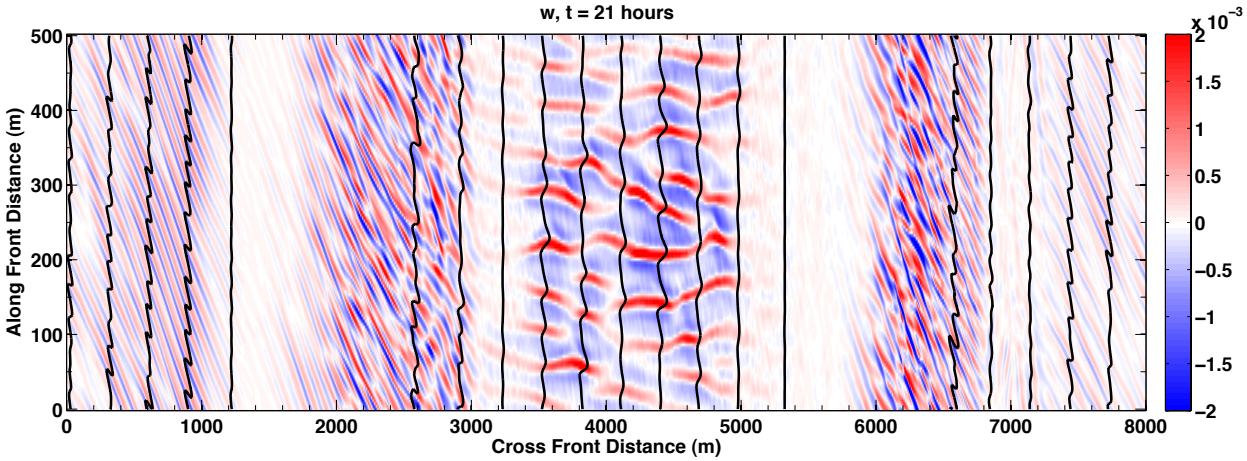

Figure 5.11: Vertical velocity (w) at $\approx 5\ m$ is shaded for the $Ri = 0.5,\ \mu = 2$ case. The black contours are isopycnals. Strong, alternating vertical velocities on scales of $10 - 500\ m$ indicate LC.

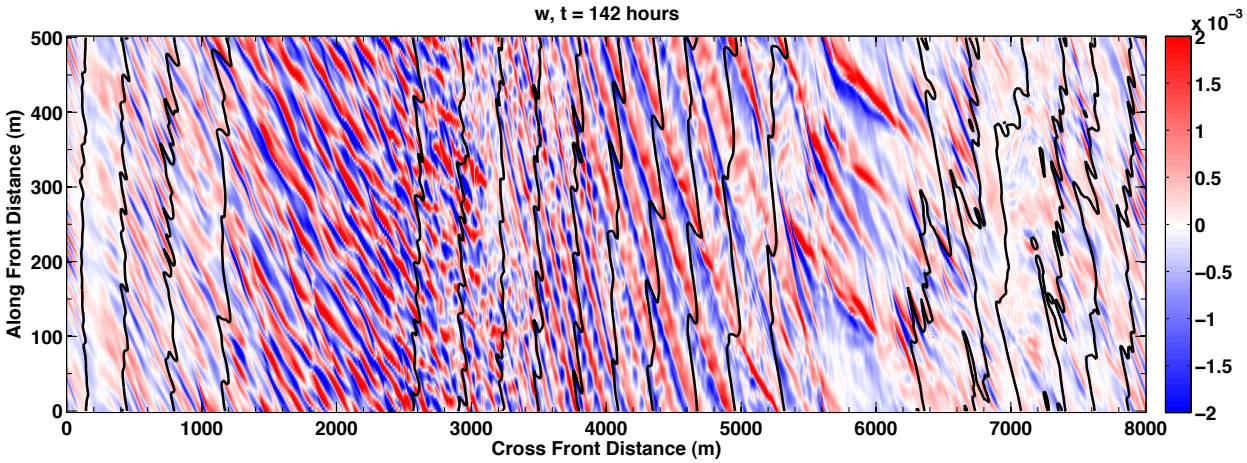

Figure 5.12: Vertical velocity (w) at $\approx 5\ m$ is shaded for the $Ri = 0.5,\ \mu = 2$ case. The black contours isopycnals. Strong, alternating vertical velocities on scales of $10 - 500\ m$ indicate LC.

These features indicate that even in nonlinear flows, the Stokes modified PV criteria (sections 4.1.2-4.2) for the onset of SI holds. Furthermore, since the wave forcing is an external source in this setup, the Stokes modified PV is an infinite source of Eulerian shear and a large reservoir of negative PV (for F2) which allows SI to grow substantially stronger than when the PV is only initially negative. One would expect this strengthening of SI to have a very strong impact on the reorganizing of the mean shear. This will be explored in the following section on the Energetics of the flow.

5.4 Energetics

Just as in chapter 4, the energy production terms are a useful tool in understanding what kind of turbulent kinetic energy (TKE) is produced by what energy source. Typically energy budgets are computed by averaging over a domain which has no net energy flux so as to conclude that the energy production is caused by the turbulent motions within the domain rather than an energy flux into the domain. This technique would work fine for energy budgets of the entire domain, however the previous section showed that the features of the two fronts, F1 and F2, are quite different, so I intentionally avoid averaging over them. Therefore averages within each front are performed to capture the differences in energy production that are so clear from the velocity and PV structures seen in the previous section. The result of averaging only within each front is that the buoyancy production term is not very useful as it is particularly contaminated with large fluctuations due to internal waves and interactions between fronts. Therefore, in place of the buoyancy production we will look at the average stratification for each front (a measure of the work done by buoyancy production) and the evolution of PV.

In the no waves case ($Ri = 0.5,\ \mu = 0$), we see what we expect, large ESP throughout the mixed layer (figure 5.13). The volume integrated stratification slowly increases which is evidence that the are not only extracting kinetic energy from the Eulerian shear, but also potential energy from the front. The PV begins to be restored to zero coincident with the

peak ESP, and therefore, the onset of SI. Note that the snapshot of SI at 42 h in figures 5.4-5.5 is shortly after the peak in ESP. As time progresses, the ESP is weakened as the SI increase the PV and reduce the available kinetic energy in the front. The SI clearly do some BP since the stratification increases quickly, and uniformly throughout the layer coincident with the high ESP. This classic SI case, which has been studied by many others (e.g. Taylor and Ferrari, 2009, 2010) serves as a control case to demonstrate that a front unperturbed by Stokes drift acts exactly as has been seen in previous numerical studies, and quite similarly to what has been shown by analytical, linear theory.

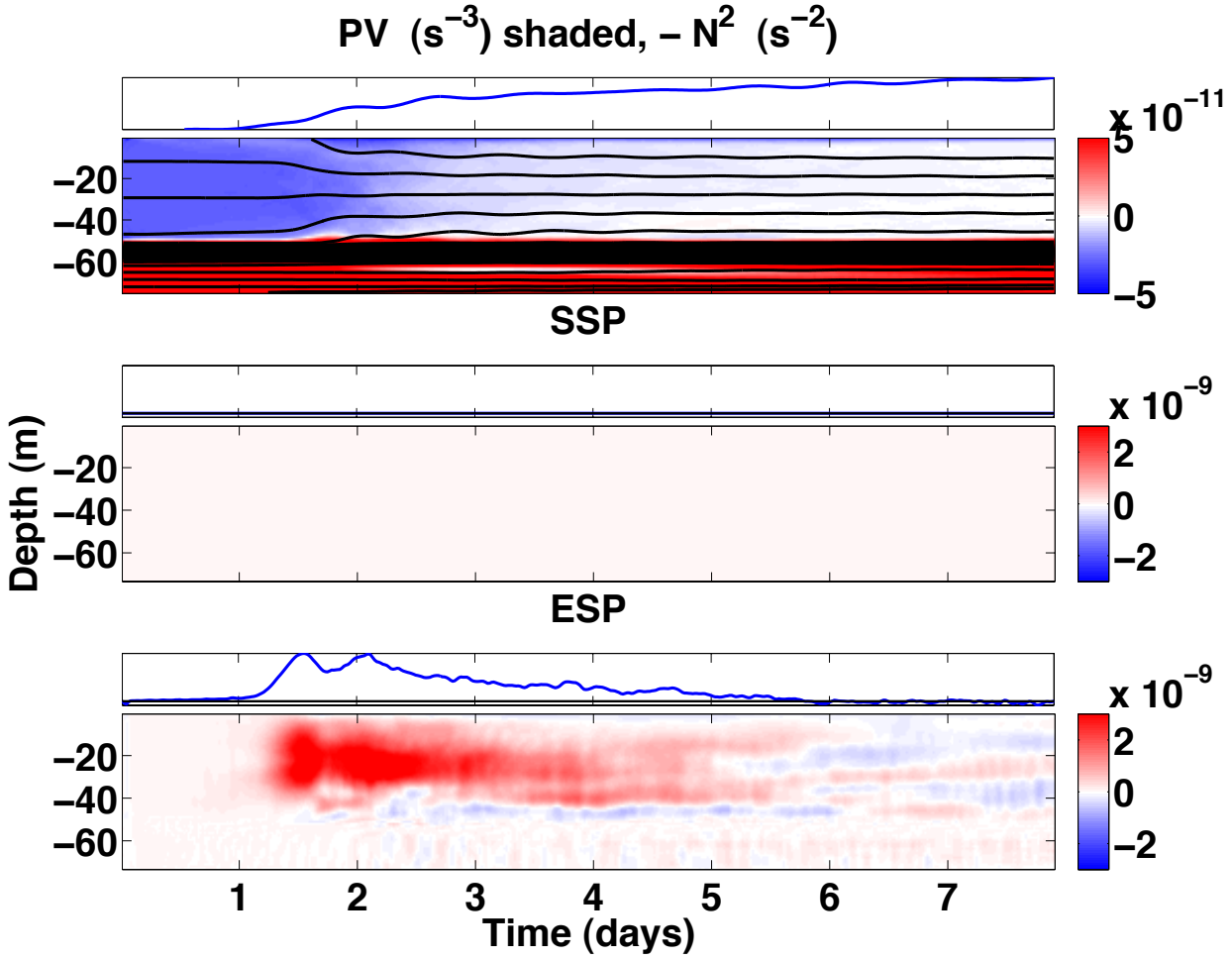

Figure 5.13: (top) A Hovmöller plot of horizontally integrated (within F2) PV is shaded. Black contours are buoyancy. The line plot above shows the volume integrated (within F2) buoyancy gradient, N^2, with time. (middle and bottom) Energy production sources are plotted (volume integrated) and shaded (horizontally integrated) vs time for the no Stokes ($Ri = 0.5,\ \mu = 0$) run. $SSP = \overline{u'w'}U_z^S$ is the Stokes shear production, or equivalently, the work done by the Stoke shear force on vertical motions. $ESP = \overline{u'w'}\overline{U}_z + \overline{v'w'}\overline{V}_z$ is the Eulerian shear production. Here only F2 is shown, but the results are similar for F1. The energy production terms have units of $m^2\ s^{-3}$.

The $Ri = 2,\ \mu = 1$ case is quite different. First, F1 is somewhat simpler in that the PV is positive throughout the layer. There is no evidence of SI as expected. In all cases of F1, the Ekman transport is oriented to destabilize the front. This is seen in the volume integrated reduction of N^2. Furthermore, the development of the Ekman Layer can be seen in the PV as a strongly positive ribbon of PV descends from the surface during the Ekman layer development. This, in conjunction with the overall decrease in vertical stratification, suggests that the PV dynamics are most significantly effected by the strong anti-Stokes Eulerian shear rather than the reduced vertical stratification (which would reduce the PV). The onset of strong SSP occurs after about a day. The ESP also develops at the same time, but remains very weak throughout the run. Nevertheless, LC are present as in figure 5.8 at 104 h, which is shortly after the Ekman layer becomes fully developed.

The dynamics of F2 are significantly different. Since F2 has an oppositely oriented buoyancy gradient, the anti-Stokes Eulerian shear produces negative PV in the Stokes layer. Also since F2 is oppositely oriented, the Ekman flow restratifies the surface as shown by the volume integrated stratification. As expected by the absence of any evidence of LC in vertical velocity (figure 5.8), the SSP is zero or negative throughout the run. Although there is evidence of weak SI in cross front velocity (figure 5.6), there is very little ESP. The slightly negative SSP near the surface is another indicator of weak SI that is predicted in table 5.1. A weak effect of SI can be seen beyond 8 days where the PV is becoming homogenized near the surface.

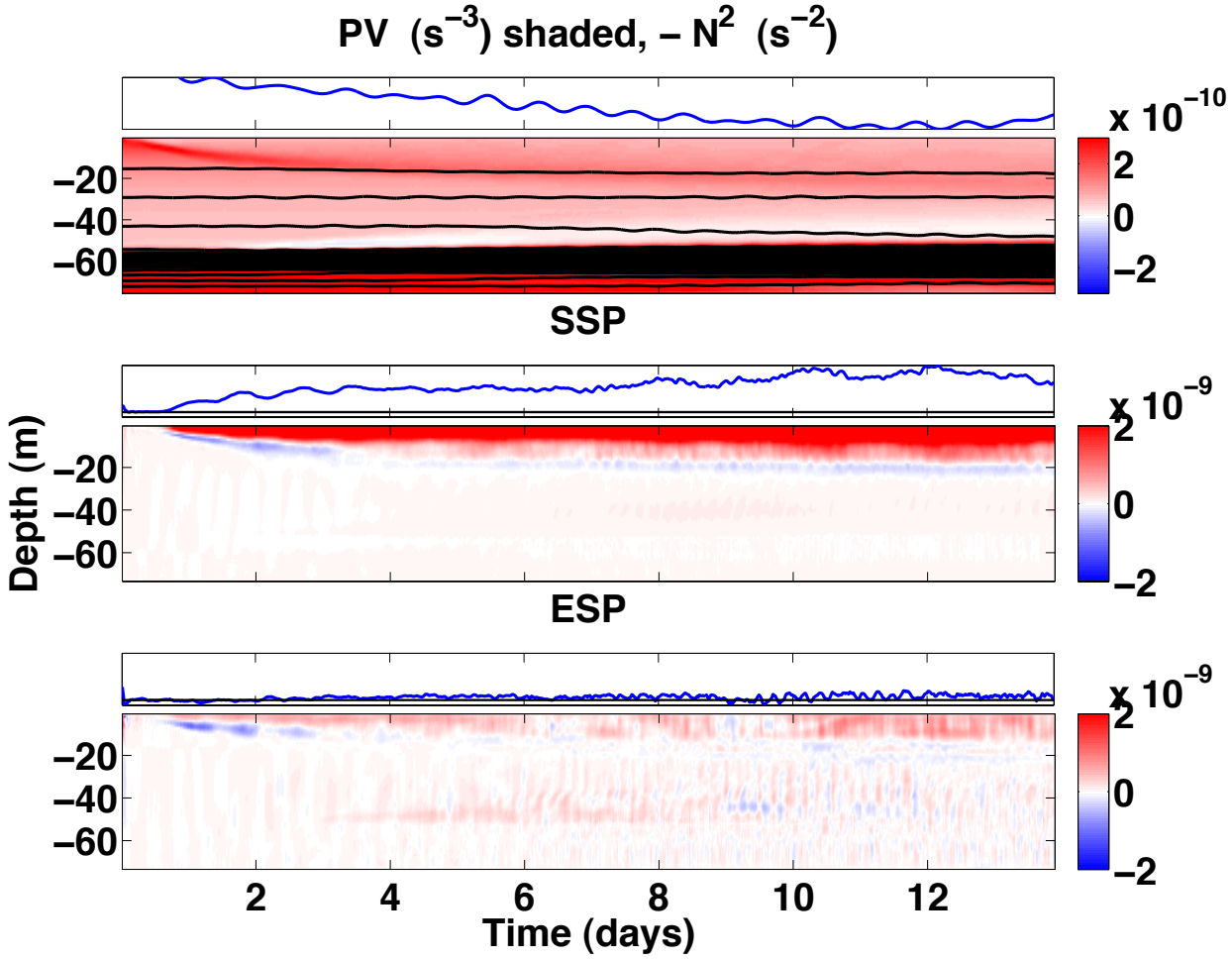

Figure 5.14: As in figure 5.13 but for $Ri = 2,\ \mu = 1$ and for F1.

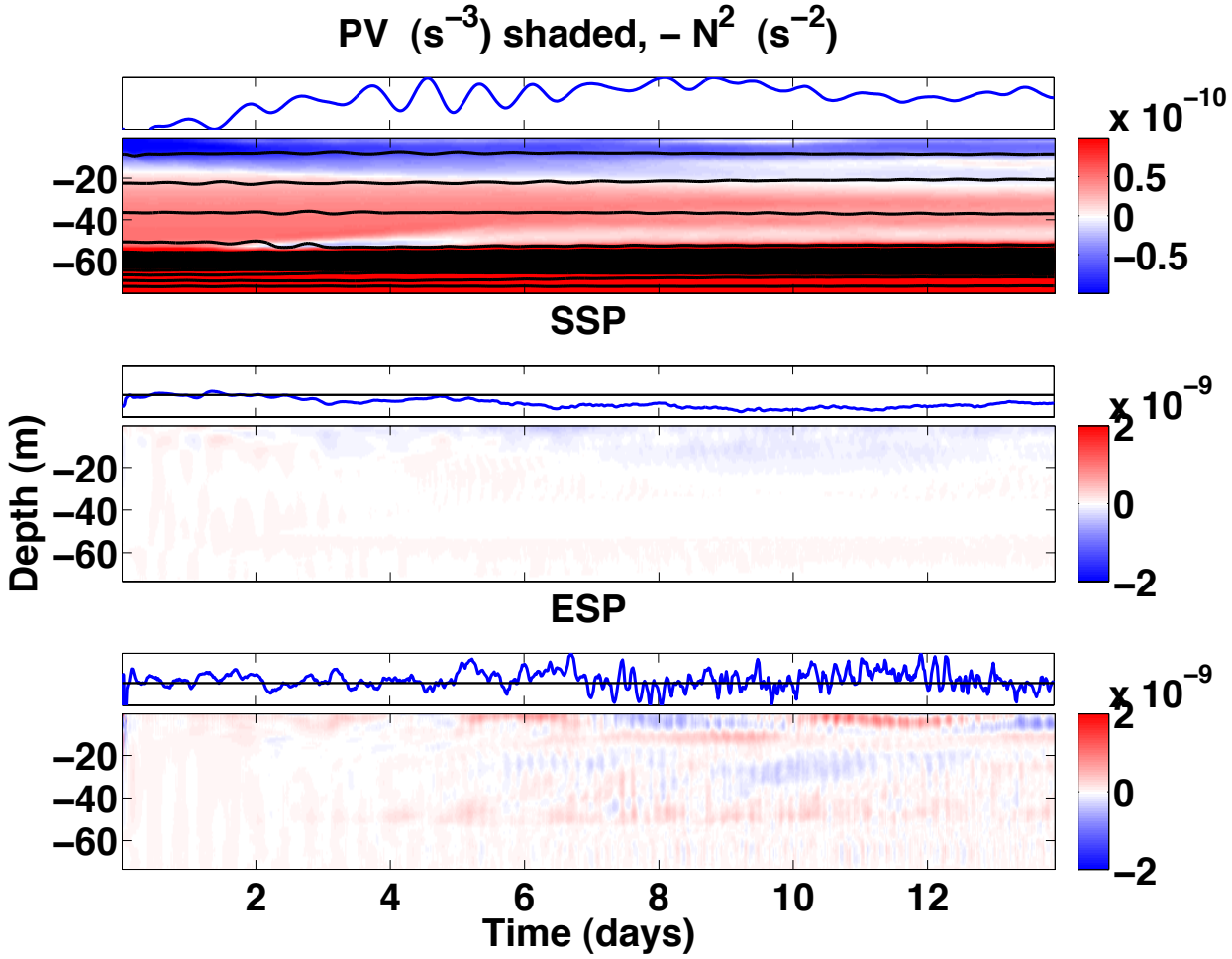

Figure 5.15: As in figure 5.13 but for $Ri = 2,\ \mu = 1$ and for F2.

The $Ri = 0.5,\ \mu = 2$ case is very energetic and showcases both SI and LC quite well. First in F1, the volume integrated stratification oscillates, but is only slightly reduced (figure 5.16 upper panel). A reduction in stratification is consistent with a destabilized front due to the Ekman flow. The PV is initially positive at the surface, and negative deeper in the mixed layer. The PV is slowly homogenized beginning within two days of the start of the run. This is consistent with weak SI seen in figure 5.9, and with the slowly increasing ESP in the deep portion of the mixed layer (figure 5.16 lower panel). There is strong SSP at the surface beginning around 18 h and persisting throughout the run. There is also strongly negative SSP just below this, which is consistent with the prediction in table 5.1. The transition from the mixed convective-shear instability to a LC-like structure in vertical velocity (figures 5.11-5.12) occurs around one day. At roughly this same time, there are significant relaxations in both SSP and ESP from previously large values. After one day, ESP remains strongly positive in the Stokes layer, and weakly positive in the deeper mixed layer.

F2 starts with negative PV throughout the layer, with very negative PV near the surface. The increase in volume integrated stratification is consistent with the alignment of the front and Ekman flow. Homogenization of the PV below the Stokes layer begins within two days indicating the onset of SI. This is also evident in the ESP with a strong increase at roughly 1.3 days. The ESP is generally positive both at depth and very near the surface, with a thin layer of near zero ESP in between. This same gap occurs with the fine scale changes in turbulent cross front velocity (v') near the surface, and larger scale changes at depth, with a layer of weak v' in between (figure 5.9). These scales are consistent with LC in the near surface, and SI below. The SSP is strongly positive at the surface throughout the run, which is consistent with the presence of LC (figure 5.11), however the SSP is strongly negative in the deep mixed layer. This suggests that the Stokes shear force does work to inhibit the SI just as predicted by table 5.1.

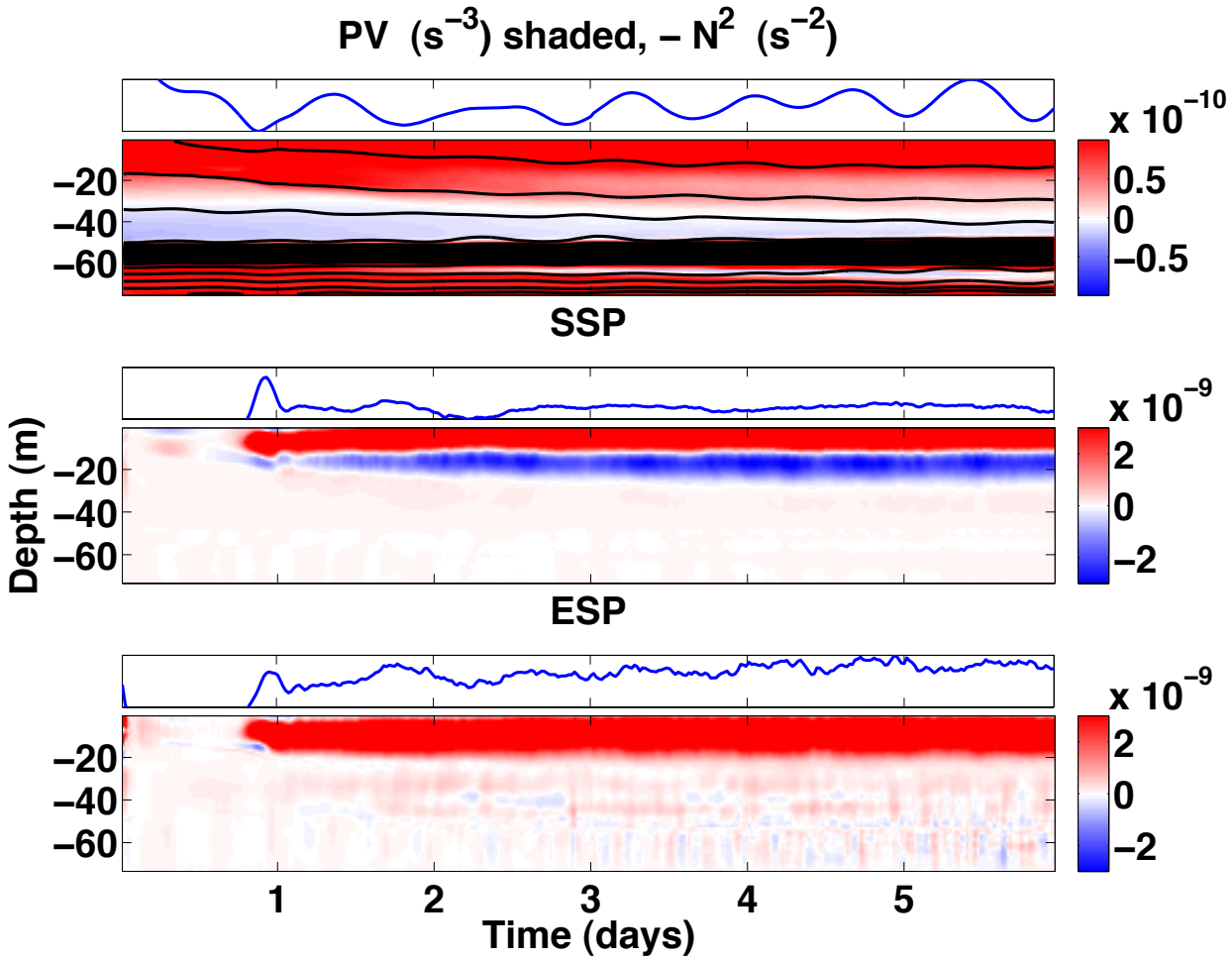

Figure 5.16: As in figure 5.13 but for $Ri = 0.5,\ \mu = 2$ and for F1.

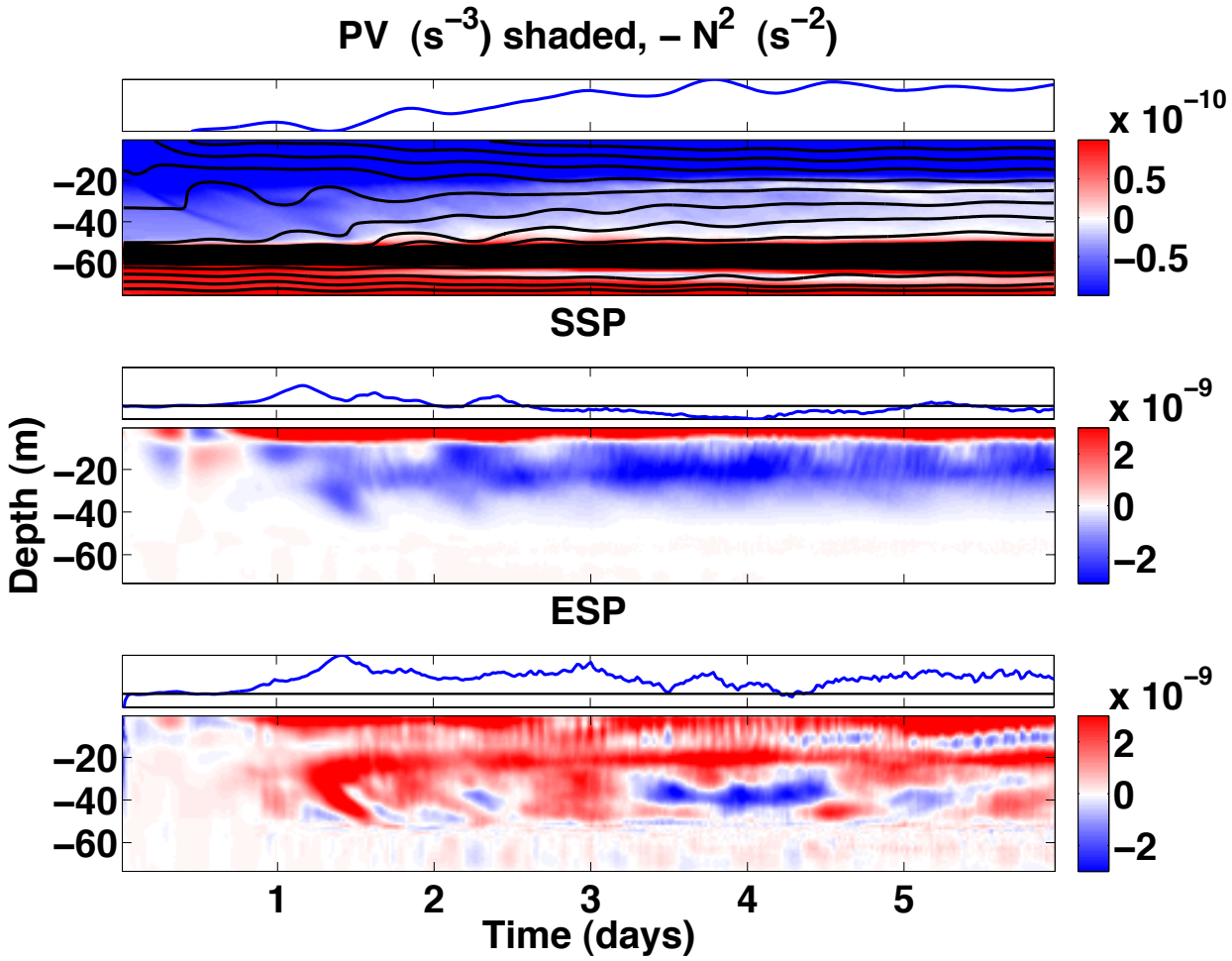

Figure 5.17: As in figure 5.13 but for $Ri = 0.5,\ \mu = 2$, and for F2.

5.4.1 Energy Spectra

The linear stability calculations of the previous chapters were necessarily lacking nonlinear interaction between modes. This nonlinear interaction is required for the transfer of energy between scales in the flow. One way to examine this interaction of scales is to look at how the energy as a function of wavenumber changes in time. Here I have computed the energy spectra as a function of cross front wavenumber for each front in each case. To compute the kinetic energy ($\frac{1}{2}\mathbf{u}\cdot\mathbf{u}$) spectra, first the domain is restricted to one of the fronts, and any linear trend in the cross front direction is removed. Then a fast Fourier transform is performed in the cross front direction for each velocity component at each depth and along front position. The spectral velocity components are summed to form the kinetic energy, and then averaged over the along front position and depth.

First, the control case ($Ri = 0.5,\ \mu = 0$) shows a strongly peaked spectrum after one day (figure 5.18). The peak is near a wavelength of 200 m in F1 and 160 m in F2, which is nearly the linear stability prediction for the size of SI ($\sim$ 160 m). Then energy from SI cascades to larger scales, although a substantial bump at higher wavenumbers persists through day two. After three days have passed, there is no longer a notable peak at the SI length scale, and by the end of the run, the energy at all scales has subsided somewhat. The loss of the peak at the SI length scale, and reduction in total kinetic energy after three days is consistent with the restoration of PV back to nearly zero, and the reduction in ESP shown in figure 5.13. It is clear then from these two figures that the turbulence in an otherwise unforced symmetrically unstable front is driven by the negative PV (a limited fuel source) and ensuing SI. The final spectral slope is closest to l^{-3}.

The $Ri = 2,\ \mu = 1$ case does not exhibit the same peak near the SI wavelength in F2 where the PV is negative near the surface. There is a peak near the SI wavelength in F1, however, no SI are expected there, nor was there strong evidence of SI in figure 5.9. There are two striking differences between the fronts in this case: 1) a peak near a wavelength of

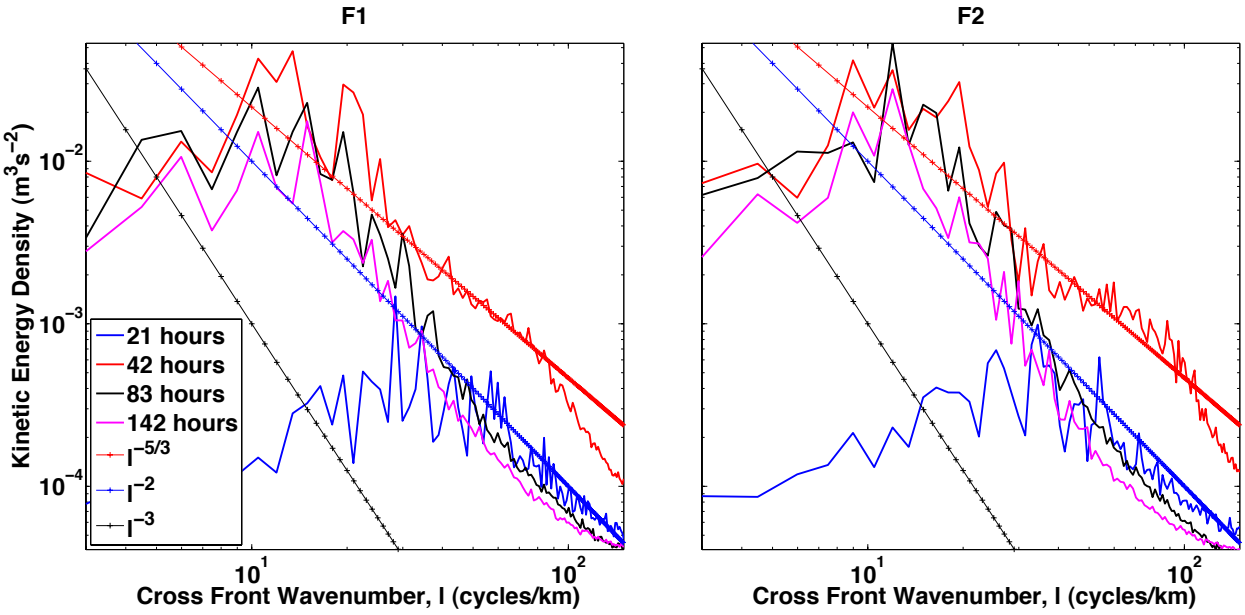

Figure 5.18: Kinetic energy spectra as a function of cross front wavenumber (l) for F1 (left), and F2 (right) for the $Ri = 0.5,\ \mu = 0$ case. Several different times during the run are shown. Spectral slopes of $l^{-5/3}$, l^{-2}, and l^{-3} are plotted for comparison.

125 m in F1 that lasts for several days but is absent from F2, and 2) the spectral slope of the final state of F1 appears to be closer to l^{-2} while the spectral slope of the final state of F2 is closer to l^{-3}. First, the peak near 125 m in F1 is consistent with the cross frontal scale of LC, which are present in F1, but not in F2. The fact that this peak persists, unlike the peak at the SI wavelength in the no stokes case demonstrates how the LC emanate from the Stokes drift which drives the flow. This is unlike the depletion of a finite reservoir of negative PV in the no Stokes case. The fact that F2 has a spectral slope closer to l^{-3} is consistent with similarities to the no Stokes case since SI is present. Lastly, the final state of F1 is considerably more energetic than F2, which is again consistent with the presence of LC in F1 which are absent from F2.

The $Ri = 0.5,\ \mu = 2$ case shows the same peak near the SI wave number early in the run in both F1 and F2. The peak in F2 is considerably stronger, which is consistent with the large reservoir of negative PV near the surface in F2. Unlike the $Ri = 2,\ \mu = 1$ case,

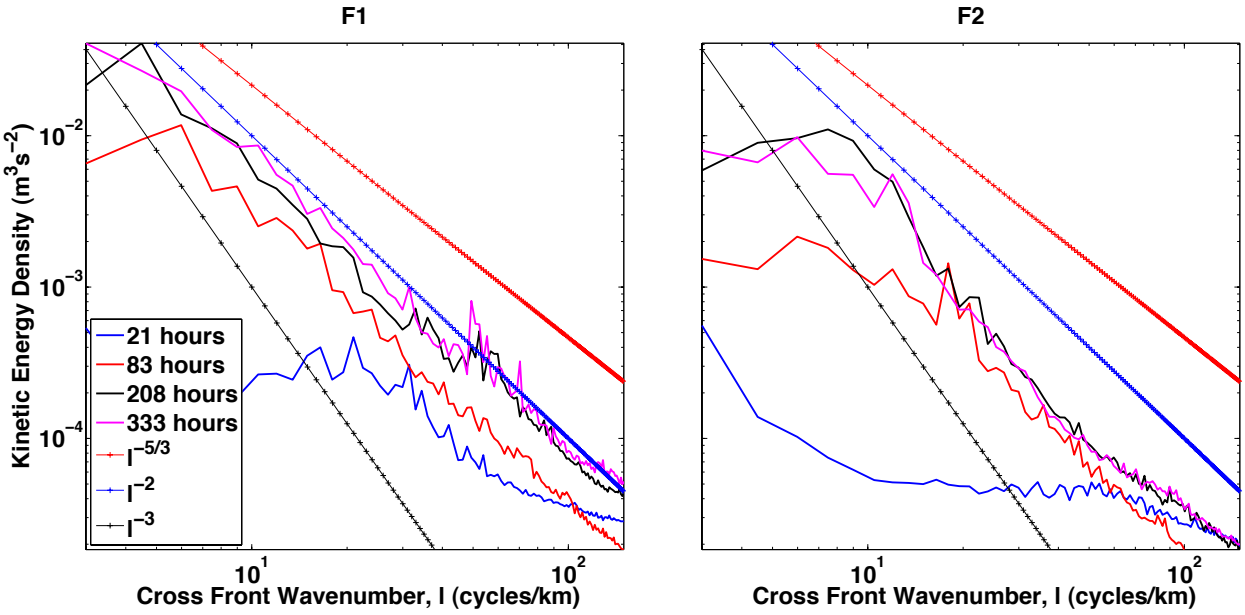

Figure 5.19: As in figure 5.18 but for $Ri = 2,\ \mu = 1$.

despite the presence of LC in both fronts, there appears to be no persistent peak near the LC wavelength. However it should be noted that this peak does not appear in the $Ri = 2,\ \mu = 1$ case until about eight days, while this case was only run for 6 days. Again, in the case with strong SI (F2) the spectral slope is closer to l^{-3} while it is closer to l^{-2} in F1. Lastly, F2 contains far more energy in its final state than F1. This suggests that SI, which is very strong in F2, produces far more kinetic energy in this configuration than LC, which is fairly strong in both fronts. This also further reinforces the idea that the anti-Stokes flow is a driver of SI analogous to down-front winds in the case of FSI.

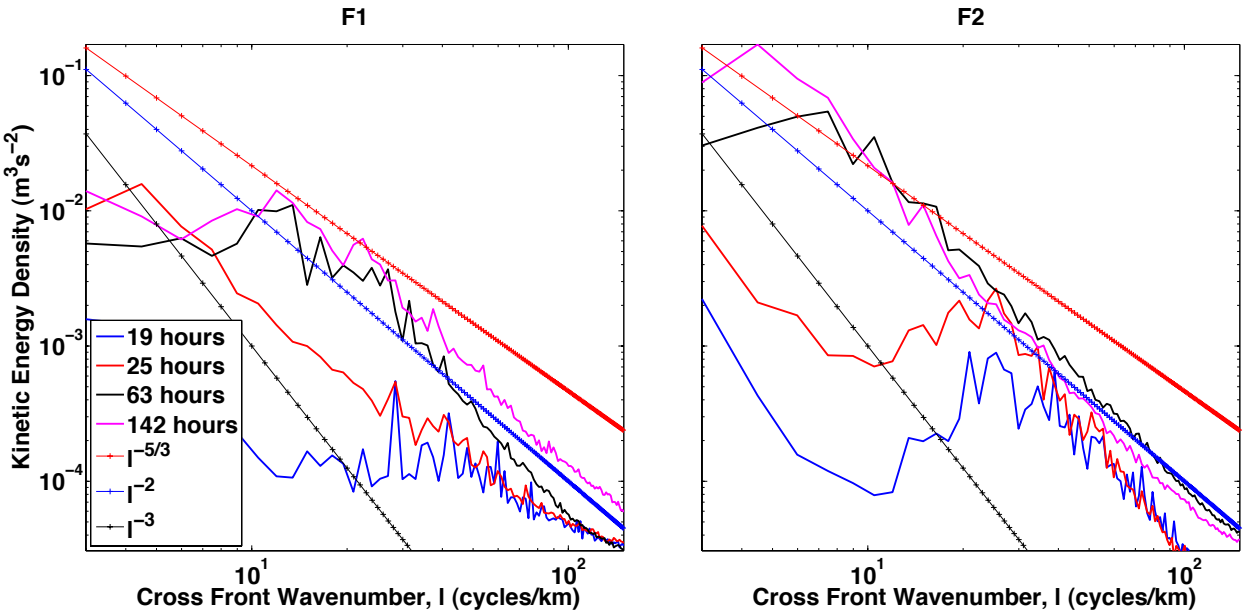

Figure 5.20: As in figure 5.18 but for $Ri = 0.5,\ \mu = 2$.

The kinetic energy spectra highlight several of the features that were apparent in both the velocity slices, and the energy production terms. SI show a significant peak in the energy spectra when they are strong, and if driven, the front becomes extremely energetic. Even in cases of consistent driving, however, the energy from SI is transferred to larger scales, and eventually forms a spectral slope near l^{-3}. LC induce a significant peak in the kinetic energy spectrum in longer simulations, which lasts for several days. This effectively creates a second cascade as seen in Hamlington et al. (2014) due to the strong surface forcing from Stokes drift.

5.5 Discussion

The LES showcase SI and LC quite well in multiple Stokes-front alignments. The linear stability does a reasonable job predicting the length scale for both SI and LC, however their growth rates appear to be somewhat slower than predicted. The negative PV criteria for the onset of SI holds in all cases. LC strongly affect the near surface shear by extracting Eulerian shear, however, it appears that any vertical mixing they might accomplish cannot compete with a stabilizing EBF.

SI are extremely strong when forced by negative PV in the Stokes layer, although the Stokes shear production itself indicates that the Stokes shear force does work against SI as predicted by the linear stability (table 5.1). Therefore, the Stokes drift may set up a mean flow with negative PV that favors SI, but the perturbation Stokes shear force suppresses SI. The near surface turbulence is dominated by LC when the Stokes drift is sufficiently strong, and the vertical stratification is sufficiently weak. The absence of SI very near the surface even in strongly negative PV regions may be due to an SI/LC interaction or to the suppression of SI by the Stokes shear force. There is no strong evidence that LC are suppressed by SI alone, although SI add to the restratification that occurs in stabilizing EBF cases.

The 1D, across front, kinetic energy spectra exhibited spectral slopes of l^{-3} in the fronts

with SI and l^{-2} in fronts without SI. LC induce a peak in the energy spectrum, highlighting that the presence of Stokes drift introduces an additional forcing scale to fronts. A front with strongly Stokes modified negative PV at the surface, moderately negative PV at depth, and weak LC, exhibited far more total kinetic energy than the neighboring front with positive PV near the surface, negative PV at depth, and strong LC. This highlights the role of Stokes drift as a strong driver of SI; a result that has been robust through analytic, linear, and nonlinear simulations.

Chapter 6

Conclusions

The ocean mixed layer is forced externally by winds, waves, and surface buoyancy fluxes, but these forcings do not dictate the structure of the mixed layer. Conservative mixed layer dynamics have been shown to be competitive with external diabatic processes in setting the thermal stratification and velocity structure. Furthermore, the interactions between dynamical mechanisms in the mixed layer are complicated and do not yield simple answers such as more waves produce more turbulence. The consideration of winds, waves, and mixed layer fronts allows for many possibly interesting, and complicating alignments between the three. However, I have developed a few simple scaling arguments, and instability criteria that shed light on both the dominant structures of the mixed layer, and their energy sources.

6.1 Summary

The unique scenario of a hurricane wake, provides a setting in which most of the parameters to estimate the effects of some dynamical restratification mechanisms are readily available through satellite SST data. This allows for simple scalings for wind and MLE driven restratification mechanisms to be derived and compared to surface heat fluxes. Past studies of wake restratification have restricted their attention to surface heat fluxes because they are the only non-conservative process that can restore any lost heat content from the ocean, however, enhanced mixing rather heat content loss is the primary reason for cold

wakes. Therefore, considering un-mixing (i.e. restratification) as possibly the primary driver in wake recovery is reasonable.

Timescales have been derived for the restratification of a wake by surface fluxes, EBF, and MLEs. In four hurricane wakes observed, the restratification time by surface fluxes was rivaled by EBF, with MLEs lagging far behind. In every case, the SST observations resulted in much shorter wake restoration times, however it is notable that this only implies that the thin surface layer was restored, whereas each of the derived timescales accounts for the restratification over the full climatological mixed layer depth. If it is assumed that a deeper (than the climatological depth) fraction of the wake restratifies, MLEs become more competitive and sometimes dominate. Typically some fraction of the wake close to the surface restratifies faster than the full wake. This seals off the sub-surface bolus which is then inaccessible by surface fluxes and EBF, and can therefore only be restratified by MLEs. The timescale for sub-surface bolus restratification is still quite long, and will exceed the time until the mixed layer deepens in winter. Lastly, although the observed wakes were likely unaffected by MLEs, the exercise in assuming a deeper wake restratification illustrates that the hurricane wake parameter regime is not far from one in which MLEs can compete with surface fluxes. This point is further strengthened by noting that the observed wakes were comparatively wide, and narrower fronts (which are present in the mixed layer) would imply far faster restratification by MLEs as compared with EBF since the the MLE restratification time scales with the square of the front width (equation 2.8).

The consideration of narrower and stronger fronts opens up the potential for a new class of instability that was not considered in the hurricane wake restratification: SI. Also notably absent from the wake restratification was the effect of waves. To address the effects of these mechanisms on the mixed layer a new linear stability model is developed. This model reproduces several linear stability results of previous works on LC, SI, and GI. Furthermore, it can smoothly transition between the extreme regimes in which each of these dynamical mechanisms was previously examined. In addition, this model allows for the possibility of

several mixed modes which are more representative of the real, nonlinear ocean mixed layer.

Some simple cases of the linear equations yield very useful analytic stability criteria. The classical, necessary criteria for QG baroclinic instability and SI have been re-derived with a mean flow in Lagrangian (Eulerian plus Stokes) thermal wind balance. The GI criteria, adapted from the Charney-Stern-Pedlosky criteria, on the QGPV and mean shear are unaltered, so long as the QGPV and mean shear are interpreted in their analogous Lagrangian forms. Numerical solutions with the linear stability model show that when GI does exist, the effect of Stokes drift is to make the growth rate and the wavenumber slightly larger when the Stokes drift is aligned with the geostrophic flow. When the Stokes drift is anti-aligned, the growth rate and wave number are reduced. This effect is likely that which has already been established by (Nakamura, 1988) in which increasing the shear reduces the penetration depth of the edge waves that cause baroclinic instability, therefore requiring a longer wavelength for them to interact and form GI. However, in this case, it is the anti-Stokes Eulerian shear that effects the edge wave penetration depth.

The SI criterion for instability, adapted from Hoskins (1974), is also unchanged. Negative Ertel PV is necessary for SI, however, in the presence of Stokes drift the PV is altered by the anti-Stoke Eulerian flow, and the direct relation between PV and Ri is broken. Therefore it is critical that the PV criteria is used if SI (with the full Eulerian shear in the PV) are of interest rather than any number of possible Eulerian, Lagrangian, Stokes, or geostrophic Richardson numbers. Numerical solutions with the linear stability model show that the negative PV criterion for SI holds even for Stokes drift that decays exponentially with depth. Furthermore, the motions of SI more closely follow surfaces of constant momentum when the Stokes modified PV is negative at the surface, and they more closely follow constant buoyancy surface at depth below the Stokes layer and where the geostrophic shear is constant. This is consistent with the parcel switching dynamics which show that SI utilize more energy than would be indicated by the PV alone. This also implies that the SI do more buoyancy production in the near surface region because they do more 'slantwise convection'

within momentum surfaces than they do centrifugal instability within buoyancy surfaces.

The new linear stability model allows a realistic parameter regime to be explored in which LC, SI, and GI all exist in modified forms. The growth rates and wavenumbers of each instability are comparable to their no Stokes counterparts. The Stokes drift in this case was aligned with the front, and therefore, SI are only present at depth. The strength of SI alternates with depth due to the rotating Ekman flow that alters the PV. SI are more driven by the potential energy (BP) than their no Stokes counterparts. The mixing by LC is greatly outweighed by the positive BP by GI and SI, however, the Reynolds stress profile ($\overline{w'b'}^{xy}(z)$) shows that SI and GI also do minimal mixing within the Stokes layer. Therefore, it is expected that LC are able to mix the near surface, but within a front, they will not be able to penetrate through to where SI and GI are strongly influential. Lastly, the Lagrangian shear production by LC is several orders of magnitude greater than the shear production by SI.

The linear stability analysis is complemented with fully nonlinear solutions of the WAB using LES. The anti-Stokes Eulerian flow develops into a Stokes-Ekman-Front layer which persists throughout each run (several days). For the fronts which have negative PV, this provides an very large PV source because the negative PV is maintained by the anti-Stokes Eulerian flow which is required to balance the mean Ekman flow. Since the source for the anti-Stokes flow is the waves, it is external to the system here since the flow has no feedback on the Stokes drift. The negative PV criterion for SI is again confirmed in a two simulations of four fronts, which provide all possible combinations of PV, Ri, and Ri^E criteria. The only portion of these fronts which exhibited SI were the ones with negative PV as expected.

The energetics of the simulated fronts showed that fronts with visibly apparent LC exhibited strong SSP and ESP in the Stokes layer, however SSP was negative deeper in the mixed layer when SI were present. This indicates that while the anti-Stokes Eulerian flow created negative PV conditions that favored SI, the perturbation Stokes shear force works against SI. The presence of SI is usually coincident with strong ESP. Energy spectra show

that in general fronts with SI or SI and LC have a spectral slope of l^{-3} while fronts with only LC have a spectral slope of l^{-2}. Furthermore, the fronts with the strongest LC exhibited a peak in the spectra (a break from an otherwise constant slope) that coincides with the length scale of LC. Lastly, in the front with the most strongly negative PV (and therefore SI), the total kinetic energy was at least an order of magnitude greater than other fronts which had strong LC but no SI.

All of the above results indicate a strong interaction particularly between Stokes drift and SI. The negative PV criteria based on the Stokes modified (through the anti-Stokes Eulerian flow) PV is a robust result that has been: 1) proven analytically in a special case, 2) confirmed in more realistic cases with numerical linear stability, and 3) confirmed in fully nonlinear LES. Furthermore, since this PV source comes from the waves, the shear that contributes to the PV will persist for very long times, with constant readjustment of the Ekman-Stokes-front flow that is the leading order balance. This persistent shear provides a large reservoir of energy for SI, thereby making negative PV fronts with Stokes drift far more energetic than positive PV fronts with Stokes drift.

The effects of Stokes drift on GI appear to be considerably less dramatic with small changes in growth rate and wavenumber. These affects were not assessed here in a fully nonlinear model, and the potential for exploring this interaction remains as future work. The effects of SI and GI on LC are also seemingly weak. The linear stability indicates that the increase in geostrophic shear provides the LC with more Eulerian shear, however in a realistic regime, this would be negligible. Previously stated results on the suppression of LC by strong vertical stratification are confirmed by the LES.

6.2 Testing These Conclusions in the Real Ocean

The Stokes modified negative PV criterion is such a robust phenomena that it deserves its own observational experiment. As discussed in the introduction, there have been considerable efforts to observe SI in the ocean, and success has been shown through the

dramatically increased TKE when EBF is strong. A particularly interesting observational experiment would be to look for cases of anti-Stokes forced SI. Recall that FSI may occur when down front winds reduce the PV. Also recall that the PV is reduced when the Stokes drift is directed up front. Therefore a region with opposed winds and waves is likely to have extremely strongly forced SI if there is a front present with the right alignment. Furthermore, the opposed winds and waves are likely to suppress LC, thereby isolating SI more than usual in such an experiment. Also, regions with opposed winds and waves are certain to be regions of swell rather than wind waves, and would therefore have deep Stokes layers to allow for a deeper region of forced SI.

The linear stability and LES results both suggest that the mixing done by LC is fairly small, and confined to a thin layer near the surface, and yet observations suggest that vertical mixing is substantially enhanced by LC. The LES shows that restratification by EBF is the strongest suppression mechanism on LC, but the linear stability results show that restratification by SI and GI is far stronger than mixing by LC. However, the linear stability results also showed that within the Stokes layer, SI and GI were suppressed at the surface (assuming the correct Stokes-front alignment). Therefore, a particularly interesting experiment would be to observe the differences in turbulent mixing in frontal zones with very deep and very shallow Stokes layers (i.e. with very long and very short wavelength waves, respectively). Ideally, of course the Stokes shears would be the same to control for the effective kinetic energy and PV fluxes by the waves, but among other things in this ideal experiment, this is hard to control. Would the restratifying instabilities of the frontal zone inhibit LC, or would the deep Stokes layer inhibit the formation of these instabilities as suggested by the linear stability results? In the shallow Stokes layer, would the mixing be so negligible as to only consider the frontal dynamics as setting the mixed layer depth? The results in this work suggest that LC plays a more minor role, and that Stokes drift plays a supporting role in enhancing the turbulence in frontal zones, and these suggestions warrant an attempt to confirm or refute them with observational experiments.

Bibliography

Bachman, S. and B. Fox-Kemper, 2013: Eddy parameterization challenge suite. I: eady spindown. *Ocean Modelling*, **64**, 12–28.

Boccaletti, G., R. Ferrari, and B. Fox-Kemper, 2007: Mixed layer instabilities and restratification. *Journal of Physical Oceanography*, **37 (9)**, 2228–2250.

Boyd, J. P., 2001: *Chebyshev and Fourier spectral methods*. Courier Dover Publications.

Charney, J. G., 1947: The dynamics of long waves in a baroclinic westerly current. *Journal of Meteorology*, **4 (5)**, 136–162.

Craik, A., 1977: The generation of langmuir circulations by an instability mechanism. *Journal of Fluid Mechanics*, **81 (02)**, 209–223.

Craik, A. and S. Leibovich, 1976: A rational model for langmuir circulations. *Journal of Fluid Mechanics*, **73 (03)**, 401–426.

D'Asaro, E. A. and G. T. Dairiki, 1997: Turbulence intensity measurements in a wind-driven mixed layer. *Journal of physical oceanography*, **27 (9)**, 2009–2022.

D'Asaro, E. A., T. B. Sanford, P. P. Niiler, and E. J. Terrill, 2007: Cold wake of hurricane frances. *Geophysical Research Letters*, **34 (15)**.

DAsaro, E., C. Lee, L. Rainville, R. Harcourt, and L. Thomas, 2011: Enhanced turbulence and energy dissipation at ocean fronts. *science*, **332 (6027)**, 318–322.

Eady, E., 1949: Long waves and cyclone waves. *Tellus*, **1 (3)**, 33–52.

Eliassen, A., 1983: The charney-stern theorem on barotropic-baroclinic instability. *pure and applied geophysics*, **121 (3)**, 563–572.

Emanuel, K., 2001: Contribution of tropical cyclones to meridional heat transport by the oceans. *Journal of Geophysical Research-Atmospheres*, **106 (D14)**, 14 771–14 781.

Ferrari, R., S. T. Merrifield, and J. R. Taylor, 2014: Shutdown of convection triggers increase of surface chlorophyll. *Journal of Marine Systems*.

Fox-Kemper, B. and R. Ferrari, 2008: Parameterization of mixed layer eddies. Part II: Prognosis and impact. *Journal of Physical Oceanography*, **38 (6)**, 1166–1179.

Fox-Kemper, B., R. Ferrari, and R. Hallberg, 2008: Parameterization of mixed layer eddies. Part I: Theory and diagnosis. *Journal of Physical Oceanography*, **38 (6)**, 1145–1165.

Fox-Kemper, B., et al., 2011: Parameterization of mixed layer eddies. iii: Implementation and impact in global ocean climate simulations. *Ocean Modelling*, **39 (1-2)**, 61–78.

Gnanadesikan, A. and R. A. Weller, 1995: Structure and instability of the ekman spiral in the presence of surface gravity waves. *Journal of Physical Oceanography*, **25 (12)**, 3148–3171.

Haine, T. W. and J. Marshall, 1998: Gravitational, symmetric, and baroclinic instability of the ocean mixed layer. *Journal of physical oceanography*, **28 (4)**, 634–658.

Hamlington, P. E., L. P. Van Roekel, B. Fox-Kemper, K. Julien, and G. P. Chini, 2014: Langmuir-submesoscale interactions: Descriptive analysis of multiscale frontal spin-down simulations. *Journal of Physical Oceanography*, **(2014)**.

Haney, S., et al., 2012: Hurricane wake restratification rates of one-, two-and three-dimensional processes. *Journal of Marine Research*, **70 (6)**, 824–850.

Harcourt, R. R. and E. A. D'Asaro, 2008: Large-eddy simulation of langmuir turbulence in pure wind seas. *Journal of Physical Oceanography*, **38 (7)**, 1542–1562.

Holm, D. D., 1996: The ideal craik-leibovich equations. *Physica D: Nonlinear Phenomena*, **98 (2)**, 415–441.

Hoskins, B., 1974: The role of potential vorticity in symmetric stability and instability. *Quarterly Journal of the Royal Meteorological Society*, **100 (425)**, 480–482.

Howard, L. N., 1961: Note on a paper of john w. miles. *J. Fluid Mech*, **10 (4)**, 509–512.

Huang, N. E., 1979: On surface drift currents in the ocean. *Journal of Fluid Mechanics*, **91 (01)**, 191–208.

Huang, P., T. B. Sanford, and J. Imberger, 2009: Heat and turbulent kinetic energy budgets for surface layer cooling induced by the passage of hurricane frances (2004). *Journal of Geophysical Research: Oceans (1978–2012)*, **114 (C12)**.

Kraus, E. and J. Turner, 1967: A one-dimensional model of the seasonal thermocline ii. the general theory and its consequences. *Tellus*, **19**, 98–106.

Lane, E. M., J. M. Restrepo, and J. C. McWilliams, 2007: Wave-current interaction: A comparison of radiation-stress and vortex-force representations. *Journal of physical oceanography*, **37 (5)**, 1122–1141.

Langmuir, I., 1938: Surface motion of water induced by wind. *Science*, **87 (2250)**, 119–123.

Large, W. and S. Pond, 1981: Open ocean momentum flux measurements in moderate to strong winds. *Journal of physical oceanography*, **11 (3)**, 324–336.

Large, W. and S. Yeager, 2012: On the observed trends and changes in global sea surface temperature and air-sea heat fluxes (1984-2006). *Journal of Climate*, **25 (18)**, 6123–6135.

Large, W. G., J. C. McWilliams, and S. C. Doney, 1994: Oceanic vertical mixing: A review and a model with a nonlocal boundary layer parameterization. *Reviews of Geophysics*, **32 (4)**, 363–403.

Leibovich, S., 1977a: Convective instability of stably stratified water in the ocean. *Journal of Fluid Mechanics*, **82 (03)**, 561–581.

Leibovich, S., 1977b: On the evolution of the system of wind drift currents and langmuir circulations in the ocean. part 1. theory and averaged current. *Journal of Fluid Mechanics*, **79 (04)**, 715–743.

Leibovich, S. and S. Paolucci, 1981: The instability of the ocean to langmuir circulations. *Journal of Fluid Mechanics*, **102**, 141–167.

Li, K., Z. Zhang, G. Chini, and G. Flierl, 2012: Langmuir circulation: An agent for vertical restratification? *Journal of Physical Oceanography*, **42 (11)**.

Mahadevan, A., E. DAsaro, C. Lee, and M. J. Perry, 2012: Eddy-driven stratification initiates north atlantic spring phytoplankton blooms. *Science*, **337 (6090)**, 54–58.

Malecha, Z., G. Chini, and K. Julien, 2014: A multiscale algorithm for simulating spatially-extended langmuir circulation dynamics. *Journal of Computational Physics*, **271**, 131–150.

McWilliams, J. C., 1985: A uniformly valid model spanning the regimes of geostrophic and isotropic, stratified turbulence: Balanced turbulence. *Journal of the atmospheric sciences*, **42 (16)**, 1773–1774.

McWilliams, J. C. and B. Fox-Kemper, 2013: Oceanic wave-balanced surface fronts and filaments. *Journal of Fluid Mechanics*, **730**, 464–490.

McWilliams, J. C., E. Huckle, J. Liang, and P. P. Sullivan, 2014: Langmuir turbulence in swell. *Journal of Physical Oceanography*, **44 (3)**, 870–890.

McWilliams, J. C., J. R. Restrepo, and E. M. Lane, 2004: An asymptotic theory for the interaction of waves and currents in shallow coastal water. **511**, 135–178.

McWilliams, J. C., P. P. Sullivan, and C.-H. Moeng, 1997: Langmuir turbulence in the ocean. *Journal of Fluid Mechanics*, **334**, 1–30.

Miles, J. W., 1961: On the stability of heterogeneous shear flows. *Journal of Fluid Mechanics*, **10 (04)**, 496–508.

Moeng, C.-H., 1984: A large-eddy-simulation model for the study of planetary boundary-layer turbulence. *Journal of the Atmospheric Sciences*, **41 (13)**, 2052–2062.

Monin, A. and A. Obukhov, 1954: Basic laws of turbulent mixing in the surface layer of the atmosphere. *Tr. Akad. Nauk SSSR Geophiz. Inst.*, **24 (151)**, 163–187.

Moum, J., D. Farmer, W. Smyth, L. Armi, and S. Vagle, 2003: Structure and generation of turbulence at interfaces strained by internal solitary waves propagating shoreward over the continental shelf. *Journal of Physical Oceanography*, **33 (10)**, 2093–2112.

Mrvaljevic, R., et al., 2013: Evolution of the cold wake of typhoon fanapi. *Geophys. Res. Lett.*, **40**.

Nakamura, N., 1988: Scale selection of baroclinic instability-effects of stratification and nongeostrophy. *Journal of the atmospheric sciences*, **45 (21)**, 3253–3268.

Pasquero, C. and K. Emanuel, 2008: Tropical cyclones and transient upper-ocean warming. *Journal of Climate*, **21 (1)**, 149–162.

Pedlosky, J., 1982: Geophysical fluid dynamics. *New York and Berlin, Springer-Verlag, 1982. 636 p.*, **1**.

Price, J. F., J. Morzel, and P. P. Niiler, 2008: Warming of SST in the cool wake of a moving hurricane. *Journal of Geophysical Research-Oceans*, **113 (C7)**.

Price, J. F., R. A. Weller, and R. Pinkel, 1986: Diurnal cycling: Observations and models of the upper ocean response to diurnal heating, cooling, and wind mixing. *Journal of Geophysical Research-Oceans*, **91 (C7)**, 8411–8427.

Smith, J. A., 1992: Observed growth of langmuir circulation. *Journal of Geophysical Research: Oceans (1978–2012)*, **97 (C4)**, 5651–5664.

Stone, P. H., 1966: On non-geostrophic baroclinic stability. *Journal of the Atmospheric Sciences*, **23 (4)**, 390–400.

Stone, P. H., 1970: On non-geostrophic baroclinic stability: Part ii. *J. Atmos. Sci*, **27 (5)**, 721–726.

Stone, P. H., 1971: Baroclinic stability under non-hydrostatic conditions. *J. Fluid Mech*, **45 (pt 4)**, 659–671.

Sullivan, P. P., J. C. McWilliams, and W. K. Melville, 2007: Surface gravity wave effects in the oceanic boundary layer: Large-eddy simulation with vortex force and stochastic breakers. *Journal of Fluid Mechanics*, **593**, 405–452.

Sullivan, P. P. and E. G. Patton, 2011: The effect of mesh resolution on convective boundary-layer statistics and structures generated by large-eddy simulation. *Journal of Atmospheric Sciences*, **68**, 2395–2415.

Suzuki, N. and B. Fox-Kemper, 2015: Understanding stokes forces in the wave averaged equations. *in preparation*.

Tandon, A. and C. Garrett, 1995: Geostrophic adjustment and restratification of a mixed layer with horizontal gradients above a stratified layer. *Journal of Physical Oceanography*, **25**, 2229–2241.

Taylor, J. R. and R. Ferrari, 2009: On the equilibration of a symmetrically unstable front via a secondary shear instability. *Journal of Fluid Mechanics*, **622**, 103–113.

Taylor, J. R. and R. Ferrari, 2010: Buoyancy and wind-driven convection at mixed layer density fronts. *Journal of Physical Oceanography*, **40 (6)**, 1222–1242.

Taylor, J. R. and R. Ferrari, 2011a: Ocean fronts trigger high latitude phytoplankton blooms. *Geophysical Research Letters*, **38 (23)**.

Taylor, J. R. and R. Ferrari, 2011b: Shutdown of turbulent convection as a new criterion for the onset of spring phytoplankton blooms. *Limnology and Oceanography*, **56 (6)**, 2293–2307.

Thomas, L. and J. Taylor, 2010: Reduction of the usable wind-work on the general circulation by forced symmetric instability. *Geophysical Research Letters*, **37 (18)**.

Thomas, L. N., 2005: Destruction of potential vorticity by winds. *Journal of physical oceanography*, **35 (12)**.

Thomas, L. N. and R. Ferrari, 2008: Friction, frontogenesis, and the stratification of the surface mixed layer. *Journal of Physical Oceanography*, **38 (11)**, 2501–2518.

Thomas, L. N. and P. B. Rhines, 2002: Nonlinear stratified spin-up. *Journal of Fluid Mechanics*, **473**, 211–244.

Thomas, L. N., J. R. Taylor, R. Ferrari, and T. M. Joyce, 2013: Symmetric instability in the gulf stream. *Deep Sea Research Part II: Topical Studies in Oceanography*, **91**, 96–110.

Vallis, G. K., 2006: *Atmospheric and oceanic fluid dynamics: fundamentals and large-scale circulation*. Cambridge University Press.

Van Roekel, L., B. Fox-Kemper, P. Sullivan, P. Hamlington, and S. Haney, 2012: The form and orientation of langmuir cells for misaligned winds and waves. *Journal of Geophysical Research: Oceans (1978–2012)*, **117 (C5)**.

Webb, A. and B. Fox-Kemper, 2011: Wave spectral moments and stokes drift estimation. *Ocean Modelling*, **40 (3)**, 273–288.

Weller, R. A. and J. F. Price, 1988: Langmuir circulation within the oceanic mixed layer. *Deep Sea Research Part A. Oceanographic Research Papers*, **35 (5)**, 711–747.

Zedler, S. E., P. P. Niiler, D. Stammer, E. Terrill, and J. Morzel, 2009: Ocean's response to hurricane frances and its implications for drag coefficient parameterization at high wind speeds. *Journal of Geophysical Research-Oceans*, **114**.

Appendix A

Hurricane wake restratification rates of one-, two- and three-dimensional processes

This paper has been published in the Journal of Marine Research (Haney et al., 2012). The full text may be found at:

http://dx.doi.org/10.1357/002224012806770937

Appendix B

Numerical Linear Stability Solver

```
%mcp_QG.m is most up to date version
%Begins from a reduced version of eqs 3.4-3.7 of Haney 2015
%dissertation. Uses M chebyshev modes to represent the 5 eq set.
%
%%%%%%%%%%%%%%%%Inputs
% M - nuber of Chebyshev modes
% Ri - Lagrangian Richardson number
% Ro - Lagrangian Rossby number
% alf - large scale aspect ratio H/L
% delta - scale separation parameter l/L, and u'~ delta*U
% mu - U^S/U^L, Stokes drift amplitude
% L - lambda = H/H^S, Stokes depth
% thet - Stokes direction wrt k-direction
% wind_dir - wind "               "
% tau_mag - D_z(U^E/U^L), normalized surface Eulerian shear
% Ek - Ekman number = nu/fL^2
% Pr - Prandtl number = nu/kappa
% gam - Dz(U^g/U^L), normalized geostrophic shear (front strength)
% klist - list of k's (along front wavenumber) to solve for
% llist - "     " l's (across front wavenumber) "      "
% kstart through lres - if you want to specify klist and llist as
% start, end, and resolution in k, l, you do it this way.
%
%%%%%%%%% Outputs
% sigr - real part of sigma
% sigi - imaginary part of sigma (the growth rate)
% eVV - array of size (klist,llist,5*M,5*M)
% EE - the full array of paired eigenvalues (sigr + i*sigi)
% A - Cheb space array of time independent coefficients in the equat
% B - "            " dependent "                          "
% Us - Cheb space Us operator
% Vs - "        " V stokes "
% UL - "         " U Lagrangian
% VL - "          " V "
%

%do_fn=0;
%if do_fn
function [sigr,sigi,eVV,klist,llist,EE,A,B,Us,Vs,UL,VL] = ...
    mcp_QG(M,Ri,Ro,alf,delta,mu,L,thet,wind_dir,tau_mag,Ek,Pr,...
    gam,klist,kstart,kend,kres,llist,lstart,lend,lres)
%geostrophic = 1;
if nargin < 5, klist = [0.01:0.01:1]; end;
if nargin < 9, llist = [0:1:5]; end;
if exist('klist')
  if isempty(klist)
    clear klist
  end
end

if exist('llist')
  if isempty(llist)
```

```
  end
end
%end
%close all
%clear all

nvsave = 5; %# of eigenvects to save
do_params=0;
do_normalize = 1; %normalize A,B s.t. eq is O(1). Could do mode by
                  %mode also

if do_params
  %%%%%%%%%%%%%%% Set Parameters %%%%%%%%%%%%%%%%%%%%%
  %%%%%%% This is usuall done for debugging only %%%%%%%%
  M = 50; % # of cheb modes
  Ri = 0.01;
  gam = 0;
  %Ro = 0.01; % Rossby #
  Ro = 10^11;
  %alf = .001; % aspect ratio
  alf = Ro^-1; % aspect ratio
  %alf = Ro; % aspect ratio
  %alf = Ro*.00053;
  %alf = Ro*0.15*(-1+(L/2))^2; % aspect ratio
  thet = 0; %stokes dir. 0 to 2*pi
  %thetl = [-pi/8:pi/8:pi/4];
  klist = [0];
  %klist = [[0:1:10] [15:5:20]];
  %klist = [[0:0.5:3] [4:10] [15:5:20]];
  kstart = 1; % x-wavenumber to start looping over
  kend = 2;
  kres = 1; %# of k's to loop over
  %llist = [[0:1:50] [55:5:100] [110:20:400]];
  %llist = [0:1:20];
  llist = [0:.1:7];
  %llist = [];
  lstart = 5; % y-wavenumber to start looping over
  lend = 6;
  lres = 2;
  %mul = [0 0.1 0.25 0.5 0.75 1 2 4 8];
  mu = 0.4;
  L = 2;
  %epsilon = mu*1*Ro; %only if L=1 in mcp
  %epsilon = mu*5*Ro; %only if L=5 in mcp
  %Ek = 0.01;
  %Ek = 0;
  %Ek = Ro*0.001*alf*(1-mu);
  %Ek = Ro*0.001*(1-mu)/alf;
  LaLP = 100^-1;
  Ek = (2*alf*Ro*LaLP*mu^0.5*(1-mu*L)^0.5)/L^(3/2);
  %Pr = 7;
  %Pr = 4000*0.001;
  Pr = 6.7;
```

```
%%%%%%%%%%%%%%% Set k and l lists %%%%%%%%%%%%%%%%%
if kres == 0
  klist = [kstart];
else
  if exist('klist')
  else
    klist = [kstart:(kend-kstart)/(kres-1):kend];
  end
end

if lres == 0
  llist = [lstart];
else
  if exist('llist')
  else
    llist = [lstart:(lend-lstart)/(lres-1):lend];
  end
end
%%%%%%%%%%%%%%% Define Grid %%%%%%%%%%%%%%%%%%%%%%
z_real = flipud([-1:2/(M-1):1]');
%z_real = linspace(0,1,M)';
z_cheb = cheb_grid(M);
Z_VALS = [-1 1]; %endpoint values for BC's

%%%%%%%%%%%%%%% Important Operators %%%%%%%%%%%%%%%
%%%%% Identity things %%%%
I_Z = sparse(eye(M));
I_var = sparse(eye(5)); %5 since there are 5 eqs
I_Z_bc = I_Z; I_Z_bc(end,:)=0; %ONLY LEFT MULT!!! i.e. I_Z_bc*A
I_Z_bc2 = I_Z_bc; I_Z_bc2(end-1,:)=0; %ONLY LEFT MULT!!! i.e. I_Z_bc
%%%%% Derivative things %%%%
DZ = sparse(deriv(M));
coord_trans = 2; %(this is d(zeta)/dz where zeta is the cheb
                 %vertical coord). This 2 corresponds to z =
                 %(1+zeta)/2 i.e. going from [0 1] to [-1 1]
DZ = DZ*coord_trans;

%%%%%%%%%%%%%%% Background Flow %%%%%%%%%%%%%%%%%%%%%
%This is in general, non-constant coeff
% Choose Bkd based on regime
Mr = max([1,Ro^-1]);
%delta = min([Ro,Ro^-1]); %this is different than the notes
%delta = Ro;
%delta = alf;
%delta = 0.01;
if Ro<0.1 && gam>0 && Ek == 0
  do_exp_stokes = 1;
  do_geostrophic = 1;
  do_LC = 0;
  do_ekman = 0;
  do_Li = 0;
elseif Ro>10 %% be more specific
```

```
  do_exp_stokes = 1;
  do_LC = 1;
  do_geostrophic = 0;
  do_ekman = 0;
  do_Li = 0;
elseif Ro<0.1 && gam>0 && Ek>0 && Pr<6
  do_exp_stokes = 0;
  do_geostrophic = 0;
  do_LC = 0;
  do_ekman = 0;
  do_Li = 1;
elseif Ro<0.1 && Ek>0 %&& gam == 0
  do_exp_stokes = 1;
  do_ekman = 1;
  do_LC = 0;
  do_geostrophic = 0;
  do_Li = 0;
end


%stokes part is independent of Bkd
if do_exp_stokes
  Us_real = exp(-0.5*L*(-z_cheb+1)); %mu = Us/U, L is stokes decay s
else
  Us_real = 0.5*(z_cheb+1); % linear Stokes
end
Us_cheb = phys2cheb(Us_real);
Us = cheb_prod(Us_cheb);
Vs = sin(thet)*Us;
Us = cos(thet)*Us; %note that above Us variable is magnitude
Vs_cheb = sin(thet)*Us_cheb;
Us_cheb = cos(thet)*Us_cheb;
Usz = DZ*Us_cheb; Usz = cheb_prod(Usz);
Vsz = DZ*Vs_cheb; Vsz = cheb_prod(Vsz);

if do_geostrophic
  %%%%%%%%%%%% Lagrangian Part (i.e. Ug+Us+Uanti-stokes = Ug)
  UL_real = 0.5*(z_cheb+1);  %bkd flow in real space
  U_cheb = phys2cheb(UL_real);%"         " cheb space
  UL = cheb_prod(U_cheb);%MxM matrix gives action of arg on cheb vec
  Uz = DZ*(U_cheb-mu*Us_cheb); Uz = cheb_prod(Uz);
  Vz = -mu*Vsz; % only due to geostrophy
  VL = 0;
  U_real = UL_real-mu*Us_real;

  %%%%%%%%%%%%%% Background Buoyancy %%%%%%%%%%%%%%%
  %This is in general, non-constant coeff
  By = -I_Z; % normalized dB/dy
  Bz = I_Z;  % dB/dz

elseif do_LC % For reproducing Leibovich and Paolucci 1981 JFM
  %%%%%%%%%%%% Eulerian Part (i.e. Ue+Us = UL, UL|_z=0 = 1 by def)
  U_real = 0.5*(1-mu*L)*(z_cheb+1)-mu+mu*L; %bkd flow in real space
```

```
  U = cheb_prod(U_cheb); % MxM matrix gives action of arg on cheb ve
  Uz = DZ*U_cheb; Uz = cheb_prod(Uz);
  % no V or Vz since not geostrophic
  Vz = zeros(M);
  UL = U+mu*Us;
  VL = zeros(M);

  %%%%%%%%%%%%%% Background Buoyancy %%%%%%%%%%%%%%%
  %This is in general, non-constant coeff
  By = -I_Z; %dB/dy
  Bz = I_Z; %dB/dz

elseif do_Li % For reproducing Li et al. 2012
  U_real = tau_mag*0.5*(z_cheb+1);
  U_cheb = phys2cheb(U_real);%"          " cheb space
  U = cheb_prod(U_cheb);%MxM matrix gives action of arg on cheb vect
  Uz = DZ*U_cheb; Uz = cheb_prod(Uz);
  Vz = zeros(M);
  UL = U+mu*Us;
  VL = zeros(M);
  By = -I_Z; %dB/dy
  Bz = I_Z; %dB/dz

elseif do_ekman
  eta = alf/sqrt(2*Ek); % = H/H_E
  zhat = 0.5*(z_cheb-1); % map [-1,1] -> [-1,0]
  %%%%% Ekman-Stokes-front solution (appendix of Haney 2015 Disserta
  Ek_amp = (1/((1+i)*eta))*(tau_mag*exp(i*wind_dir)-gam-(2*i*L* ...
        mu*exp(i*thet))/((L/eta)^2-2*i));
  phi = Ek_amp*exp((1+i)*eta*zhat)+gam*zhat+2*i*mu*exp(i*thet)*...
        exp(L*zhat)/((L/eta)^2-2*i);

  U_real = real(phi);
  V_real = imag(phi);
  U_cheb = phys2cheb(U_real);%"          " cheb space
  V_cheb = phys2cheb(V_real);%"          " cheb space
  U = cheb_prod(U_cheb);%MxM matrix gives action of arg on cheb vect
  Uz = DZ*U_cheb; Uz = cheb_prod(Uz);
  V = cheb_prod(V_cheb);%MxM matrix gives action of arg on cheb vect
  Vz = DZ*V_cheb; Vz = cheb_prod(Vz);
  UL = U+mu*Us;
  VL = V+mu*Vs;
  %%%%% Check |UL| %%%%%%%%%%%%%
  UL_real = cheb_operator_test(UL);
  VL_real = cheb_operator_test(VL);
  ULz_real = cheb_operator_test(DZ*UL);
  VLz_real = cheb_operator_test(DZ*VL);

  stopper = 0;
  if abs(sqrt(UL_real(1)^2+VL_real(1)^2)-1)>0.01
    disp('problem with |UL| not normalized correctly. |UL| - 1 =')
    sqrt(UL_real(1)^2+VL_real(1)^2)-1
    stopper = 1;
```

```
  if abs(sqrt(ULz_real(1)^2+VLz_real(1)^2)-1)>0.01
    disp('problem with |ULz| not normalized correctly. |ULz| - 1 =')
    sqrt(ULz_real(1)^2+VLz_real(1)^2)-1
    stopper = 1;
  end
  stopper = 0; % these are just warnings now
  if stopper ~=0
    stop
  end
  %%%%% Note that the normalization used here means that the
  %lagrangian (and Eulerian) shear direction is different from the
  %lagrangian flow direction. The Stokes and Stokes shear
  %directions are, however, the same. Think about whether this
  %matters. As best I can tell this is likely fine... but what
  %impact does this have on the lagrangian advection of things like
  %buoyancy.

  %%%%%%%%%%%%%% Background Buoyancy %%%%%%%%%%%%%%%
  %This is in general, non-constant coeff
  By = -I_Z; %dB/dy
  Bz = I_Z; %dB/dz
end
epsilon = mu*L*Ro;
Mrp = max(delta/Ro,1);

%%%%%%%%%%%% Build Matrix Problem %%%%%%%%%%%%%%%%%%
% It should look roughly like this:
%           A                      V                B        V
%[ikU -Ro     Uz       0    ikRi][u] =     [1 0 0     0 0][u]
%[Ro   ikU    0        0    ilRi][v] =     [0 1 0     0 0][v]
%[0    0      ikalf^2U -Ri  RiDZ][w] =-isig[0 0 alf^2 0 0][w]
%[0 By/(RoRi) Bz        ikU    0][b] =     [0 0 0     1 0][b]
%[ik   il     DZ        0      0][p] =     [0 0 0     0 0][p]

%%%%%%%%%%%%%%%%%% Loop over k's or l's, etc.%%%%%%%%%%%%
%%Initialize
EE = zeros([length(klist) length(llist) 5*M]);
sigr = EE;
sigi = EE;
for kk = 1:length(klist)
  for ll = 1:length(llist)
    k=klist(kk); l = llist(ll);
    %%%%%%% Put em together %%%%%%%%
    % 1,2,3,4,5 -> u,v,w,b,p or u,v,w,b,cont eqs
    %%%%%%% Build A Matrix %%%%%%%%%%
    % \tilde{u} eq
    A11 = Ro*(i*k*UL+i*l*VL)-(delta*Ek/alf^2)*DZ^2+(Ek/delta)*...
        (k^2+l^2)*I_Z;
    A12 = -delta*I_Z;
    A13 = Ro*Uz;
    A14 = zeros(M);
    A15 = Mrp*i*k*Ro*I_Z;
    % \tilde{v} eq
```

```
A22 = Ro*(i*k*UL+i*l*VL)-(delta*Ek/alf^2)*DZ^2+(Ek/delta)*...
    (k^2+l^2)*I_Z;
A23 = Ro*Vz;
A24 = zeros(M);
A25 = Mrp*i*l*Ro*I_Z;
% \tilde{w} eq
A31 = epsilon*delta*Usz/L/Ro^2;
A32 = epsilon*delta*Vsz/L/Ro^2;
A33 = (alf^2/delta/Ro)*(i*k*UL+i*l*VL)-(Ek/Ro^2)*DZ^2+...
(Ek*alf^2/delta^2/Ro^2)*(k^2+l^2)*I_Z;
A34 = -Mrp*(delta/Ro)*I_Z;
%A34 = zeros(M);
A35 = Mrp*(delta/Ro)*DZ;
% \tilde{b} eq
A41 = zeros(M);
A42 = (delta*gam/Ro/Mr)*By;
A43 = (Ri/Mr)*Bz;
A44 = Mrp/Mr*(i*k*UL+i*l*VL-(Ek*delta/Ro/Pr/alf^2)*DZ^2...
+(Ek/Ro/Pr/delta)*(k^2+l^2)*I_Z);
%A44 = I_Z;
A45 = zeros(M);
% cont eq
A51 = i*k*I_Z;
A52 = i*l*I_Z;
A53 = DZ;
A54 = zeros(M);
A55 = zeros(M);

%%%%%%% Build B Matrix %%%%%%%%%%
% \tilde{u} eq
sgn = 1;
B11 = sgn*Ro*i*I_Z;
B12 = sgn*zeros(M);
B13 = sgn*zeros(M);
B14 = sgn*zeros(M);
B15 = sgn*zeros(M);
% \tilde{v} eq
B21 = sgn*zeros(M);
B22 = sgn*Ro*i*I_Z;
B23 = sgn*zeros(M);
B24 = sgn*zeros(M);
B25 = sgn*zeros(M);
% \tilde{w} eq
B31 = sgn*zeros(M);
B32 = sgn*zeros(M);
B33 = sgn*(alf^2/delta/Ro)*i*I_Z;
B34 = sgn*zeros(M);
B35 = sgn*zeros(M);
% \tilde{b} eq
B41 = sgn*zeros(M);
B42 = sgn*zeros(M);
B43 = sgn*zeros(M);
B44 = sgn*Mrp/Mr*i*I_Z;
```

```
   %B44 = sgn*zeros(M);
   B45 = sgn*zeros(M);
   % cont eq
   B51 = sgn*zeros(M);
   B52 = sgn*zeros(M);
   B53 = sgn*zeros(M);
   B54 = sgn*zeros(M);
   B55 = sgn*zeros(M);

   if do_normalize
     % In principle this does not need to be done.
     for ii = 1:5
Amax =  max(max(abs([eval(['A' num2str(ii) '1']),...
           eval(['A' num2str(ii) '2']),...
     eval(['A' num2str(ii) '3']),...
           eval(['A' num2str(ii) '4']),...
     eval(['A' num2str(ii) '5'])])));
Bmax =  max(max(abs([eval(['B' num2str(ii) '1']),...
           eval(['B' num2str(ii) '2']),...
     eval(['B' num2str(ii) '3']),...
           eval(['B' num2str(ii) '4']),...
     eval(['B' num2str(ii) '5'])])));
ABmax = max([Amax Bmax]);
for jj = 1:5
  %Normalize A
  Aij = genvarname(['A' num2str(ii) num2str(jj)]);
  eval([Aij '= eval(Aij)./ABmax;']);

  %Normalize B with same norm const
  Bij = genvarname(['B' num2str(ii) num2str(jj)]);
  eval([Bij '= eval(Bij)./ABmax;']); %NEED Amax here!!!
end
     end
    end

   %%%%%%%%%% BC's %%%%%%%%%%%%%%%
   noflux = sparse(bc_1d(M,{'D_R','D_L'},[0 0],Z_VALS)); %var=0
   noflux_bottom = sparse(bc_1d(M,{'D_L'},0,Z_VALS)); %w=0 at botto
   noflux_top = sparse(bc_1d(M,{'D_R'},0,Z_VALS)); %w=0 at top
   nostress = coord_trans*sparse(bc_1d(M,{'N_L','N_R'},[0 0],Z_VALS
   nostress_top = coord_trans*sparse(bc_1d(M,{'N_R'},[0],Z_VALS));
   %D2 = (coord_trans^2)*sparse(bc_1d(M,{'D2_R'},[0],Z_VALS)); %D2
   D2 = (coord_trans^2)*sparse(bc_1d(M,{'D2_L'},[0],Z_VALS)); % D2
   %!!!!!!!!!!! If you change the bc value to something other than
   %0 you need to add that to the appropriate spot in the B matrix!

   %%%%%%% Which kind of BC for u,v,w,b,cont? %%%%%%%%%%
   if Ek>0 %do_LC || do_ekman
     UBC = I_Z_bc2;
     VBC = I_Z_bc2;
     WBC = I_Z_bc2;
     BBC = I_Z_bc2;
     CBC = I_Z_bc;
```

```
    VVBC = nostress;
    WWBC = noflux_top+[D2(2:end,:);zeros(1,M)];
    BBBC = nostress;
    CCBC = noflux_bottom; %on W in c-eq
  else   %if do_geostrophic
    UBC = I_Z;
    VBC = I_Z;
    WBC = I_Z_bc;
    BBC = I_Z;
    CBC = I_Z_bc;
    UUBC = zeros(M);
    VVBC = zeros(M);
    WWBC = noflux_top;
    BBBC = zeros(M);
    CCBC = noflux_bottom; %on W in c-eq
  end
  A = [[UBC*A11+UUBC,UBC*A12,UBC*A13,UBC*A14,UBC*A15];...
 [VBC*A21,VBC*A22+VVBC,VBC*A23,VBC*A24,VBC*A25];...
 [WBC*A31,WBC*A32,WBC*A33+WWBC,WBC*A34,WBC*A35];...
 [BBC*A41,BBC*A42,BBC*A43,BBC*A44+BBBC,BBC*A45];...
 [CBC*A51,CBC*A52,CBC*A53+CCBC,CBC*A54,CBC*A55]];

  B = [[UBC*B11,UBC*B12,UBC*B13,UBC*B14,UBC*B15];...
 [VBC*B21,VBC*B22,VBC*B23,VBC*B24,VBC*B25];...
 [WBC*B31,WBC*B32,WBC*B33,WBC*B34,WBC*B35];...
 [BBC*B41,BBC*B42,BBC*B43,BBC*B44,BBC*B45];...
 [CBC*B51,CBC*B52,CBC*B53,CBC*B54,CBC*B55]];
  %%%%%%%%%%%%%%%%%%%%%%%%%% Solver %%%%%%%%%%%%%%%%%%%%%%%%%%
  [eV,E] = eig(full(A),full(B));
  btol = 100; stol=1/btol;
  Eorig = E;
  uno=ones(1,length(E));
  E = uno*E; E(isinf(E))=nan; E = E(:);
  E(abs(E)>btol)=0;


  %%%% Sort Eigenvalues by real or im %%%%%%%%
  [sortsigr, Ir] = sort(real(E),'descend');
  [sortsigi, Ii] = sort(imag(E),'descend');
  EE(kk,ll,1:length(E))=E(Ii);
  %%%%%%% Save nvsave eigenvectors %%%%%%%%
  goodinds = nan; badinds = nan;
  ndx1 = 1; ndx2 = 1; ndx = 1;
  while ([length(goodinds)<=nvsave &&...
   ndx<=length(Ii) && ndx2<=length(Ii)])
    ugly = 0;
    mmodes = 10;
    no_wiggles = 1;
    do_eigenpair = 0;
    if no_wiggles
% ignore modes with lots of energy in high wavenumbers
for n = 1:5 %5 variables
  if max(abs(eV(M*n-mmodes:M*n,Ii(ndx))))>=...
```

```
    ugly = ugly+1;
  end
end
if do_eigenpair && ugly>0
  sortsigi(ndx) = -sortsigi(end-ndx+1);
  epair = squeeze(conj(EE(kk,ll,end-ndx+1)));
  eVpair = squeeze(-real(eV(:,Ii(end-ndx+1)))+...
     i*imag(eV(:,Ii(end-ndx+1))));
  tol = max(abs((A-squeeze(EE(kk,ll,end-ndx+1))*B)*...
  eV(:,Ii(end-ndx+1))));
  test = (A-epair*B)*eVpair;
  if max(abs(test))<=10*tol
    disp('it worked, kk, ll')
    kk
    ll
    sortsigi(ndx)
    ugly = 0;
  end
end
     end
     if ugly>0
badinds(ndx1) = ndx;
ndx1 = ndx1+1;
     else
goodinds(ndx2) = ndx;
ndx2 = ndx2+1;
     end
     clear ugly
     ndx = ndx+1;
   end
   if isnan(goodinds)
     sortsigi = zeros([length(sortsigi) 1]);
     eVV(kk,ll,:,1:nvsave)=zeros(squeeze(size(eV(:,1:nvsave))));
   else
     sortsigi = sortsigi(goodinds);
     sortsigr = sortsigr(goodinds);
     eVV(kk,ll,:,1:length(goodinds))=eV(:,Ii(goodinds));
     EE(kk,ll,1:length(goodinds))=EE(kk,ll,goodinds);
     EE(kk,ll,length(goodinds)+1:end) = zeros([length(EE(1,1,:))-..
         length(goodinds) 1]);
   end
   sigr(kk,ll,1:length(sortsigr)) = sortsigr;
   sigi(kk,ll,1:length(sortsigi)) = sortsigi;
 end
end
```

*Error: File: /Users/sean/research/CLPV/unstable_wave/mcp_QG_*
Unexpected MATLAB operator.

Published with MATLAB® 8.0

Appendix C

Derivation of the Ekman-Stokes-Front Layer

This section repeats the analytic calculation of the Stokes-Ekman layer in McWilliams et al. (2014), but in the notation of the present paper, with a single monochromatic wave, and with the addition of a balanced front. This derivation begins from equations 4.22-4.23, while noting that the flow is made steady despite the introduction of the front by an external buoyancy source.

$$\nabla_H \overline{P} + \hat{\mathbf{k}} \times \overline{\mathbf{U}}^L - Ek \nabla_H^2 \overline{\mathbf{U}} - \frac{Ek}{\alpha^2} \overline{\mathbf{U}}_{zz} = 0 \tag{C.1}$$

$$\overline{P}_z - \overline{B} = 0 \tag{C.2}$$

$$\textit{If} \quad \overline{B} = y + z, \quad \textit{then} \quad \nabla_H \overline{P} = \gamma z. \tag{C.3}$$

$$-\overline{V} - \frac{Ek}{\alpha^2} \overline{U}_{zz} = -\mu \sin(\theta) e^{\lambda z} \tag{C.4}$$

$$\overline{U} - \frac{Ek}{\alpha^2} \overline{V}_{zz} = -\gamma z + \mu \cos(\theta) e^{\lambda z} \tag{C.5}$$

summing the two,

$$-\overline{U} - i\overline{V} - \frac{Ek}{\alpha^2} \overline{V}_{zz} + i \frac{Ek}{\alpha^2} \overline{U}_{zz} = -\gamma z + \mu \cos(\theta) e^{\lambda z} + \mu \sin(\theta) e^{\lambda z} \tag{C.6}$$

$$\left[-i \frac{Ek}{\alpha^2} - 1 \right] \phi = -\gamma z + \mu e^{i\theta} e^{\lambda z} \tag{C.7}$$

$$\left[\partial_z^2 - i \frac{\alpha^2}{Ek} \right] \phi = -i \frac{\alpha^2}{Ek} \gamma z + i \frac{\alpha^2}{Ek} \mu e^{i\theta} e^{\lambda z} \tag{C.8}$$

$$\left[\partial_z^2 - 2i\eta^2 \right] \phi = -2i\eta^2 \gamma z + 2i\eta^2 \mu e^{i\theta} e^{\lambda z} \tag{C.9}$$

Since the Stokes drift and front strength are prescribed (by μ, λ, θ, and γ), this only changes the solution by adding a particular part. Therefore, the classic Ekman layer solution is given by the homogeneous part of equation C.9.

$$\phi^h = C_1 e^{(1+i)\eta z} + C_2 e^{-(1+i)\eta z} \tag{C.10}$$

Then the particular part is given by the right hand side

$$\begin{aligned} \phi^p &= C_3 z + C_4 e^{\lambda z} && \text{(C.11)} \\ \phi^p_{zz} &= C_4 \lambda^2 e^{\lambda z} && \text{(C.12)} \\ \implies C_3 &= \gamma && \text{(C.13)} \\ C_4 &= \frac{2i\mu e^{i\theta}}{(\frac{\lambda}{\eta})^2 - 2i} && \text{(C.14)} \end{aligned}$$

C_1 and C_2 are then given by the surface and bottom boundary conditions respectively.

$$\phi \to \gamma z, \ \ as \ z \to -\infty \tag{C.15}$$

$$\implies C_2 = 0 \tag{C.16}$$

$$\phi_z|_0 = \overline{U}_z|_0 + i\overline{V}_z|_0 = C_1(1+i)\eta + \gamma + \frac{2i\lambda\mu e^{i\theta}}{(\frac{\lambda}{\eta})^2 - 2i} \tag{C.17}$$

$$\implies C_1 = \frac{1}{(1+i)\eta}\left[\overline{U}_z|_0 + i\overline{V}_z|_0 - \gamma - \frac{2i\lambda\mu e^{i\theta}}{(\frac{\lambda}{\eta})^2 - 2i}\right] \tag{C.18}$$

Therefore, the full, analytic, Ekman-Stokes-Front layer (equation 4.26) is given by

$$\phi = \frac{1}{(1+i)\eta}\left[\hat{\tau}e^{i\theta^e} - \gamma - \frac{2i\lambda\mu e^{i\theta}}{(\frac{\lambda}{\eta})^2 - 2i}\right] e^{(1+i)\eta z} + \gamma z + \frac{2i\mu e^{i\theta}}{(\frac{\lambda}{\eta})^2 - 2i} e^{\lambda z}. \tag{C.19}$$